UNIVERSIDAD NACIONAL AUTÓNOMA DE MÉXICO
PROGRAMA DE DOCTORADO EN CIENCIAS (ASTROFÍSICA)

ENTENDIENDO EL FENÓMENO ‘BORN-AGAIN’ EN NEBULOSAS PLANETARIAS

TESIS
QUE PARA OPTAR POR EL GRADO DE:
DOCTOR EN CIENCIAS (ASTROFÍSICA)

PRESENTA:
JANIS BERENICE RODRIGUEZ GONZALEZ

TUTOR PRINCIPAL
JESUS ALBERTO TOALÁ SANZ, INSTITUTO DE RADIOASTRONOMÍA Y ASTROFÍSICA

MORELIA, MICHOACÁN. ENERO 2025

Resumen

Las nebulosas planetarias (NPs) representan una de las etapas finales en la evolución de estrellas de baja y mediana masa (1 $M_\odot \lesssim M_{\rm ZAMS} \lesssim 8$ $M_\odot$). Estas estrellas pueden perder más de la mitad de su masa inicial a través de vientos lentos y densos durante su fase en la rama asintótica de las gigantes (AGB, por sus siglas en inglés). Finalmente, cuando evolucionan hacia la etapa post-AGB, desarrollan un viento rápido (~1000 km s^{-1}) que barre y comprime el material previamente eyectado. Al mismo tiempo, el nuevo flujo de radiación ultravioleta (UV) fotoioniza el material, creando una NP.

En casos muy especiales, cuando la estrella desciende por la traza de enfriamiento de las enanas blancas, puede experimentar lo que se conoce como un "pulso térmico muy tardío" (VLTP, por sus siglas en inglés). Este fenómeno ocurre cuando la capa de He alcanza una masa crítica que provoca un evento termonuclear explosivo. Como resultado, la opacidad de la estrella aumenta, llevándola temporalmente a una segunda fase AGB. En esta etapa, el material procesado, pobre en H y rico en C, es eyectado hacia la NP preexistente, mientras la estrella central comienza a evolucionar nuevamente hacia una fase post-AGB. En cierto sentido, la estrella "renace", un fenómeno conocido como "born-again" (BA, por sus siglas en inglés). Hasta la fecha, se han identificado menos de 10 NPs *born-again*, la mayoría detectadas debido a la fuerte presencia de gas y polvo rico en C en sus interiores. Los estudios espectroscópicos de estas nebulosas reportan abundancias que no coinciden completamente con las predichas por los modelos de evolución estelar para estrellas simples (no binarias).

El objetivo de este trabajo es comprender el fenómeno *born-again* en NPs, abordándolo desde perspectivas tanto observacionales como teóricas, lo que nos ha permitido tener una visión más completa de este proceso. Mediante un análisis detallado del polvo en estas nebulosas y modelos de fotoionización, podemos demostrar que el material interno es producto del VLTP, considerando que una gran parte del C eyectado queda atrapado en el polvo. Utilizando observaciones de alta dispersión en combinación con modelos morfo-cinemáticos de dos de las nebulosas *born-again* más estudiadas hasta el momento, proponemos un escenario de formación que explica su morfología, cinemática y composición química. En este escenario, el material eyectado en las regiones más internas de la nebulosa corresponde a una eyección causada por el VLTP, la cual interactúa con una estrella compañera a través de un proceso de envolvente común.

Finalmente, exploramos la evolución estelar de estrellas que producen pulsos térmicos tardíos utilizando el código de evolución estelar MESA. Creamos una amplia red de modelos que nos permite estudiar las propiedades de las estrellas que experimentan un último pulso térmico en sus fases más avanzadas. Esto nos ha permitido

entender en detalle cómo diversos parámetros influyen en su evolución, siendo los vientos estelares los más relevantes para las estrellas deficientes en H.

Summary

Planetary nebulae (PNe) represent one of the final stages in the circumstellar evolution of low- and intermediate-mass stars (1 $M_{\odot} \lesssim M_{\rm ZAMS} \lesssim 8$ $M_{\odot}$). These stars can lose more than half of their initial mass through slow, dense winds during their asymptotic giant branch (AGB) phase. Eventually, as they evolve into post-AGB stars, they develop a fast wind ($\sim$1000 km s^{-1}) that sweeps up and compresses the previously ejected material. At the same time, the newly emitted ultraviolet (UV) radiation photoionizes the material, creating a PN.

In very special cases, when the star is descending along the white dwarf cooling track, it can experience what is known as a very late thermal pulse (VLTP). This occurs when the He shell reaches a critical mass, triggering an explosive thermonuclear event. As a result, the opacity of the star increases, briefly pushing it back into a second, short-lived AGB phase. During this stage, H-poor and C-rich processed material is ejected into the old PN, while the central star evolves one again toward a post-AGB phase. In a sense, the star is *born again*. To date, fewer than 10 born-again PNe have been identified, most of which were detected due to the strong presence of C-rich dust in their interiors. Spectroscopic studies of these nebulae report abundances that do not fully agree with the predictions from single stellar evolution models.

The goal of this work is to understand the born-again phenomenon in PNe, approaching it from both observational and theoretical perspectives. This has allowed us to gain a deeper view of the process. Through detailed analysis of the dust in these nebulae and photoionization models, we demonstrate that the inner material is a product of the VLTP, with a significant portion of the ejected C becoming trapped in the dust. Using high-dispersion spectroscopic observations and morpho-kinematic models of two of the most studied born-again nebulae to date, we propose a formation scenario that explains their morphology, kinematics, and chemical composition. In this scenario, the material ejected in the innermost regions of the nebula corresponds to a VLTP-driven ejection that interacts with a companion star through a common envelope process.

Finally, by using the MESA stellar evolution code, we created an extensive grid of models that allowed us to study the properties of stars that experience late thermal pulses in their most evolved phases. This has enabled us to peer into the details of how various parameters influence stellar evolution during this specific case of path, with stellar winds playing a crucial role for H-deficient stars.

Contents

Chapter 1

Introduction

1.1 Evolution of Solar-like stars

Low- and intermediate-mass stars ($0.8\ \mathrm{M}_\odot \lesssim M_{\mathrm{ZAMS}} \lesssim 8\ \mathrm{M}_\odot$) spend most of their lives in the main sequence (MS) phase. This phase begins when the force of gravity and pressure are balanced through hydrostatic equilibrium. During this phase, the core of the star is fusing H into He through the p-p chain or the CNO cyclo depending on the mass of the star. The main interest of this work is in the evolution beyond post-AGB, therefore we will not go into detail about MS phase.

As the star depletes the H in its core, the core contracts under the influence of gravity, causing the temperature to rise. This contraction triggers H fusion in a shell surrounding the inert helium core. With continued shell burning, the core contracts further until the temperature and pressure are high enough to ignite helium fusion, marking the onset of the horizontal branch (HB). The fusion of He occurs through the triple-α chain, a process that combines three He nuclei to form C.

The evolution that follows the He burning of the core is highly dependent on the initial stellar mass. When the central supply of He is depleted, He will continue to burn in one shell, while the H shell is almost dormant at this point. On the Hertzsprung-Russell (HR) diagram, the star will move toward a lower effective temperature (T_{eff}) and higher luminosity (L). This phase is quite similar to the previous red giant phase of low-mass stars, although the temperatures are slightly higher. For this reason it is known as the asymptotic giant branch (AGB). As the He shell catches up with the dormant H shell (see Fig. 1.1), the AGB star progresses into the thermal pulsation phase. During its dynamic stage, the star experiences a cyclical alternation in energy output between the H and He shells. At times, H shell burning dominates, producing most of the energy, while the He shell shell continuing at a lower rate. This alternation is followed by phases where helium shell burning intensifies and drives more energy output, temporarily reducing the contribution from the H shell. This intricate interplay between the two shells during thermal pulsations delineates a pivotal segment of a star's evolution during the AGB phase.

Each pulses last some hundred of years (Iben, 1981) but are capable of inducing a strong instability in the internal structure of the star. As a consequence of this

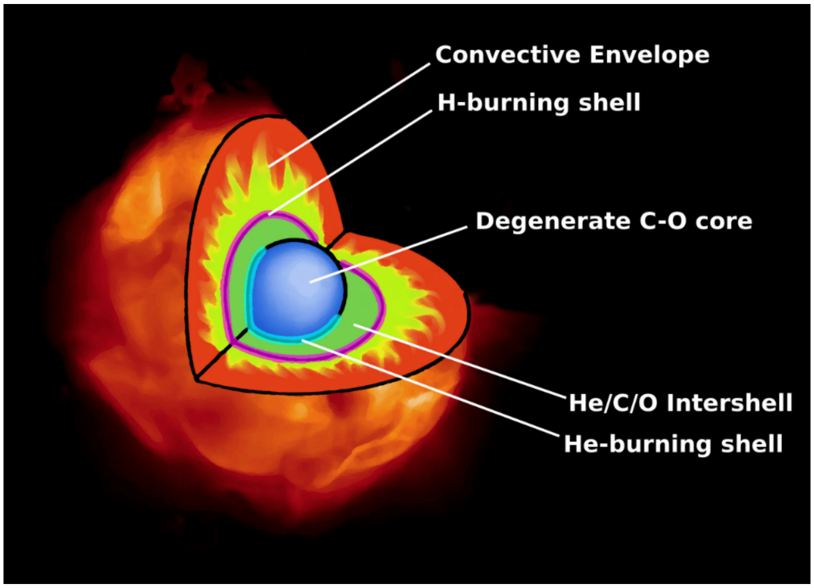

Figure 1.1: Diagram illustrating the internal structure of an asymptotic giant branch (AGB) star. The key features are the H-burning shell and He-burning shell, essential for the star's energy production. Taken from Miller Bertolami (2024)

instability, dredge-up occurs in which reprocessed nuclear material is transported to the surface of the star. A star can lose much of its mass during the AGB phase with a mass loss rate of $\lesssim 10^{-5}$ M$_\odot$ yr^{-1} (see Ramstedt et al., 2020, and references therein) producing a dense envelope. As a consequence, the opacity increases and AGB stars produce large amounts of dust in their atmospheres, which then contribute to the enrichment of the interstellar medium (Habing & Olofsson, 2003).

As the atmosphere is expelled away from the star into the circumstellar medium (CSM), deeper and hotter shells of the core are exposed, eventually leaving a nucleus mainly composed of H, He, C, and O. The subsequent evolution of this post-AGB star will produce a white dwarf (WD). When the exposed core reaches a temperature greater than $\sim 3\times10^4$ K, enough UV photons are emitted to ionize the ejected layers.

1.2 Formation of a planetary nebula

The simplest formation scenario is the so-called Interacting Stellar Winds Model (ISWM; see Kwok et al., 1978) and establishes that during the AGB phase the star can lose up to half its mass through a slow wind ($v_{\rm AGB}$ =10–30 km s^{-1}; produced by radiation pressure on dust grains) with high mass-loss rate ($\dot{M} \lesssim 10^{-5}$ M$_\odot$ yr^{-1}; Vassiliadis & Wood, 1993; Villaver et al., 2002). The effective temperature of the star is significantly reduced and dust and molecules are formed in the CSM (Cox et al., 2012).

As the star sheds its H-rich outer layers, the post-AGB star begins to warm up. Consequently, the peak of its emissivity shifts towards the UV, generating a photon

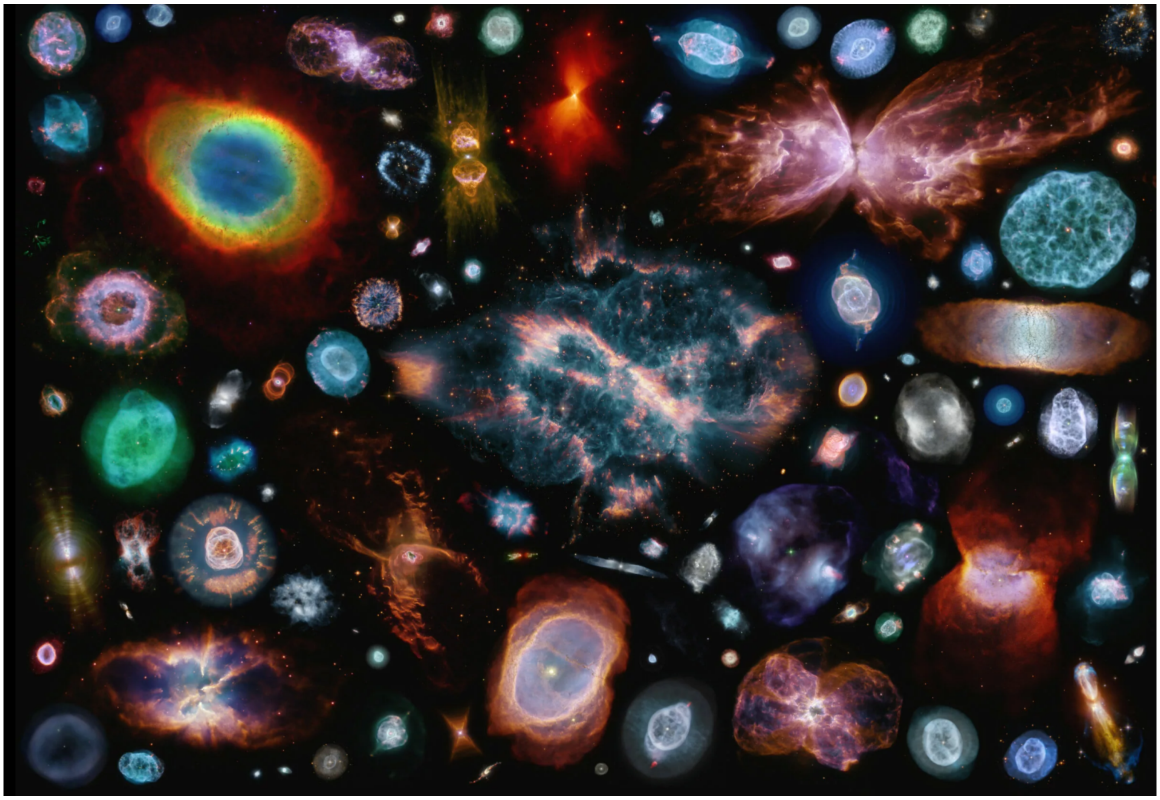

Figure 1.2: A *Hubble Space Telescope* sampler of post-AGB stars and PNe. Credits NASA/ESA/Judy Schmidt.

flow that radiatively accelerates material in the star's atmosphere through spectral lines. This phenomenon, known as line driven winds (see Chapter 8 of Lamers & Cassinelli, 1999), that can reach velocities as high as v_∞ =500–4000 km s^{-1} (Guerrero & De Marco, 2013) and smaller mass-loss rates ($\dot{M}$ $\lesssim$$10^{-10}$–$10^{-7}$ M$_\odot$ yr^{-1}). The fast post-AGB wind sweeps and compresses the material ejected previously in the AGB phase. Simultaneously, as $T_{\rm eff}$ continues to increase, it emits a strong flux of ionizing photons, capable of photoionizing elements in the surrounding material. This combination of physical process produces a PNe.

The ISWM is capable to explain the round or spherical morphologies observed in some PNe. However, most of PNe exhibit more capricious morphologies (see Fig. 1.2 and Sahai et al., 2011) that require more complex mechanism to explain its formation. As a step forward, Balick et al. (1987) proposed the Generalized Interacting Stellar Winds Model (GISW). These authors proposed that during the AGB phase the star has non-isotropic mass-loss episodes, with a dependence with the azimuth angle. This implies that near the equator the wind has a lower velocity and a larger density and the opposite can be said for the polar directions. When the stars evolved to the post-AGB phase and its presents a fast wind it could break the PN by the poles (see Fig. 1.3). This could explain PNe with bipolar morphology.

For years, the physical processes that can produce these morphologies in PNe

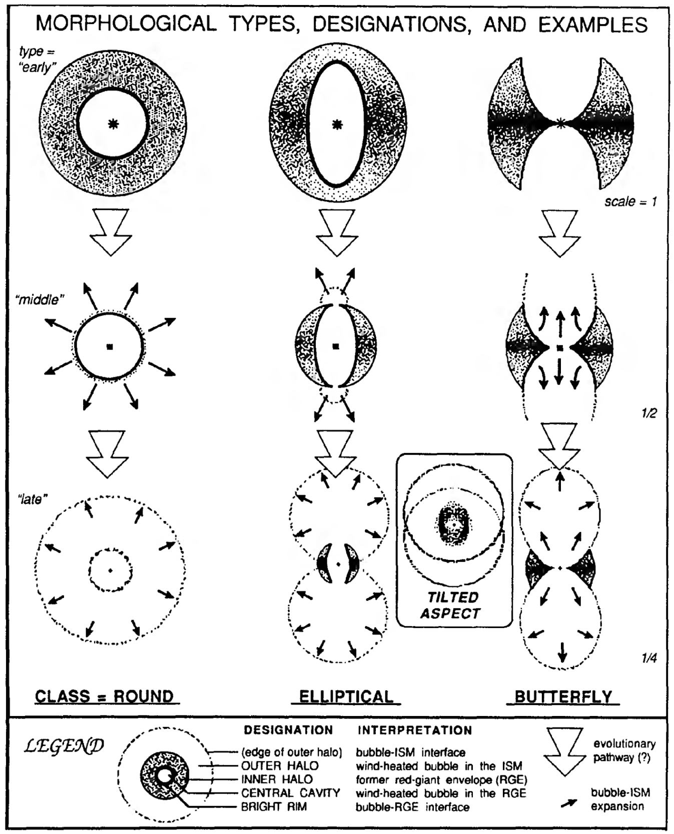

Figure 1.3: PNe formation scheme with different morphologies proposed by Balick et al. (1987). The scheme shows in a simple way how a round, spherical, and bipolar PN is formed and evolves.

have been sought and various mechanisms have been proposed, such is the presence of strong magnetic fields and bipolar ejections of material due to stellar rotation of the progenitor star. García-Segura et al. (1999) presented numerical simulations of the evolution and formation of PNe following the interaction scenario of two consecutive stellar winds. Their models have several parameters that vary but they highlight in this work that the formation of a nebula with very marked bipolar morphology can be obtained when the stellar rotation ($v_{\rm rot}$) approaches the critical rotation speed ($v_{\rm crit}$) in the AGB phase. Later work by García-Segura et al. (2016) refined this model, emphasizing that stellar rotation alone is insufficient to produce the complex bipolar structures observed in planetary nebulae. García-Segura et al. (2016) demonstrated that binary interactions, particularly tidal forces from a companion star, play a crucial role in spinning up the AGB star. This tidal spin-up enhances the star's rotation, but the formation of bipolar morphologies requires a combination of effects, including magnetic fields and winds. Thus, while rotation is an essential component, it must be complemented by binarity and magneto-hydrodynamic effects to fully account for the formation of bipolar PNe.

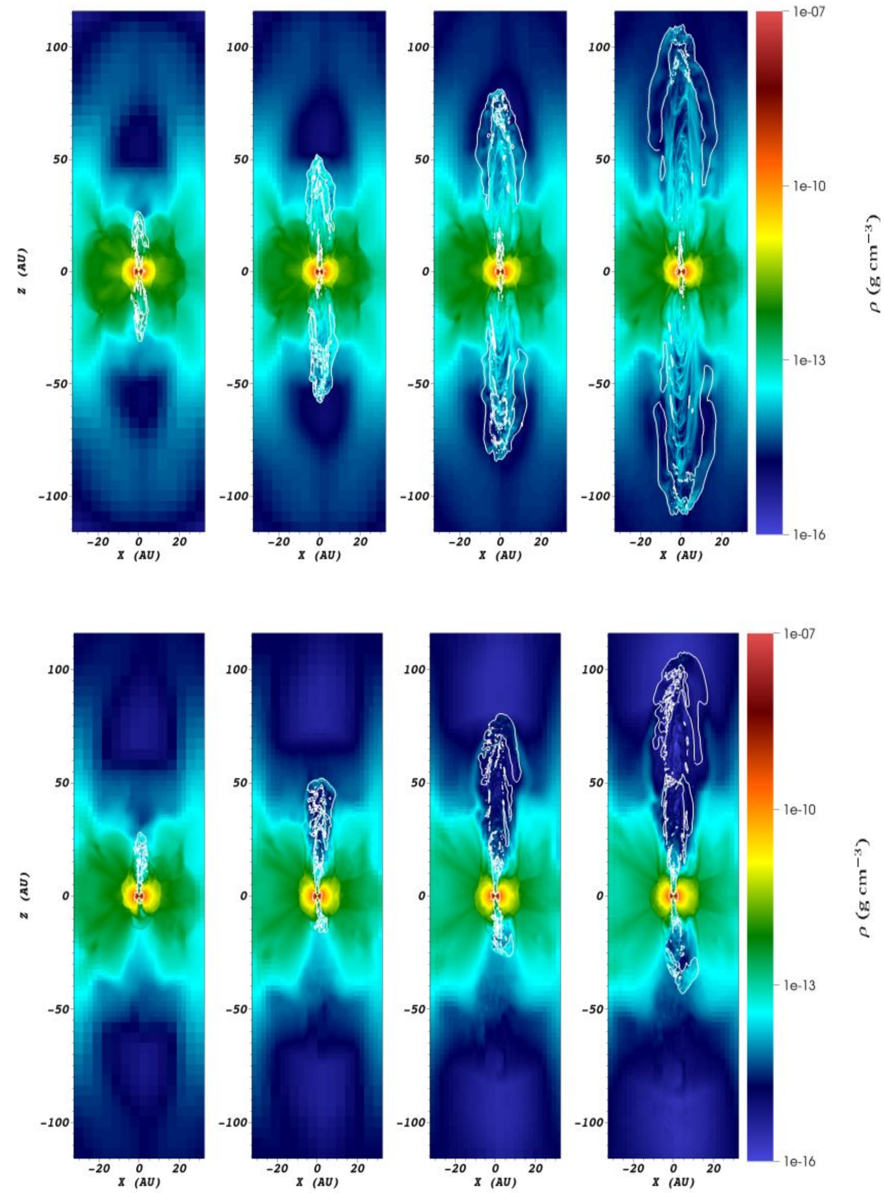

Figure 1.4: Numerical simulations taken from Zou et al. (2020), at the top we have their high momentum outflow density evolution model with radiative cooling. The panels, from left to right, are taken at 3460, 3840, 4200, 4600 days (460, 840, 1200, 1600 days after the fast wind turned on). At the bottom we have the evolution of the low momentum outflow density with radiative cooling. The panels, from left to right, are taken at 4760, 5580, 6400, 7000 days. The white outlines mark a constant temperature of 10,000 K.

Another parameter that they take into consideration in their models is the magnetic field. García-Segura et al. (2020) find that the combination of these two parameters reproduces a nebula with a morphology of a very strongly collimated bipolar. In the case of having a strong enough field, jets can be reproduced in the polar regions of the nebula. While weak fields lead us to the case of an elliptical nebula.

In addition, the role of a stellar companion has also been studied through simulation, particularly, the common envelope (CE) phase (Passy et al., 2012; Ricker & Taam, 2012; Ivanova et al., 2013, and referes therein). In their 3D numerical simulations, Zou et al. (2020) explored the CE ejection in a binary system, revealing its role in the formation of PN. The CE ejection process naturally establishes a high-density contrast environment from the pole to the equator, offering a plausible mechanism for the generation of bipolar PNe. This study underscores the significance of density contrast resulting from the loss of a common envelope as a foundational element for a diverse array of nebular models. The outcomes of their models showcase scenarios where symmetry is disrupted in the bipolar outputs, driven by GISW models (see for example Fig. 1.4). This occurs because the morphology of the bipolar lobes is determined by the asymmetries of the central part (funnel) of the CE ejection.

1.3 Born-again planetary nebulae

In previous sections it was explained that during the evolution of a low- or intermediate-mass star, the mass loss process forms PNe. Despite their diverse morphologies, PNe typically exhibit similar elemental abundances, with H predominating in the ejected envelope (Kaler, 1983; Stanghellini et al., 2000). However, over some decades it has been observed a peculiar phenomenon wherein certain PNe contain H-deficient material within them, while their central stars (CSPNe) exhibit either marginal H abundance or its absence entirely from their surfaces (De Marco et al., 1997; Górny & Tylenda, 2000; Werner & Herwig, 2006).

Notably, since the 1980s, two PNe showcasing these distinctive characteristics have been identified: PNe A66 30 and 78, colloquially referred to as A 30 and A 78 (see Hazard et al., 1980). The CSPN of A30 and A78 have been classified as H-poor stars, denoted as [WR]-PG 1159 stars (Weidmann et al., 2020).

The concept of born-again was initially proposed by Iben (1984) and has been further explored since then (see Iben & MacDonald , 1995; Schönberner, 1979; Herwig, 2001; Lawlor & MacDonald, 2003; Toalá et al., 2021, and references therein). Iben et al. (1983) presented stellar evolution models with interesting behavior in which after the star has passed the "knee" beyond the post-AGB phase on the HR diagram, it undergoes a remarkable event known as a very late thermal pulse (VLTP). During this phase, the star reignites its He shell (Lawlor & MacDonald, 2006; Miller Bertolami et al., 2006). As a result, the star will increase in size, causing its $T_{\rm eff}$ to decrease, which makes the star return to the region reserved for AGB stars on the HR diagram. As a result of the sudden He ignition, the processed material (H-poor and C-rich) expands within the old PN (see Fig. 1.5). From there, the star would repeat its evolution towards the post-AGB track for a second time as illustrated in Fig. 1.6.

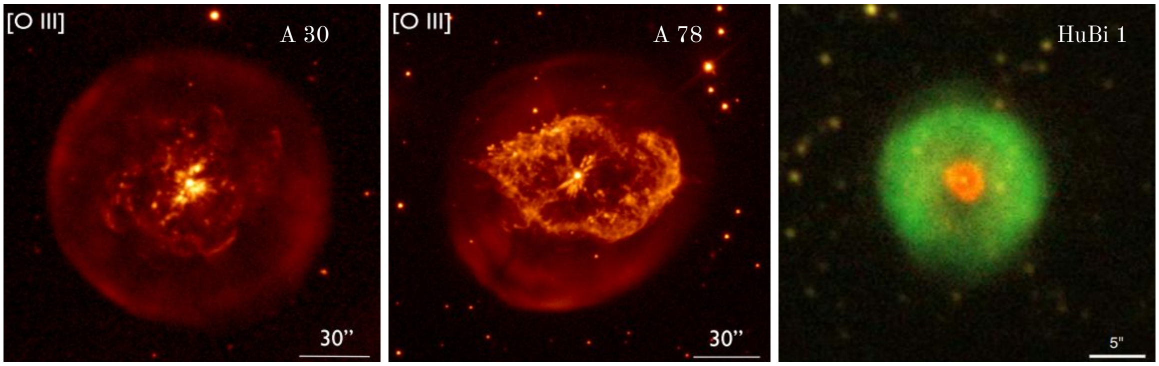

Figure 1.5: Some famous born-again PNe, from left to right we have A 30, A 78 and HuBi 1. A 30 and A 78 are optical [O III] images. A 30 image was obtained at the Kitt Peak National Observatory Mayall telescope and A 78 was obtained at the Nordic Optical Telescope (NOT), both were obtained with an [O III] filter and were taken from Toalá et al. (2021). For HuBi 1 we have a colour composite image obtained with NOT ALFOSC with the filters [N II] λ6584 (red) and Hα λ6563 (green) taken from Guerrero et al. (2018).

It was not until the early 90s when the born-again scenario became important, specifically, since the discovery of V 4334 Sgr (PN G 010.4+04.4) or as commonly known, the Sakurai's Object. In 1996 the amateur astronomer Y. Sakurai discovered that a star changed its brightness dramatically (Nakano et al., 1996) changing its magnitude in the J band from 21 to 9.16 mag (Duerbeck & Benetti , 1996; Nakano et al., 1996). For years, it has been one of the most studied born-again PNe due to dramatic changes in chemistry, luminosity, and temperature (see Fig. 1.7). Evans et al. (2020) demonstrated that the material ejected during the VLTP has cooled from $\sim$1000 to $\sim$180 K over 20 yr of evolution, creating a dust shell with a mass that has increased from 10^{-10} to 10^{-5} M$_{\odot}$. Additionally, FG Sge has been classified as a born-again object (Gehrz et al., 2005), although it has been argued that this object might have experienced its thermal pulse a bit earlier (Jeffery & Schönberner, 2006; Lawlor, 2023) it still fits within the definition of a born-again star. This classification applies to both late thermal pulses (LTP) and VLTP. The differences between these two types of pulses will be discussed in detail in the Section 4.2.

To date, no more than 10 PNe have been discovered that have been classified as part of the born-again PN sequence: A 30, A 58, A 78, the Sakurai Object, HuBi 1, NGC 40, NGC 5189, and the nebula around the star WR 72 (see Guerrero et al., 2018; Gvaramadze et al., 2020; Kimeswenger et al., 1998; Toalá et al., 2015, 2019a, and references cited there). Their progenitor stars share common characteristics: they are H-deficient, C-rich, and possess extended dust shells within their outer old PNe. The limited number of born-again PNe suggests a rare and short-lived occurrence requiring very specific conditions for a VLTP to occur. Indeed, models aiming to replicate the VLTP event in central of PNe result in duration similar to human time scales, ranging between 20 and 100 years (e.g., Miller Bertolami et al., 2006).

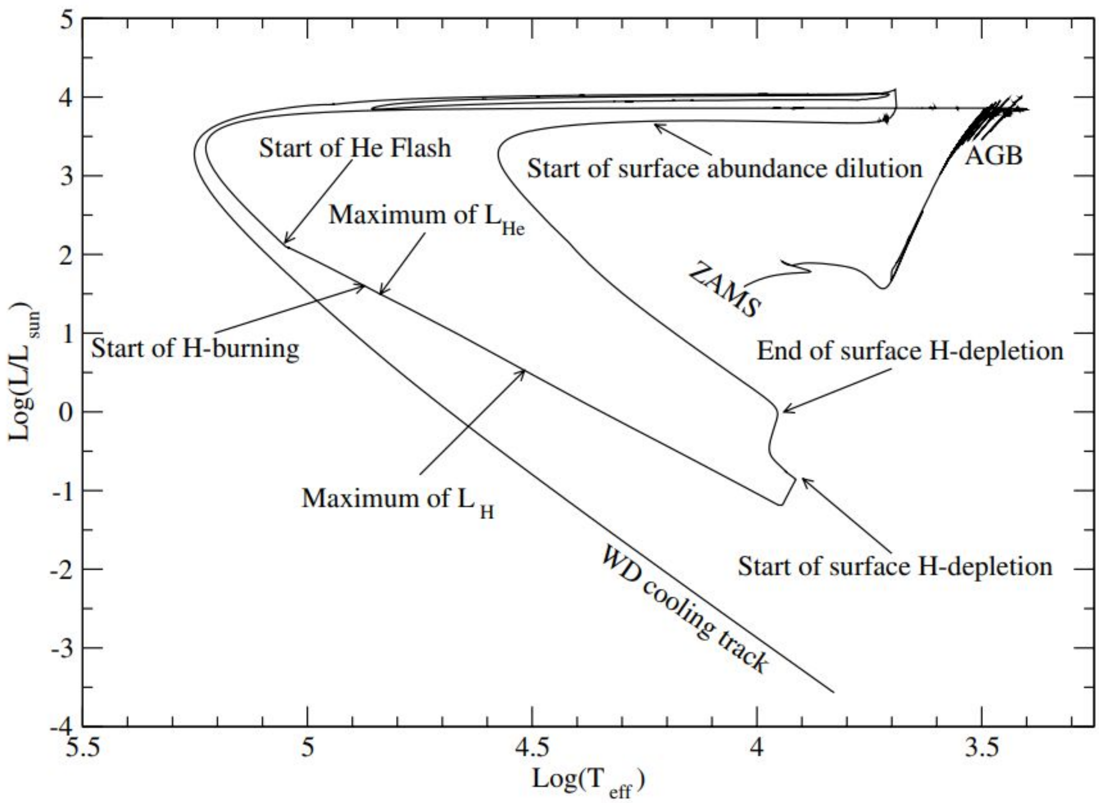

Figure 1.6: Evolutionary track of a stellar model with initial mass of 2.5 $M_\odot$ that experienced a VLTP. This figure has been taken from Miller Bertolami et al. (2006).

Guerrero et al. (2018) reported that the central star of HuBi 1 (Hu & Bibo, 1990) presented a very similar behavior to the Sakurai's Object. They showed that the central star of HuBi 1 decreased in brightness by a factor of 10,000 between 1971 and 2017 (see bottom panel of Fig. 1.7). The CSPNe of HuBi 1, IRAS 17514, has been exhibiting anomalous behavior characterized by the ejection of substantial amounts of C-rich material at velocities surpassing the expansion rate of the surrounding nebula. This rapid expansion shock-excites the inner shell, creating conditions conducive to the condensation of dust grains as the material disperses. **Due to the VLTP, the temperature of the star decreases to approximately 5000 K. As the star cools, the photons it emits have lower energy, reducing the energy transferred to the surrounding gas and dust during collisions. This decrease in energy reduces particle motion and temperature, facilitating dust grain formation as particles coalesce more easily. The increasing optical depth of the surrounding dusty cocoon further shields UV photons from the central star, enhancing cooling and triggering recombination processes in the outer nebula, a behavior distinct from what is typically observed in most CSPNe (Naito et al., 2012).**

HuBi 1 has been studied extensively through various methods, offering insights

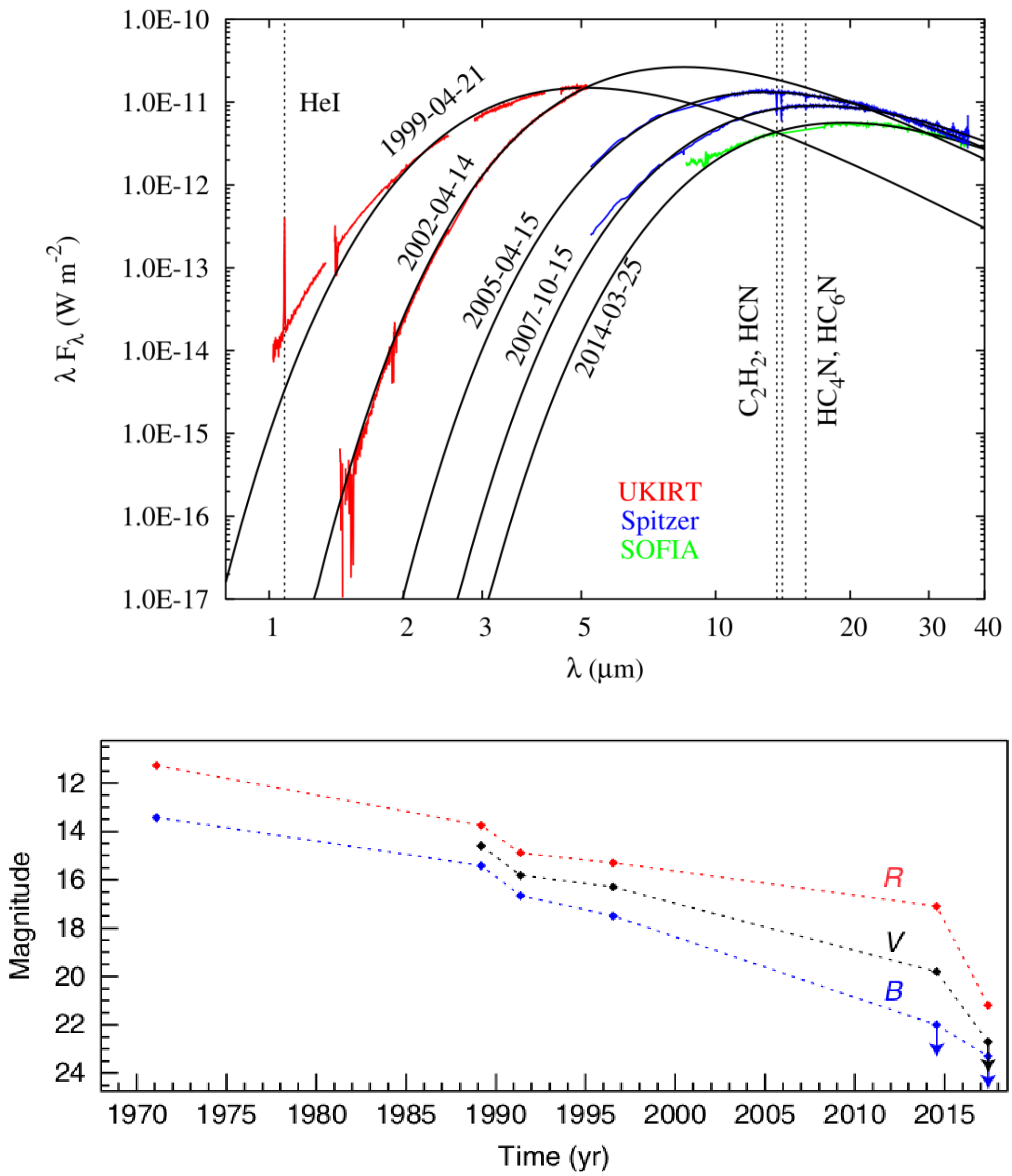

Figure 1.7: Top: Temporal evolution of the IR properties of the H-poor ejecta from the Sakurai Object (V 4334 Sgr) reported in Evans et al. (2020). Bottom: Evolution of the optical photometry of the central star of HuBi 1 in the B, V and R bands reported in Guerrero et al. (2018).

into its unique properties. For instance, the chemical abundances of HuBi 1 have been analyzed by Montoro-Molina et al. (2023), who provided a detailed account of the elemental composition of the nebula. Their study highlighted the presence of enhanced C and O abundances, which are indicative of a VLTP event. This analysis supports the classification of HuBi 1 as a born-again PN, characterized by its H-deficient and C-rich nature.

In addition to chemical abundance studies, the kinematics of the H-deficient ejecta of born-again PNe have been thoroughly investigated. Meaburn & Lopez (1996) and Meaburn et al. (1998) presented long-slit high-dispersion optical spectra of A 30 and A 78 and revealed a broad range of velocities for the H-poor clumps, varying from 40 to 500 km s^{-1}, suggesting complex dynamics. Observations also show that the expansion of these nebulae is not homogeneous, with interactions between different components contributing to the complexity of their evolution.

Furthermore, the study presented by Fang et al. (2014) also examines the expansion patterns of A 30 and A 78. These authors explored how these nebulae expand and how this behavior relates to their physical characteristics and evolution, offering additional insights into the expansion process. Notably, they found that the clumps closest to the central star (disk clumps) move faster than those further from the star (bipolar ejections).

More recently, the most comprehensive three-dimensional (3D) study of HuBi 1, a born-again planetary nebula, is that of Rechy-García et al. (2020b), which utilized Integral Field Unit (IFU) data. This work is notable for the precision and detail with which the nebula's structures were analyzed, providing a deep view of its morphology and dynamics. Their study highlights the velocity structure and expansion patterns within the nebula, revealing complex outflows and asymmetries that suggest a VLTP event. The kinematic data provided crucial information about the dynamical history of HuBi 1, indicating that the nebula has undergone significant structural changes, likely driven by episodic ejections associated with the born-again phenomenon. This work represents a significant advancement in understanding the 3D structure and evolution of such nebulae.

By examining the interplay between gas and dust, and understanding how these components interact and evolve, we can gain a more complete picture of the processes that govern the formation and evolution of the material in such PNe.

1.4 The binary dilema

In contrast to the stellar evolution models described above, some born-again PNe exhibit some characteristics that suggest they host a binary system as progenitor. For instance, optical and IR observations have demonstrated that the morphology of the H-poor ejecta around stars A 30, A 58, A 78, and the Sakurai Object is bipolar, formed by a disk and a pair of jets (Clayton et al., 2013; Fang et al., 2014; Hinkle & Joyce, 2014). Additionally, Wesson et al. (2018) showed that among PNe with the largest abundance discrepancy factor are A 30 and A 78, suggesting they harbor binary systems. However, the most controversial result for a decade has been related to abundances.

Lau et al. (2011) compared the abundances of H-poor material from A 30 and A 58 obtained by Wesson et al. (2003, 2008) with predictions from stellar evolution models (described in the previous section). They found that while stellar evolution models predict a carbon-to-oxygen mass ratio (C/O) > 1, abundances obtained from observations report values in the range of C/O ≈ 0.06–0.30. Lau et al. (2011) propose that it is very possible that the production and ejection of material within the old PN could take place as a result of a binary system. These autors propose that a binary system composed of an ONeMg primary white dwarf (WD) and an AGB secondary star will evolve such that the primary will accrete material from the companion AGB. The subsequent evolution of the AGB star will create the PN we see today. Following its evolution, the secondary star will produce a thermal pulse ejecting the H-poor processed material. In their table 1, Lau et al. (2011) present predictions of the C/O ratio from nova explosion models, resulting in values around 0.05–0.60, more consistent with values obtained from optical observations. However this scenario presents a few problems, as discussed in recent reviews on PN formation of H-deficient CSPNe by Miller Bertolami (2024). For instance, Lau et al. (2011) scenario would likely result in a double luminosity peak, which is not observed in A 30 nor A 58. Additionally, the initial configuration they propose is difficult to reconcile with realistic binary evolution pathways. Achieving this outcome would require highly fine-tuned conditions, such as specific orbital configurations and mass ratios, which are statistically unlikely. While the scenario successfully matches Ne abundances, this comes at the cost of failing to reproduce many other elemental abundances observed in H-deficient PNe.

In the previous sections, we have mentioned that after undergoing the VLTP, the star returns to the region of the HR diagram designated for AGB stars, reducing its $T_{\rm eff}$ below 10^4 K. This allows for the formation of dust and molecules from the H-poor, C-rich ejecta. Over the nearly 30-year post-VLTP evolution of Sakurai's Object, it has been demonstrated that C-rich dust is formed almost immediately. This process is triggered by the high metallicity of this material (Evans et al., 2020).

Recently, our group presented the most comprehensive study of dust characterization in the born-again PNe A 30 and A 78 in Toalá et al. (2021). Our observations demonstrate that C-rich dust (amorphous carbon, graphite, and PAHs) coexists with H-poor material and hot X-ray-emitting gas (Guerrero et al., 2012; Toalá et al., 2015) at distances of up to 40–50 arcsec from their CSPNe[1]. Using the radiative transfer code Cloudy (Ferland et al., 2017), we were able to reproduce the optical and IR observations of A 30 to study the ionized gas and dust present in this nebula. Our best model resulted in a total gas mass $M_{\rm gas} = 4.41^{+0.55}_{-0.14} \times 10^{-3} M_\odot$ with 35% of the mass in the outer shell. The total dust mass $M_{\rm dust} = 3.20^{+3.21}_{-2.20} \times 10^{-3} M_\odot$ with 95% in the outer shell. Thus, the total mass corresponding to the ejected mass during the VLTP in A 30 is $M_{\rm TOT}$=$7.61^{+3.76}_{-2.20} \times 10^{-3}$ M$_\odot$.

Taking into account both the mass of C and O in the gas as well as the mass of C in the dust, we find that C/O > 1.7–5.1. With this, we have demonstrated that the

[1]≈0.4–0.5 pc assuming a distance to A 30 of 2.4 kpc (Bailer-Jones et al., 2021).

H-poor ejecta of A 30 is consistent with a born-again evolution scenario in contrast to the binary scenario proposed by Lau et al. (2011).

1.5 Science goals

In this thesis we aim to deepen our understanding of the born-again phenomenon in PNe by approaching it from both observational and theoretical angles. Considering the current literature described in the referenced works above, it is necessary to produce modern stellar evolution models to address the duration of the VLTP event and study its energetic impact on the ejecta. Additionally, we will characterize the optical properties of born-again PNe as well as the presence of C-rich dust. Specifically, our objectives are:

- To comprehend the mechanism of H-poor material ejection.
- To develop stellar evolution models using modern tools, considering the VLTP scenario.
- To characterize born-again PNe through optical and IR observations.

This thesis is organized as follows. In Chapter 2, we present our Cloudy models of the born-again nebulae A 78 and HuBi 1. Additionally, we discuss how studying the dust within these types of nebulae helps us understand the origin of the H-poor material they contain. Chapter 3 focuses on a morpho-kinematic study of the H-poor clumps in the nebulae A 30 and A 78. A formation scenatio is proposed for born-again PN through common envelope mechanism. In Chapter 4, we present our stellar evolution models, examining the parameters that influence the occurrence of a late He flash and how this event impacts the star's evolution. We also address the challenges encountered in modeling such events. Finally, in Chapter 5, we present our general conclusions and discuss potential directions for future work.

1.6 Publications

The research presented in this thesis has led to several publications that contribute to the understanding of born-again PNe and related stellar evolutionary processes. These articles detail various aspects of the study, including observational data, morpho-kinematic and photoionization modeling. Each publication represents a significant step forward in the broader investigation of H-deficient nebulae and the mechanisms driving their formation and evolution.

The following is a list of articles derived from this work:

- *Common envelope evolution in born-again planetary nebulae - Shaping the H-deficient ejecta of A 30*, **Rodríguez-González, J. B.**; Santamaría, E.; Toalá, J. A.; Guerrero, M. A.; Montoro-Molina, B.; Rubio, G.; Tafoya, D.; Chu, Y. -H.; Ramos-Larios, G.; Sabin, L, 2022, MNRAS, 514, 4794

- *Carbon-rich dust in the born again planetary nebula A78*, **Rodríguez-González, J. B.**; Toalá, J. A. et al., 2024, submitted to MNRAS

- *Carbon-rich dust in the born again planetary nebula HuBi 1 (PM 1-188)*, **Rodríguez-González, J. B.**; Toalá, J. A. et al., in prep.

In addition, I also contributed to other works related with born-again PNe and other evolved stars:

- *Spectral Variability of the Born-again Ejecta in A 58*, Montoro-Molina, Borja; Guerrero, Martín A.; Toalá, Jesús A.; **Rodríguez-González, Janis B.**, 2022, ApJ, 934, 18.

- *First Images of the Molecular Gas around a Born-again Star Revealed by ALMA*, Daniel Tafoya , Jesús A. Toalá , Ramlal Unnikrishnan , Wouter H. T. Vlemmings , Martín A. Guerrero , Stefan Kimeswenger , Peter A. M. van Hoof , Luis A. Zapata , Sandra P. Treviño-Morales , and **Janis B. Rodríguez-González**, 2022, ApJL, 925, L4

- *Rings and arcs around evolved stars - III. Physical conditions of the ring-like structures in the planetary nebula IC 4406 revealed by MUSE*, Ramos-Larios, G.; Toalá, J. A.; **Rodríguez-González, J. B.**; Guerrero, M. A.; Gómez-González, V. M. A., 2022, MNRAS, 513, 2862.

- *Tidal forces effects produced by planets around evolving Solar-like stars*, Maldonado, R.F., Toalá, J.A., **Rodríguez-González, J. B.** and Tamayo, D., submitted to MNRAS

Chapter 2

Radiative-transfer models of born-again PNe

As mentioned in the previous chapter, until recently the born-again scenario could not explain the observed abundances of born-again PNe. The main reason is that the C dust was not taken into account. Toalá et al. (2021) showed, for A 30, that if we consider the C trapped in the dust we could reproduce the C/O expected from a born-again event. In this chapter we expand this study to other born-again PNe to prove if we could reproduce the C/O that the evolution models predict for this type of event.

2.1 Observations

The photoionization model of a source can be considered suitable if it reproduces all available observations of sufficient quality. It thus requires, an obvious preliminary step, to compile as many available observations and to examine critically their quality and reliability.

2.1.1 Photometry of born-again nebulae

We retrieved the photometric data from the VizieR Photometry viewer[1] for A 78 and HuBi 1. Our searched was performed requesting all photometric measurements within 30 and 2 arcsec from the CSPN of A 78 and HuBi 1, respectively. This resulted in a large number of data points given that these are extended sources. Thus, we filtered some of the photometric measurements by inspecting the visibility window from this online tool to discriminate values corresponding to background sources. Furthermore, to ensure that the IR SED was reliable in the IR range we only considered photometric data with available uncertainties. In the case of A 78 VizieR also includes optical photometric data derived from *XMM-Newton* observations (Toalá et al., 2015). Those measurements do not include uncertainties, but, since these points

[1] `http://vizier.cds.unistra.fr/vizier/sed/`

are important to constrain the stellar continuum, we decided to keep them. All the available photometric data for A 78 and HuBi 1 are listed in Table 2.1.

In the case of HuBi 1 we also calculated the IR SED of the inner region, since we are interested in characterizing the dust produced by a possible VLTP in the inner region, we want to subtract the contribution of the outer nebula.**Unlike A78, where photometry could not be calculated due to the lack of clear contours for the inner regions, HuBi 1 benefited from well-defined contours that were crucial for separating the inner and outer regions. This distinction was not possible for A78 because images from telescopes like WISE and others were saturated, making it difficult to distinguish between the two regions.** We used publicly available IR observations from *WISE*, *IRAS* and *Akari* telescopes which together cover the 3–160 μm wavelength range. These observations were retrieved from the NASA/IPAC Infrared Science Archive. The details of the observations are listed in Table 2.2.

For the photometric extraction procedure, we started by defining a region that covered the nebular emission. Its flux is simply defined as the sum of the contribution of all pixels inside this region. We then select different regions of the nebula's neighborhood to estimate the mean background contribution. We subtracted each background from the nebular flux density in order to obtain n background-subtracted fluxes for each IR wavelength image. The mean and standard deviation of these values then give us the final flux value and measurement uncertainty ($\sigma_{\rm back}$), respectively. The total error ($\sigma_{\rm tot}$) for IRAS and Akari was calculated as the standard deviation while for *WISE* was calculated as:

$$\sigma_{\rm tot} = F_{\rm s}\sigma_{\rm cal}, \tag{2.1}$$

where $F_{\rm s}$ is the source flux in each band and $\sigma_{\rm cal}$ is the calibration uncertainty. The *WISE* callibration uncertainties are 2.4, 2.8, 4.5, and 5.7 percent for the W1, W2, W3, and W4 bands, respectively[2].

For WISE, these additional instrumental uncertainties were included to account for the filter-specific errors that can significantly affect the measurements. In contrast, no such filter-dependent instrumental errors were reported for IRAS and Akari, allowing the standard deviation alone to represent the total error.

In most cases, the IR images of HuBi 1 do not provide enough resolution to clearly distinguish the dust emission in the inner regions. However, by subtracting the emission from the outer H-rich nebula, which originates from earlier evolutionary phases, we can isolate the emission from the inner region affected by the VLTP. This process ensures that the SED we analyze corresponds primarily to the emission from the H-deficient material in the inner regions, which is more directly related to the star's recent evolution and the VLTP event.

[2]See the Explanatory Supplement to the WISE Preliminary Data Release Products (`https://wise2.ipac.caltech.edu/docs/release/prelim/expsup/`)

Table 2.1: Details of publicly available photometry of A 78 and HuBi 1 extracted from the VizieR Photometry Viewer.

	λ [μm]	Flux [Jy]	error [Jy]	Year	Instrument
	0.54	2.16×10^{-2}	...	2013	XMM OM
	0.54	1.68×10^{-1}	...	2013	XMM OM
	0.54	2.52×10^{-1}	...	2013	XMM OM
	0.54	2.14×10^{-2}	...	2013	XMM OM
	0.54	2.12×10^{-2}	...	2013	XMM OM
	3.35	8.00×10^{-3}	0.11×10^{-3}	2013	WISE
	4.60	4.00×10^{-3}	0.50×10^{-3}	2013	WISE
A 78	8.28	0.61	0.03	2013	MSX
	8.61	0.99	0.03	2007	AKARI
	11.60	6.00	0.03	2010	WISE
	18.40	30.50	0.60	2007	AKARI
	21.30	33.20	2.00	2010	MSX
	65.00	123.0	9.00	2010	AKARI
	90.00	76.9	7.9	2010	AKARI
	140.00	33.60	2.4	2010	AKARI
	160.00	31.1	2.9	2010	AKARI
	550.49	1.34	0.18	2013	Planck
	550.49	1.48	0.61	2013	Planck
	550.49	1.35	0.15	2013	Planck
	2.16	0.20	0.004	2008	2MASS
	2.19	0.19	0.004	2008	2MASS
	3.35	1.44	0.06	2015	WISE
	3.35	0.88	0.02	2015	WISE
	3.35	1.28	0.18	2015	WISE
	4.60	4.66	0.55	2010	WISE
	4.60	5.43	0.24	2012	WISE
HuBi 1	8.61	6.84	0.02	2006	AKARI
	11.60	6.45	0.17	2010	WISE
	12.00	2.83	0.20	1992	IRAS
	18.40	4.78	0.04	1992	IRAS
	22.10	4.81	0.06	2010	WISE
	25.00	12.72	0.89	1992	IRAS
	60.00	9.60	0.67	1992	IRAS
	65.00	1.62	0.11	2006	AKARI
	90.00	0.84	0.05	2006	AKARI

Table 2.2: Details of the IR observations used in the photometric analysis of HuBi 1.**The data are categorized into different levels of processing, which indicate the degree of preparation applied to the observations. Level 1 corresponds to raw, unprocessed data, representing the original observations. Level 2 includes data that have been corrected for instrumental effects, ensuring a more reliable measurement. Finally, Level 3 represents science-ready data, which have been fully corrected for instrumental effects and calibrated, making them suitable for detailed scientific analysis.**

Instrument	Date (yyyy-mm-dd)	Obs. ID	λ_c (μm)	Processing level
IRAS	1992-04-10	f153h000	12, 25, 60, 100	level 3
Akari	2006-01-01		65, 90, 140, 160	level 3
WISE	2010-03-18	2688m167_ac51	3.4, 4.6, 12, 22	level 3

2.1.2 VLT Visir data for HuBi 1

We acquired mid-infrared narrow-band images using the Very Large Telescope (VLT) Imager for the mid-InfraRed (VISIR; Lagage et al., 2004) of HuBi 1 on 2018 September 13-14 (Program 2101.D-5047 A, PI: M. A. Guerrero).

The images of HuBi 1 were obtained using the PAH1 (λ_c=8.58 μm and FWHM=0.41 μm), SIV1 (λ_c=9.81 μm and FWHM=0.19 μm), and SIV (λ_c=10.47 μm and FWHM=0.17 μm) narrow-band filters with total exposure times of 12×0.021 s (0.252 s), 4×0.021 s (0.248 s) and 4×0.062 s (0.084 s), respectively. **We obtained a spectrum using VISIR that shows some features, such as the PAH at λ_c = 8.58 μm. However, this spectrum is not included in this thesis because, due to instrumental issues and errors during the observation process, the calibration star was not observed. As a result, the flux calibration of the spectrum was not performed correctly, rendering the data unsuitable for precise analysis.** The VLT VISIR images are presented in Figure 2.1. Images of a stellar source obtained immediately after these observations have a full width half maximum (FWHM) of 0.35 arcsec.

2.1.3 *Spitzer* Spectra

We inspected the *Spitzer* IR observations of HuBi 1, which were downloaded from the NASA/IPAC Infrared Science Archive[3]. HuBi 1 was observed with the *Spitzer* Infrared Spectrograph (IRS) on 2005 April 19 in staring mode. The observations correspond to program ID. 3633 (PI: M. Bobrowsky; AORKey: 11324672) and were obtained with the short-low (SL) module, which covers the 5–14.5 μm wavelength range. The slit position of these observations is showed in the upper left panel of Fig. 2.2 overplotted on a colour-composite image of HuBi 1. We note that the slit did not capture the central region of HuBi 1 and thus some flux was lost. In addition

[3]https://irsa.ipac.caltech.edu/frontpage/

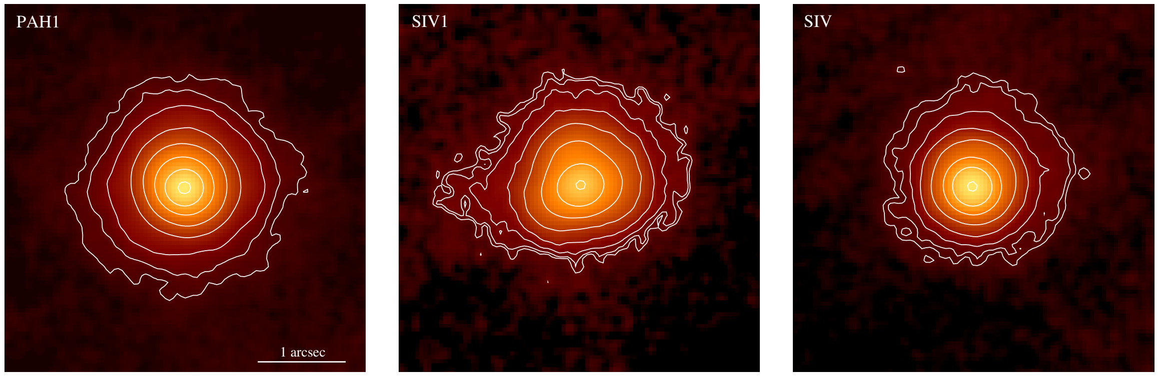

Figure 2.1: VLT VISIR images of HuBi 1 obtained in the PAH1 8.58 μm (left), SIV1 9.81 μm (middle) and SIV 10.47 μm (right) narrow-band filters. The contour levels illustrate the extended emission. All images have the same field of view. North is up, east to the left.

the *Spitzer* IRS data also include observations obtained with the short-high (SH) and long-high (LH) high-resolution modules, but these do not include background regions and thus, these were discarded.

We processed the *Spitzer* IRS data using the CUbe Builder for IRS Spectra Maps (CUBISM; Smith et al., 2007). The source and background regions are illustrated in the bottom right panel of Fig. 2.2.

2.2 PyCloudy Models

To characterize the total mass of dust and gas present in A 78 and HuBi 1, we have used the photoionization code Cloudy (version 23.0; Chatzikos et al., 2023). To obtain the most accurate model for each nebula, Cloudy requires the user to specify different properties such as:

- **The shape of the incident spectrum**. The spectrum of the CSPN of born-again PNe have very similar feature to the CSPNe of Wolf-Rayet-type, for this reason we used the NLTE stellar atmosphere code PoWR[4] to obtain the best stellar atmosphere model of the CSPN of each nebula. The details of A 78 and HuBi 1 CSPNe models are presented in Toalá et al. (2015) and Guerrero et al. (2018), respectively . We selected these models over blackbody approximations, as the winds from the CSPN of born-again PNe absorb a large portion of the UV radiation emitted by the star. This absorbed radiation is reprocessed and re-emitted at longer wavelengths, significantly reducing the total UV flux. This situation is illustrated in Fig. 2.3 where we present the best model of the CSPN of A 78 (left panel) and HuBi 1 (right panel) in comparison with a blackbody emission model with the same $T_{\rm eff}$. For A 78, the PoWR model has been scaled

[4] https://www.astro.physik.uni-potsdam.de/PoWR/

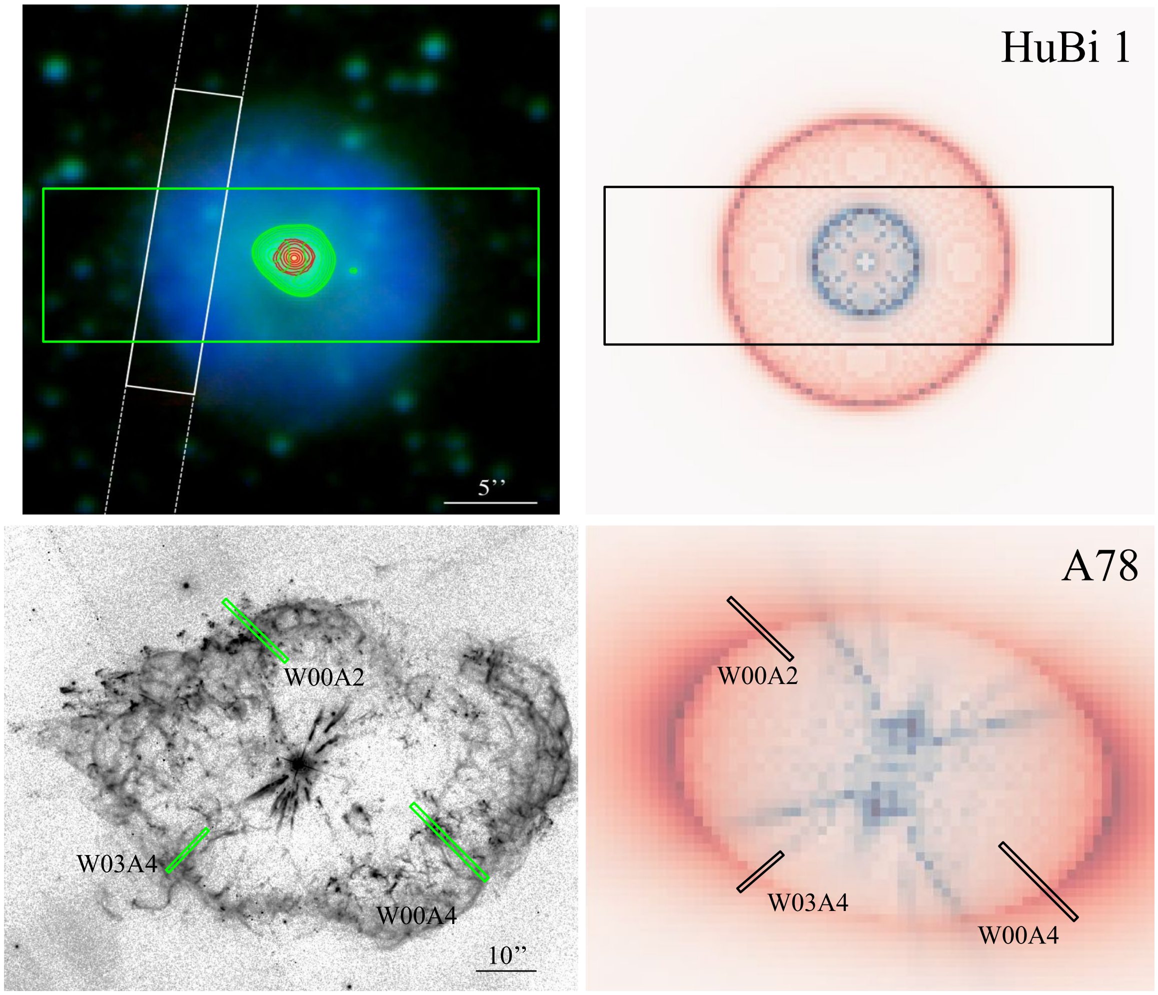

Figure 2.2: Left panels: For HuBi 1 (top), the color-composite image shows Hα (blue) and [N II] (green contours) images obtained from the Nordic Optical Telescope, originally presented in Guerrero et al. (2018). The red contours represent the VISIR PAH1 filter image (see Sec. 2.1.3 and Fig. 2.1). The solid and dashed white regions indicate the areas where the source and background spectra were extracted from the *Spitzer* IRS data (refer to Section 2.1.3). The green box represents the observed slit from GTC OSIRIS with a spatial scale of 0.254 arcsec per pixel and a spectral dispersion of 2.12 Å per pixel from Montoro-Molina et al. (2022). For A 78 (bottom), the *HST* WFC3 F502N image is displayed. The labeled slits W00A2, W03A4, and W00A4 come from Montoro-Molina et al. (2023), with a spatial scale of 0.19 arcsec per pixel and a dispersion of 0.49 Å per pixel. Right panels: Synthetic density maps generated with PyCloudy, where blue represents the inner shell and red represents the outer shell. The black rectangular regions correspond to the regions of extraction of the synthetic spectra.

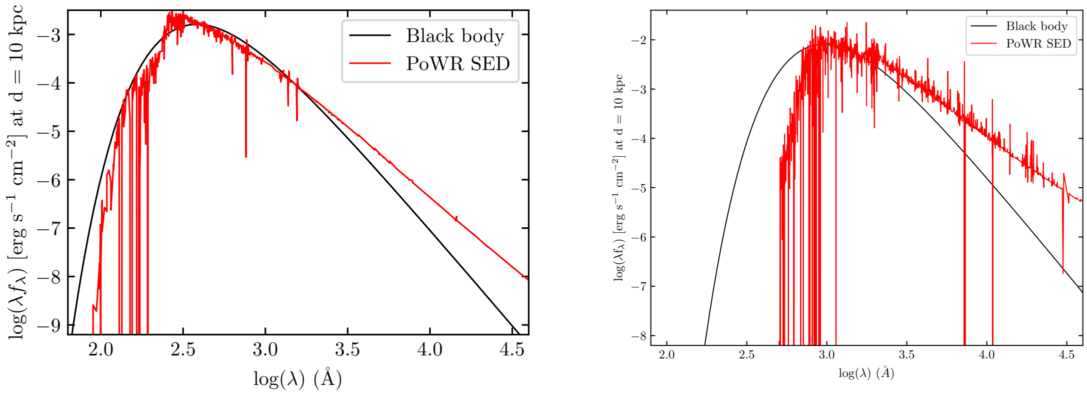

Figure 2.3: Comparison between the NLTE stellar atmosphere model of the CSPN of A 78 (left panel) and HuBi 1 (right panel) produced with the PoWR code (red) with a black body emission model (black) with an effective temperature of $T_{\rm eff}$=117,000 K (A 78) and $T_{\rm eff}$=38,000 K (HuBi 1).

to a $\log(L/{\rm L}_\odot) = 3.94$ (corresponding to the estimated distance of 1.7 kpc) and $T_{\rm eff} = 117$ kK. While for HuBi 1 the best fit to the observed properties of the CSPN of HuBi 1 resulted in $\log(L/{\rm L}_\odot)$=3.8±0.3 and $T_{\rm eff}$=38,000±2,000 K.

- **Nebular abundances**. Recently, Montoro-Molina et al. (2023) used medium-resolution optical spectra obtained with different instruments to study the physical properties of the H-deficient ejecta in A 78. They also produced the most accurate He, O, N, Ne and S abundances calculations of the the inner knots and intermediate eye-like structures. We will adopt the abundances of these elements in our model. While for HuBi 1 the chemical abundances were adopted to be those estimated by Peña et al. (2021) for the outer nebula and by Montoro-Molina et al. (2022) for the inner region. All the abundances are listed in Table 2.3.

- **The gas distribution (density and filling factor)**. Taking into account the apparent morphology seen in the observed images (see left panels of Fiure 2.2), we tried to reproduced them with relatively basic geometries in Cloudy. So for A 78 we considered two structures to model its nebular and IR properties. A dense torus-like structure surrounding the CSPN with inner and outer radii of $r_{\rm in} = 2.8$ and $r_{\rm out} = 10$ arcsec, respectively. These radii have been obtained by averaging the distances of the dense H-deficient clumps in the disrupted disk around the CSPN of A 78 (see Fang et al., 2014). Throughout this chapter, the modeled torus in Cloudy is referred to as the inner shell in our model, representing the structures of the H-deficient clumps found in the disrupted disk. We set the height scale (h) of the torus to be the same as $r_{\rm in}$, that is, h=2.8 arcsec. This assumption was made because the height of the disk is unknown, and we believe the best approach is to assume it has a size similar to the inner radius. A second hollow ellipsoidal structure was defined surrounding the torus, which we will refer to as the outer shell. Its total extension was defined as 42×45 arcsec^2, with the hollow extension of 10×17 arcsec^2.

For the VLTP ejecta of HuBi 1, we decided to adopt a spherically-symmetric VLTP structure divided into inner and outer VLTP shells. The inner VLTP shell is defined by an inner radius $r_{\rm in}$ and the total extension of the outer VLTP shell is defined by $r_{\rm out}$, with $r_{\rm mid}$ defined as the separation between the two structures. The only well-constrained measurement is the size of the outer H-rich shell, derived from VISIR images, while its starting point (inner radius) is unknown. Consequently, the inner radius of our internal shell was treated as a free parameter, with $r_{\rm in} = 0.05$ providing the best fit to the shape of the SED. The radius of our two shell were set to $r_{\rm in}$=0.05, $r_{\rm mid}$=0.2 and $r_{\rm out}$=2.2 arcsec. A schematic view of the models geometry structures is presented in Fig. 2.4.

The total number densities and filling factors of the two structural components are denoted as n_1, n_2, ϵ_1 and ϵ_2, respectively. The filling factor is a parameter that quantifies the fraction of the nebula's volume that is actually filled with gas. In many nebulae, gas is not evenly distributed; instead, it is clumpy or filamentary, with some regions containing dense clouds of gas and others being relatively empty. A filling factor less than 1 means that not all the volume is occupied by gas, which allows for high local densities in these clumps without requiring a high average density across the entire nebula. In Cloudy, the filling factor affects the emission line intensities, ionization structure, and cooling rates, as denser clumps within the nebula will contribute more to the observed spectra.

For both structures we adopted density distributions with a dependence on the radius such as

$$n(r) = n_{\rm i} \left(\frac{r}{r_{\rm i}} \right)^{-\alpha}, \qquad (2.2)$$

where $n_{\rm i}$ is the total number density of the gas at the inner face of each structure, which is coincident with their inner radii.

- **Dust properties**. There is a large number of works in the literature that have demonstrated that the dust in born-again PNe is predominantly composed by C-rich species. Even just a couple of years after experiencing their VLTP, the Sakurai's Object and A58 exhibited C-rich species in their IR spectra (Clayton & De Marco, 1997; Eyres et al., 1998) . Particularly for A 30, Greenstein (1981) demonstrated that its dust has a peculiar composition with the peak of the extinction curve near 2470 Å instead of the typical 2200 Å of the ISM. Greenstein (1981) found that the properties of the dust in A 30 are best explained purely by C-rich dust species.

  After this consideration, we decided to use only C-rich dust in our models calculations. Particularly, we used predefined amorphous carbon included in Cloudy (Rouleau & Martin, 1991). To establish the best size distribution of the dust grains we ran a number of Cloudy models to determine those fitting better

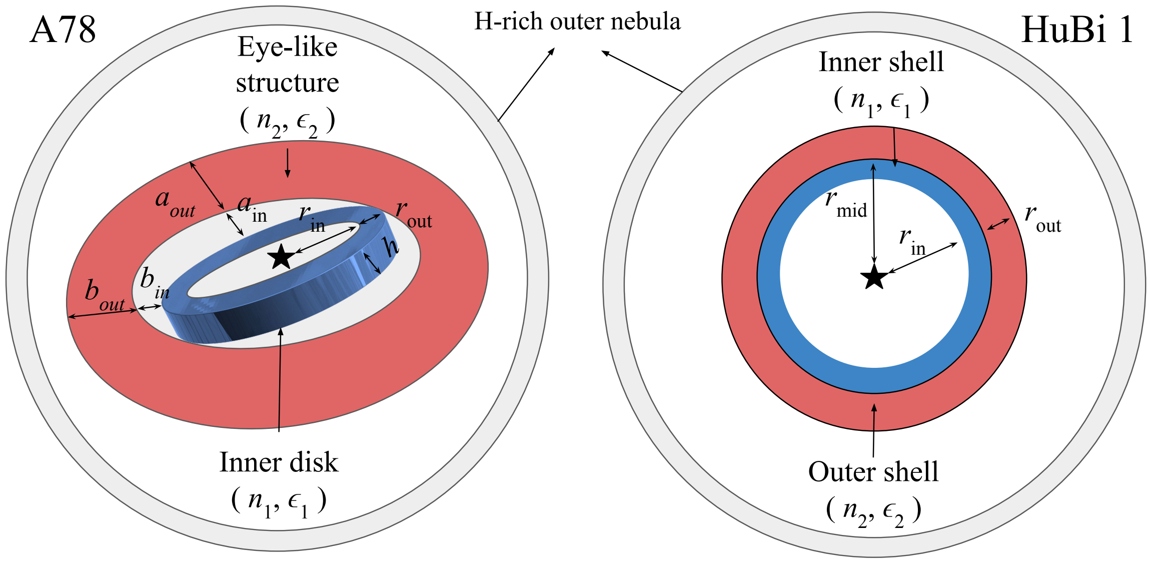

Figure 2.4: Schematic representation of the different shells adopted for the Cloudy model of A 78 (left) and Hubi 1 (right). The relative size and orientations of the shells are not to scale.

the IR SED. We initially adopted a similar approach as that employed for A 30 in the study conducted by Toalá et al. (2021). Those authors determined that a power law distribution of dust sizes, with $\propto a^{-3}$, provided the best fit to the IR SED of A 30 (see also Borkowski et al., 1994).

It is important to note that the search for the best model, one that simultaneously reproduces the best the nebular emission lines and the IR photometry, is an iterative process. A large number of models varying the different free parameters (such as n, ϵ, a, porosity of the grains and dust-to-gas ratio) were performed. We started by adopting certain density values, which impact directly the optical emission lines. Then, the IR properties are evaluated. The model parameters are then adjusted to fit a desirable value. In some cases, some parameters impact others creating a degeneracy. In the next section we describe in detail this degeneracy. The best model was selected by assessing their χ^2 statistics when compared with the observations.

For a direct comparison with observations we used the pyCloudy routines (Morisset, 2013) to produce the synthetic density map shown in the right panels of Fig. 2.2, in which the blue shades correspond to the inner shell and the red shades to the outer shell. pyCloudy routines were also used to extract synthetic slit (black boxes in Fig. 2.2) information from the projection of our 3D model.

2.3 Abell 78

As mentioned before, we require that our best Cloudy model to be able to reproduce, as best as possible, the Hα emission line, as this provides a reliable estimate of the

Table 2.3: Total number abundance values for A 78 from Montoro-Molina et al. (2023) and HuBi 1 from Montoro-Molina et al. (2022). The abundance values are listed such that $\log X(\mathrm{H}) = 12$.

	A 78		HuBi 1	
Element	Disk & Tails	Eye-like Structure	Outer Shell	Inner Shell
He	14.23	11.16	11.13	13.00
C	...	...	...	9.53
N	9.85	7.62	7.87	9.90
O	10.82	8.26	8.04	9.80
Ne	12.16	7.74	...	9.03
S	8.09	6.02	7.18	...

total gas mass. A summary of the parameters for our best model is presented in Table 2.4. Additionally, a comparison between our best model and the observed SED is also presented in Fig. 2.5. We particularly show the contribution from the inner and outer shells with dashed and dottes lines, respectively. We found that the inner and outer VLTP shells require number densities of approximately n_1=1300 cm^{-3} and n_2=80 cm^{-3}, respectively, in order to produce an acceptable synthetic Hα and Hβ fluxes from our synthetic slits. This parameter give a difference between model and observation of less than 3 per cent for the Hα line and about 22 percent for the Hβ emission for W03A4 slit. However, this combination of parameters produce between 2–3 times higher flux for the Hα and Hβ emission lines from the W00A3 and W00A4 synthetic slits. If one tries changing the parameters of the density distribution (n and ϵ) to better tailor the fluxes from another synthetic slit, the other two predict different fluxes that again range the observed values with factors between 2–3. We attribute these differences to the clumpy distribution of material from the eye-like structure in A 78, in particular in those regions of slits W00A2 and W00A4, which seem to be broader and more turbulent that the region of W03A4.

Table 2.5 compares the fluxes from the Hα and Hβ as well as those obtained from representative ions from our pyCloudy model with those reported by Montoro-Molina et al. (2023). Those of [N II] are also well reproduced by the W03A4 and W00A4 slits, but not that good in the W00A2 slit. We particularly note the discrepancy in the [O III] emission lines. Our model over-predicts the emission of [OIII] 5007 Å of slit W00A2, but for the other two slits the synthetic emission is below that of the observations. It is very likely that this situation only reflects the non uniform abundance of O within the different H-deficient clumps (see for example the case of A 30 in Simpson et al., 2022). To further assess this situation, we calculated averaged lines fluxes for our synthetic slits and the observed ones, which we list in the last two columns of Table 2.5. We note that the averaged values of Hα and Hβ provide a closer representation of the observed emission, even though the fit is not yet perfect. It is important to keep in mind that the observed fluxes correspond to specific regions of the nebula, whereas our model assumes a homogeneous distribution, which we know is not the case for A 78. Despite these discrepancies, we consider this model to be the

Table 2.4: Details of our best Cloudy model for A 78 adopting amorphous carbon with a porosity of 10 percent for the inner shell and 50 per cent for the outer structure.

Parameter	Units	Model
Inner VLTP shell		
n_1	[cm^{-3}]	1,300
α		2
ϵ_1	[10^{-6}]	8
$r_{\rm in}$	[arcsec]	2.8
$r_{\rm out}$	[arcsec]	10
h	[arcsec]	2.8
$a_{\rm small}$	[μm]	0.0009–0.009
$a_{\rm med}$	[μm]	0.003–0.05
$M_{\rm gas}$	[10^{-5}M$_\odot$]	2.6
$M_{\rm dust}$	[10^{-7}M$_\odot$]	5.0
Dust-to-gas		0.02
Outer VLTP shell		
n_2	[cm^{-3}]	80
α		2
ϵ_2	[10^{-4}]	1
$a_{\rm in}$	[arcsec]	17
$a_{\rm out}$	[arcsec]	45
$b_{\rm in}$	[arcsec]	10
$b_{\rm out}$	[arcsec]	42
$a_{\rm large}$	[μm]	0.04–0.07
$M_{\rm gas}$	[10^{-6} M$_\odot$]	2.8
$M_{\rm dust}$	[10^{-5} M$_\odot$]	1.9
Dust-to-gas		6.60
Total properties of the model		
$M_{\rm TOT,gas}$	[10^{-5} M$_\odot$]	2.8 ± 0.4
$M_{\rm TOT,dust}$	[10^{-5} M$_\odot$]	1.9 ± 0.2
C/O		17.72 ± 0.08

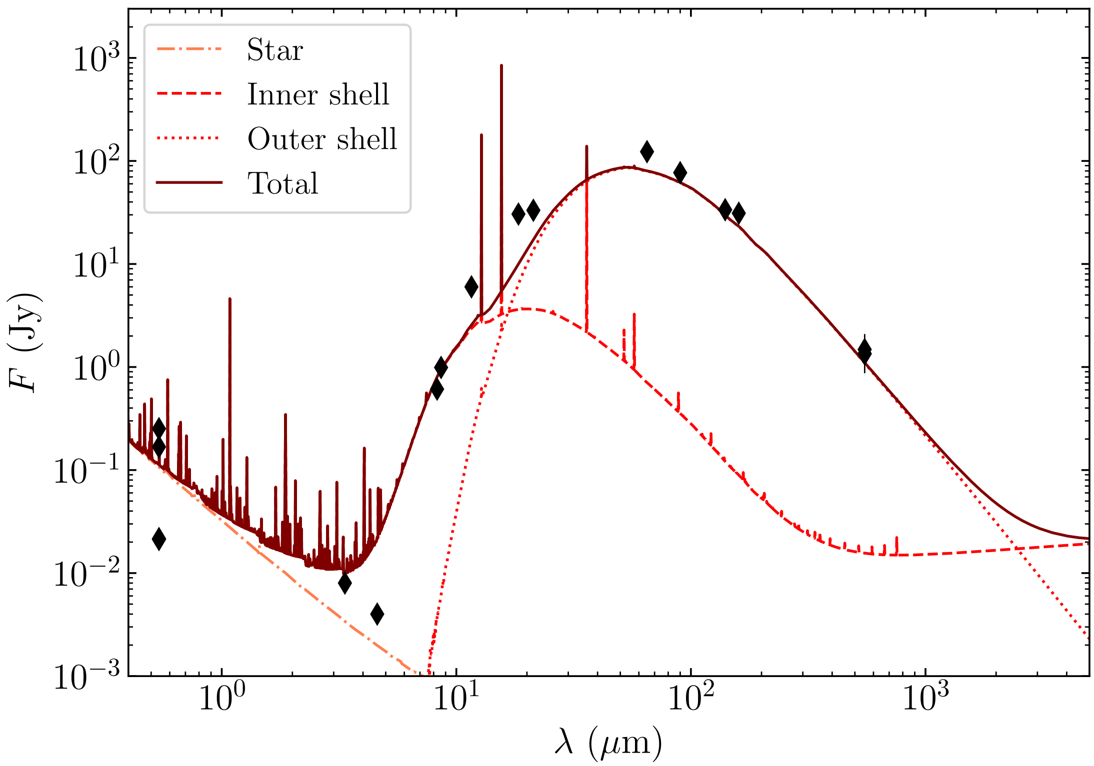

Figure 2.5: Observed SED of A 78 (black diamonds). Our best Cloudy model of A 78 is shown with a solid line. The contribution from the inner shell (with dust populations with 10 per cent porosity) and that of the outer shell (with dust population with 50 per cent porosity) are illustrated with dashed and dotted lines, respectively. Note that below 3 μm we have only the contribution of the CSPN shown with a dash-dotted line.

best representation of the emission lines available.

The next step is to reproduce the IR photometry, which is modelled through the combination of the gas filling factor (ϵ), the dust size distribution (a) and dust-to-gas (D/G) ratio. We found out that for the inner shell of A 78 the model requires the presences of two amorphous carbon dust families with sizes in the range of 0.0009–0.009 and 0.003–0.05 μm, which we have labelled small- ($a_{\rm small}$) and medium-size ($a_{\rm med}$) dust distributions. For the outer shell we used only one large dust population with sizes $a_{\rm large}$=0.04–0.07 μm. We found that a good model was achieved with $\epsilon_1 = 8 \times 10^{-6}$, $\epsilon_2 = 1 \times 10^{-4}$, and D/G ratios of 0.05 and 21 for the inner and outer shells, respectively. To illustrate the impact of varying these values, we particularly show in Fig. 2.6 the results for the outer shell, from which the degeneracy generates remarkable differences. The three panels show the SED of our CLOUDY models as solid lines, while the black diamonds represent the observed photometry. The different colors correspond to various models.

In the first panel, changes in the electron density significantly affect the shape of the SED, especially in the mid-infrared region, where higher densities shift the emission peaks and modify the model's agreement with the observed fluxes. The second panel focuses on how the variation of the parameter ϵ for the outer shell influences the accuracy of the model. As ϵ increases, the model tends to better reproduce the infrared flux. However, differences in the goodness of fit (χ^2) across different wavelengths highlight the degeneracies present, indicating that multiple parameter combinations can produce fits similar to the observed photometry. Finally, the third panel illustrates the effect of different D/G ratios on the model. A range of D/G ratios from 3.5 to 9.4 is shown, which affects both the overall level and shape of the SED. These variations have a significant impact on the model's ability to reproduce specific features in the infrared region. For the outer shell, a higher D/G ratio aligns the model better with the observed data.

This analysis demonstrates that the greatest degeneracy in the parameter space occurs between $n_{\rm e}$ and ϵ. It is possible to achieve a similar model fit by increasing $n_{\rm e}$ while decreasing ϵ, emphasizing the need for additional observational constraints to better refine the model. Restricting these parameters poses significant challenges, particularly because, while we may know the density in certain regions of the nebula, the model assumes a homogeneous medium, which is not typically the case for PN. In reality, these nebulae often exhibit regions of significantly higher density. The filling factor, in particular, is notoriously difficult to constrain observationally because it describes the fraction of the volume occupied by dense clumps within a more diffuse medium. Studies in the literature, such as Osterbrock & Ferland (2006) and Ferland et al. (2017), have shown that without detailed spatial information or high-resolution imaging, the estimation of ϵ becomes highly uncertain and is often treated as a fitting parameter rather than a directly measurable quantity. This complicates efforts to accurately characterize the physical conditions in PNe and underscores the necessity of complementary observations to better understand the density structure and filling factor. Nevertheless, within these limitations, the values we are adopting seem to produce a model that is capable of reasonably reproducing both the SED and the Balmer lines.

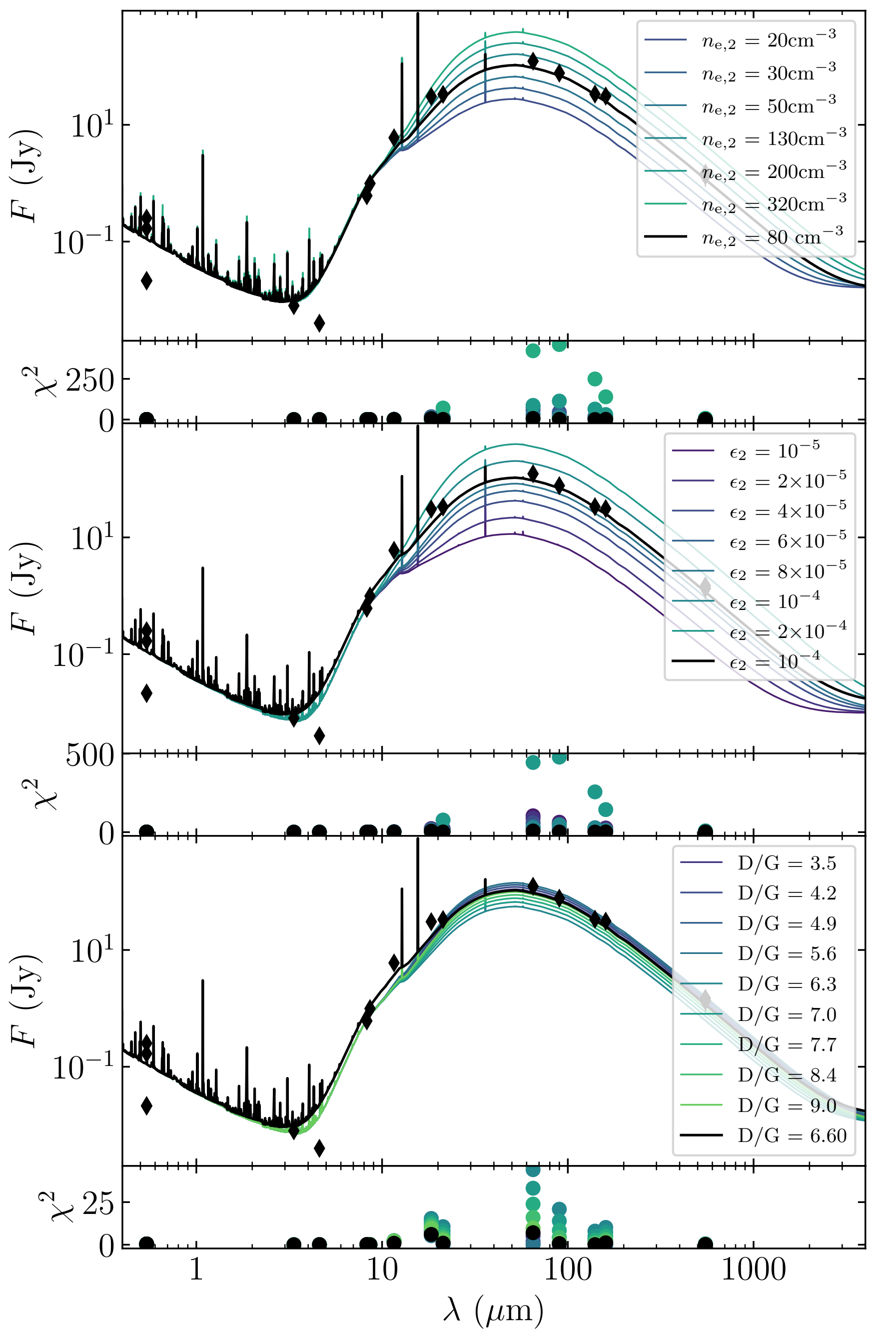

Figure 2.6: Cloudy A 78 models considering different values for the number density n (top), filling factor (middle) and D/G (bottom) for the outer shell.

Table 2.5: Best-fit Cloudy of A 78 model predictions of emission lines compared with results for slits W00A2, W03A4, and W00A4 presented in Montoro-Molina et al. (2023). The flux of the emission lines is expressed in erg/s/cm^2/Å.

Line	W03A4		W00A2		W00A4		Average	
	Model	Observed	Model	Observed	Model	Observed	Observed	Model
$\log(F_{[\mathrm{O\,III}]4363})$	−16.06	−15.35 ± 0.055	−14.73	−15.32 ± 0.032	−14.91	−15.09 ± 0.020	−14.97	−15.24 ± 0.019
$\log(F_{\mathrm{He\,II}4686})$	−15.59	−15.11 ± 0.022	−14.69	−14.79 ± 0.007	−14.74	−14.71 ± 0.006	−14.86	−14.84 ± 0.012
$\log(F_{\mathrm{H}\beta})$	−15.25	−15.14 ± 0.020	−14.59	−14.95 ± 0.011	−14.77	−14.93 ± 0.009	−14.79	−15.00 ± 0.007
$\log(F_{[\mathrm{O\,III}]4959})$	−15.34	−14.35 ± 0.061	−14.05	−14.30 ± 0.004	−14.23	−14.05 ± 0.003	−14.29	−14.21 ± 0.015
$\log(F_{[\mathrm{O\,III}]5007})$	−14.86	−13.82 ± 0.001	−13.57	−13.78 ± 0.001	−13.75	−13.56 ± 0.003	−13.81	−13.70 ± 0.019
$\log(F_{[\mathrm{N\,II}]6548})$	−15.88	−15.88 ± 0.045	−15.82	−16.44 ± 0.140	−15.79	−15.69 ± 0.018	−15.83	−15.91 ± 0.023
$\log(F_{\mathrm{H}\alpha})$	−14.71	−14.70 ± 0.004	−14.03	−14.51 ± 0.002	−14.22	−14.48 ± 0.003	−14.24	−14.55 ± 0.002
$\log(F_{[\mathrm{N\,II}]6584})$	−15.39	−15.39 ± 0.014	−15.35	−15.99 ± 0.042	−15.32	−15.24 ± 0.010	−15.35	−15.44 ± 0.009
$\log(F_{\mathrm{He\,II}6678})$	−17.95	−16.59 ± 0.198	−17.05	−16.71 ± 0.150	−17.11	−16.56 ± 0.078	−17.23	−16.62 ± 0.142

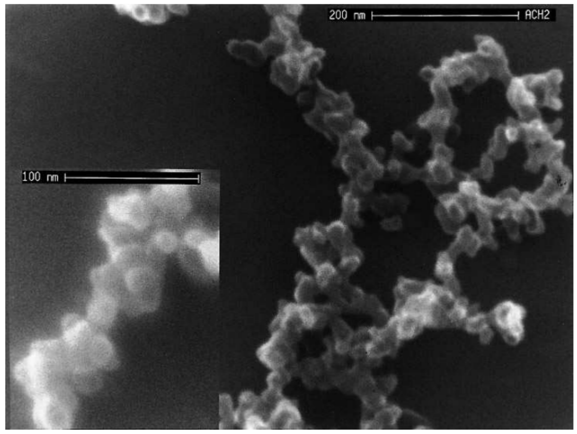

Figure 2.7: Scanning electron micrograph of carbon-rich dust particles (sample ACH2) exhibiting a fluffy, agglomerated morphology (Rotundi et al., 1998). This image provides visual evidence of the complex structures formed by these particles in interstellar medium.

Finally, we note that the most unknown parameter is the possible porosity of the dust grains. In fact, laboratory images of amorphous carbon particles show that these are chain-like agglomerates (see Fig. 2.7 taken from Rotundi et al., 1998). In the context of planetary nebulae, newly formed dust grains begin as very small particles (nanometer-sized), but as they collide, they can aggregate into larger and more complex structures. These grains can become porous, "fluffy," and irregularly shaped, particularly when the collisions are not entirely destructive but rather gentle. Thus, we also performed Cloudy simulations adopting fluffy grains, which simulate (to a certain degree) the porosity in the grains. Porosity accounts for internal voids and cavities that impact the interaction of dust with radiation and gas.

- Mass-Volume Relationship: A primary adjustment for porous grains is their mass-to-volume ratio, as porous grains have a lower effective density. This change affects the grain's opacity and thermal behavior because a grain with internal voids will have a larger cross-section for the same mass, influencing how it absorbs and scatters radiation.

- Optical Properties Adjustments: Porosity changes the effective refractive index of the dust grain, which affects scattering and absorption at different wavelengths. Models often use an "effective medium theory" to simulate this by treating the porous grain as a composite material (dust plus vacuum), which allows adjustment of its dielectric properties based on the porosity fraction.

- Radiation Interaction: Porous grains are less efficient in absorbing UV radiation but can scatter it more effectively. This distinction impacts the ionization balance in models and the thermal structure of the nebula, particularly in regions close to the ionizing star.

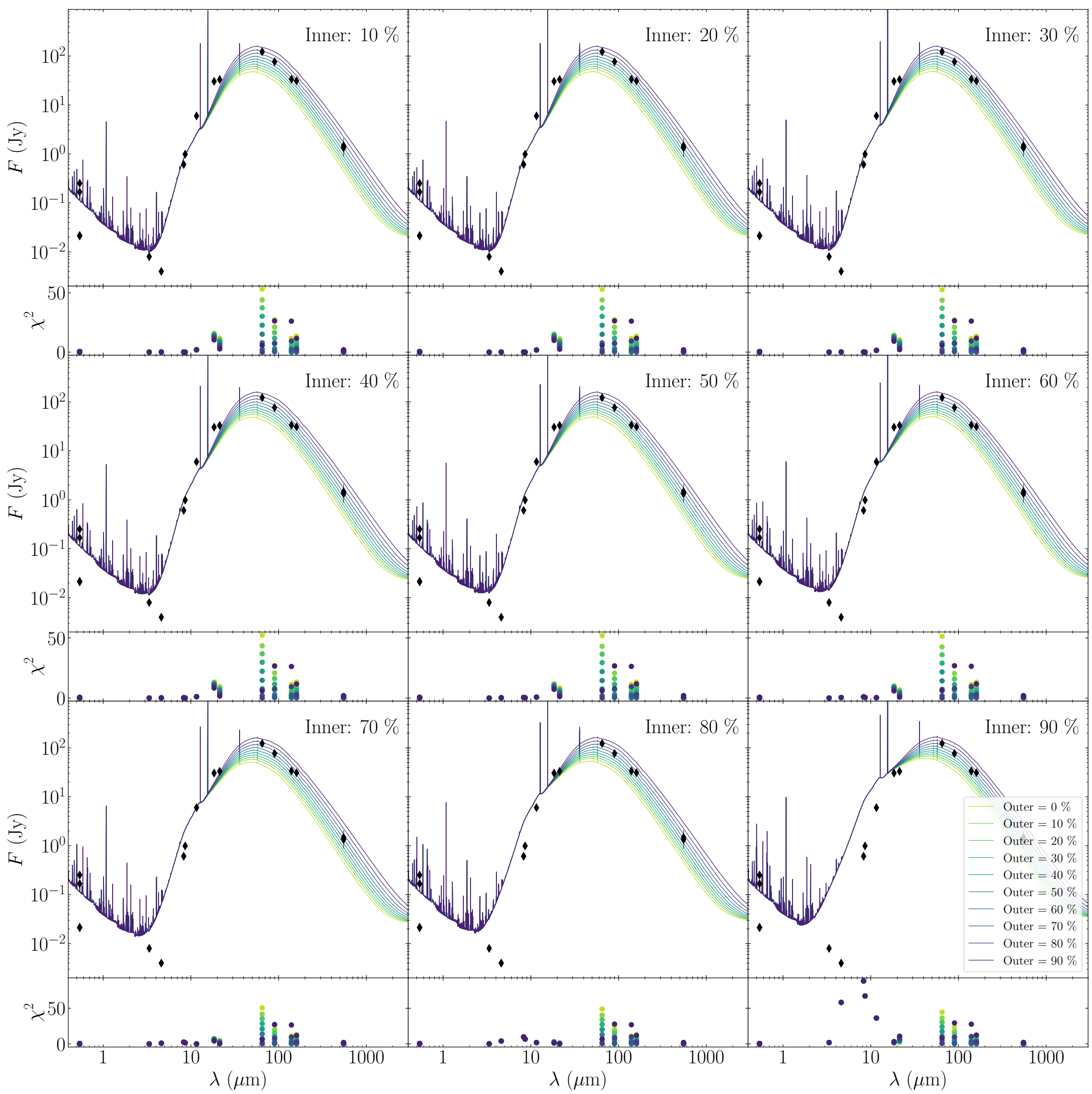

Figure 2.8: Family of Cloudy A 78 models adopting a range of porosity values for the dust grains. Each panel shows the result of adopting a fixed value for the porosity of the inner shell (from 10 to 90 per cent) with a combination of porosity values for the outer shell (same range).

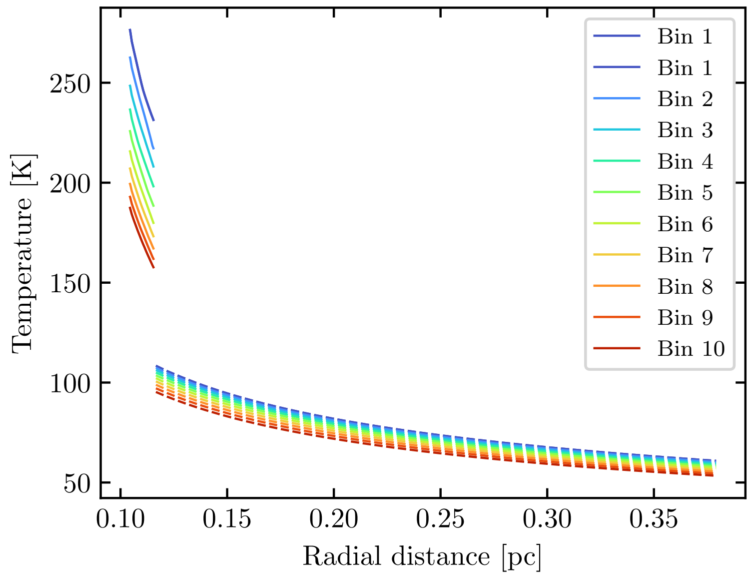

Figure 2.9: Temperatures profiles of the different dust grains sizes for our CLOUDY model of A 78. The dust in the inner shell is illustrated with solid lines, whist the large grains in the outer shell are presented with dashed lines.

In Cloudy, these porosity effects are often simulated by specifying parameters that adjust the dust's optical constants and its effective density. This allows for a more accurate representation of dust grains.

We ran a number of models combining different porosity values for the dust in the inner and outer shells. We adopted empty fractions between 10 and 90 per cent for both shells. Fig. 2.8 shows that large empty fractions for the dust in the inner shell increase the emissivity at near-IR wavelengths, deviating from the observed SED. This is a mere consequence that the effective area of each dust particle is increased at the cost of reducing the mass of the emitting dust. Thus, Fig. 2.8 suggest that the dust grains in the inner shell should be compact and solid. The effects of porosity on the dust grains in the outer shell affect the peak of the SED and values around 40 and 60 per cent empty fractions seem to produce similar χ^2 values. As a consequence of this analysis, we decided to favour a model with 10 per cent empty grains in the inner shell, but with grains with 50 per cent of emptiness in the outer shell.

Cloudy can also be used to consistently predict the dust temperature in our model. In Fig. 2.9 we present the temperature profiles of the dust population in our best model. This figure shows that the dust temperature ranges from 150 to 280 K for the inner shell and from $\sim$ 50 to 110 K for the outer shell. For comparison, Toalá et al. (2021) found that for A 30 the dust has almost the same temperature values ranging from 40 to 160 K.

Our best Cloudy model predicts the inner shell to have number density of n_1=1,300 cm^{-3}, a filling factor of $\epsilon_1 = 8 \times 10^{-6}$, and a dust-to-gas ratio of 0.05. The resultant gas and dust masses of this component are 2.6$\times$10^{-5} and 5.0$\times$10^{-7} M$_\odot$, respectively, for a total mass of the inner shell of 2.6$\times$10^{-5} M$_\odot$. In addition, the outer ellipsoidal shell resulted in number density, filling factor and dust-to-gas ratio of 80 cm^{-3}, 1$\times$10^{-4} and 21 respectively. Two of the output parameters we obtain are the total mass of the model:

$$M_{\rm TOT} = M_{\rm Gas} + M_{\rm Dust} \tag{2.3}$$

and the dust-to-gas ratio:

$$DG = \frac{M_{\rm Dust}}{M_{\rm Gas}} \tag{2.4}$$

From these, we can express:

$$M_{\rm Dust} = DG \times M_{\rm Gas} \tag{2.5}$$

Substituting Equation 2.4 into Equation 2.3, we have:

$$M_{\rm TOT} = (DG \times M_{\rm Gas}) + M_{\rm Gas} = M_{\rm Gas}(1 + DG) \tag{2.6}$$

From this we can solve for the individual masses:

$$M_{\rm Gas} = \frac{M_{\rm TOT}}{1 + DG} \tag{2.7}$$

$$M_{\rm Dust} = M_{\rm TOT} - M_{\rm Gas} \tag{2.8}$$

This calculation is performed for each shell, and the total mass is obtained by summing the gas and dust masses across all shells. The total mass of gas resulted in 2.8$\times$10^{-6} M$_\odot$ with 1.9$\times$10^{-5} M$_\odot$ of dust, for a total mass of the outer shell of 2.1$\times$10^{-5} M$_\odot$. We note that most of the gas is contained in the inner disk structure, whereas the dust mass of the outer ellipsoidal shell is $\approx$40 times that of the inner shell. The total masses for the H-deficient gas and dust in A 78 are estimated to be $M_{\rm gas}$=(2.9$\pm$0.4)$\times$10^{-5} M$_\odot$ and $M_{\rm dust}$=(1.9$\pm$0.2)$\times$10^{-5} M$_\odot$. If we assume that all the H-deficient material was produced during the VLTP event, then the total mass ejected during the VLTP would be the sum of the total gas and dust mass. We found that the VLTP mass is $(4.8 \pm 0.6) \times 10^{-5}$ M$_\odot$. If we assume that the born-again event lasted 20–100 yr (see Miller Bertolami et al., 2006), the mass-loss rate during the VLTP would be $\dot{M} = [0.48 - 2.40] \times 10^{-7}$.

2.4 Hubi 1

The near-IR images obtained with VLT VISIR show that the CSPN of HuBi 1 is still embedded in a cocoon of hot dust (see Fig. 2.1). Nevertheless, the spatial resolution of the VLT VISIR images is not sufficient to resolve any details of this structure, with a measured FWHM of 0.35 arcsec from a star in the field. Adopting the criterion presented by Santamaría et al. (2022) to determine the radius of an unresolved nebular shell as half the separation of two unresolved Gaussians, the cocoon of hot dust can be described in terms of the intrinsic FWHM of the source as

$$r = \frac{\mathrm{FWHM}}{2\sqrt{\ln 2}}.$$

This suggests $r \approx$0.21 arcsec for the IR-emitting cocoon of material in HuBi 1. That is, the location of the hot dust is well contained within the optically-emitting shell disclosed by the [N II] narrow band image. The later has apparent inner and outer radii of $\lesssim$1 and $\approx$2.25 arcsec, respectively. We suggest that the structure in HuBi 1 mainly traced by the [N II] emission was not detected by VLT VISIR observations because it is probably composed of colder dust.

These results seem to suggest that the VLTP ejecta might be currently distributed into two shells. An inner VLTP shell composed by hot dust located at distances below $\approx$0.21 arcsec from the CSPN and an outer VLTP shell with outer radius of $\approx$2.25 arcsec where colder dust should be present.

The *Spitzer* IRS spectrum of HuBi 1 exhibits the clear emission from the [Ne II] at 12.81 Å emission line (see the top panel of Fig. 2.10), which is very likely tracing the outer old PN. The spectrum peaks at $\lesssim$8 μm. However, we note that any strong conclusions drawn from the *Spitzer* data are questionable, given the fact that the slit did not covered the central areas of HuBi 1 (see the left panel of Fig. 2.2).

In order to achieve the best dust size distributions of the two VLTP shells we performed an interactive process. We noticed that a population of small dust sizes is required in the inner VLTP shell while a population of larger dust sizes is required in the outer VLTP shell. For the inner VLTP shell we require a population of porous amorphous carbon with sizes in the range of 0.0008–0.003 μm and a larger dust population with sizes 0.06–0.20 μm for the outer VLTP shell. Our best model is compared to the observed IR SED in the bottom panel of Fig. 2.10 and illustrates in (dark red) dashed and (light red) dotted lines the contribution from the inner and outer VLTP separately. This figure shows that the inner shell containing the population of small dust sizes dominates the emission for $\lambda < 10$ μm, whilst the population of large dust size is needed in order to fit the larger wavelength range.

If one tries changing the parameters of the density distribution (n and ϵ) to better tailor the fluxes of Hα and Hβ, we found a degeneracy. To illustrate the impact of varying these values, we particularly show in Fig. 2.11 the results for the inner shell, from which the degeneracy generates remarkable differences.

An important source of uncertainty in our models is the potential porosity of the dust grains. Laboratory studies of amorphous carbon particles have shown that they often form chain-like agglomerates (e.g., Rotundi et al., 1998), which suggests that dust grains in these environments may be porous. To account for this, we conducted additional Cloudy simulations incorporating fluffy grains to approximate the effects of porosity. A series of models was run, varying the porosity levels in both the inner and outer shells, with void fractions ranging from 10 to 90 percent in each shell. The models are calculated with the same dust mass. Fig. 2.11 shows that large empty fractions for the dust in the inner shell increase the emissivity at near-IR wavelengths, deviating from the observed SED. This is a mere consequence that the effective area

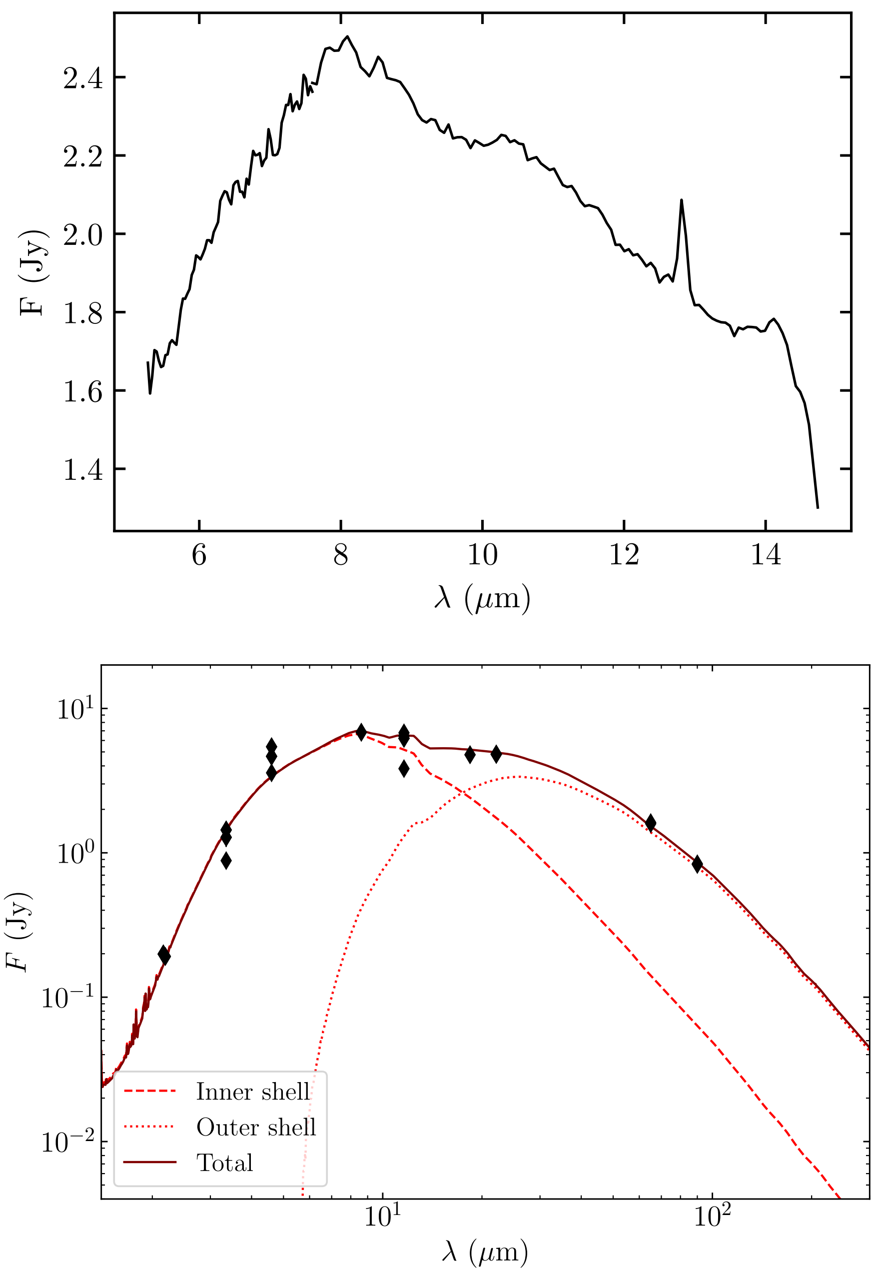

Figure 2.10: Top:*Spitzer* IRS spectroscopic observations of HuBi 1. Bottom: Observed IR SED of HuBi 1 (black diamonds). The best Cloudy model (solid line) along with the contribution from the inner and outer VLTP shells in dashed and dotted lines, respectively. This model adopted a 50 per cent porosity.

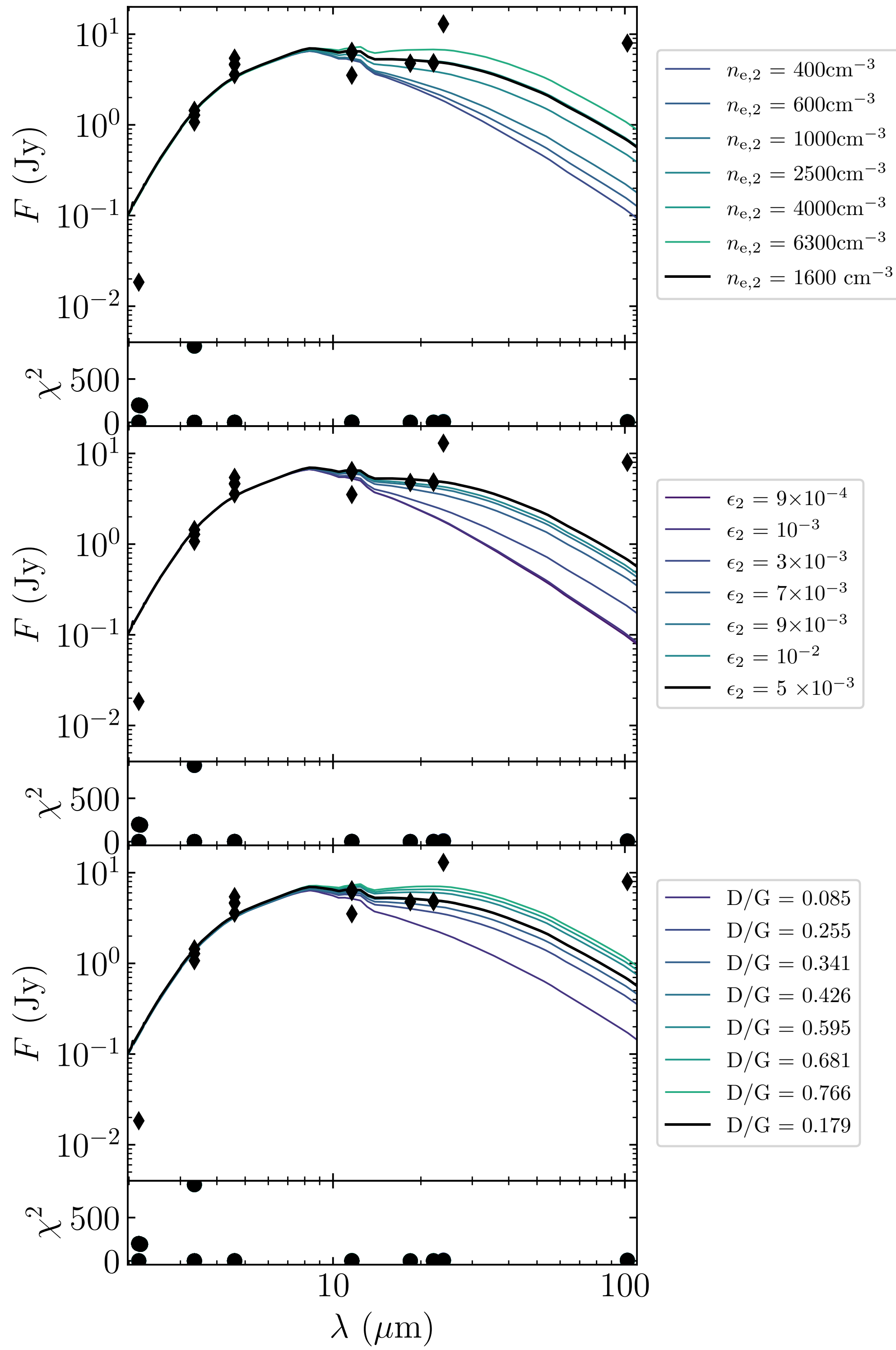

Figure 2.11: CLOUDY HuBi 1 models considering different values for the number density n (top), filling factor (middle) and D/G (bottom) for the outer shell.

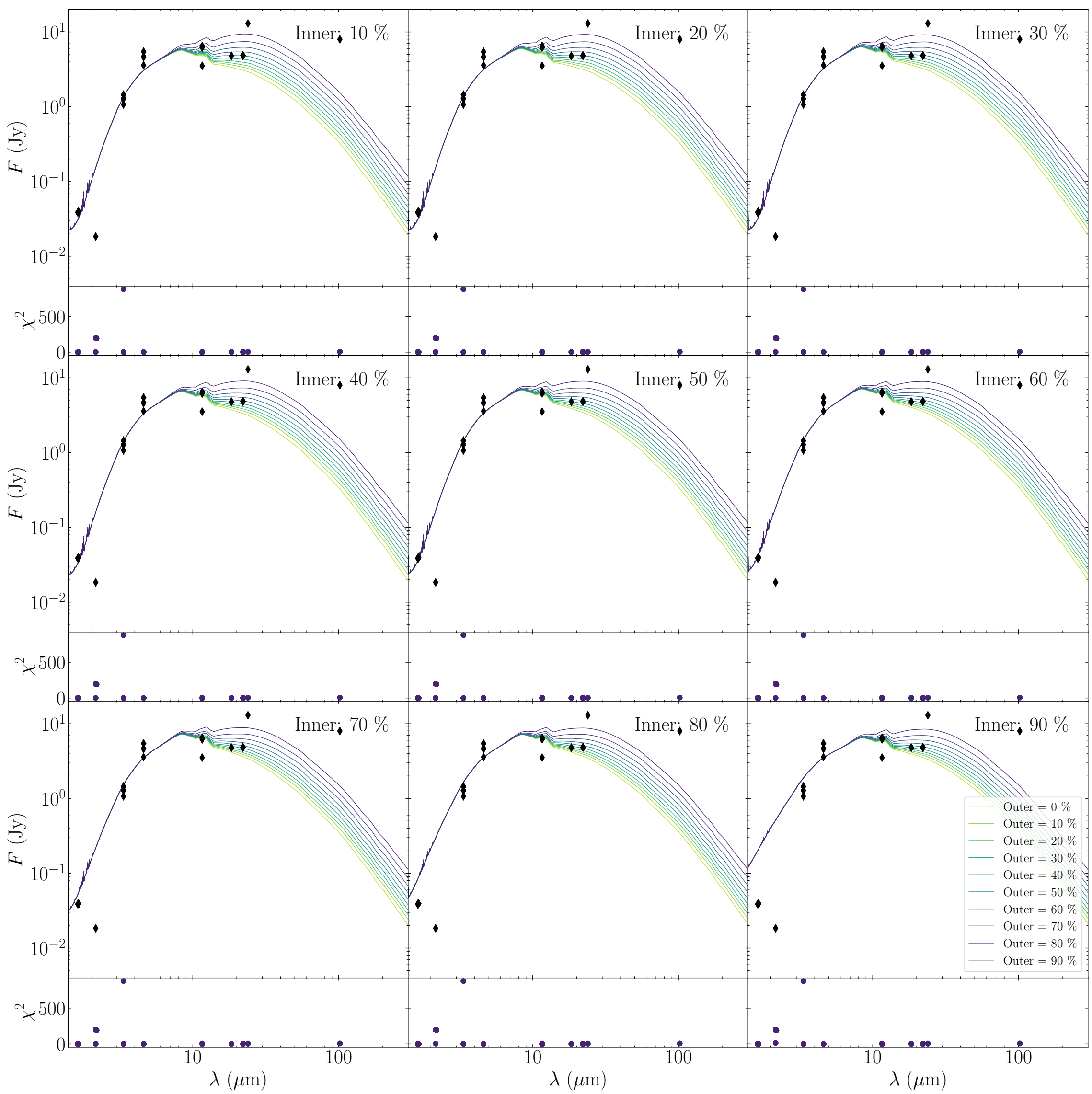

Figure 2.12: Family of Cloudy HuBi 1 models adopting a range of porosity values for the dust grains. Each panel shows the result of adopting a fixed value for the porosity of the inner shell (from 10 to 90 per cent) with a combination of porosity values for the outer shell (same range).

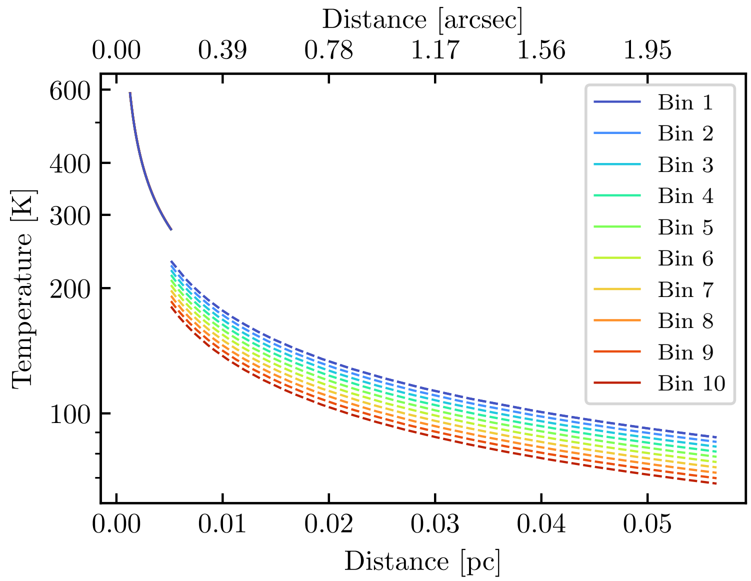

Figure 2.13: Temperature profiles of the different dust grain sizes for our best Cloudy model for HuBi 1. The dust in the inner VLTP shell is illustrated with solid lines, whist the large grains in the outer VLTP shell are presented with dashed lines. There are not apparent temperature differences between the different dust sizes in the inner VLTP shell.

of each dust particle is increased at the cost of reducing the mass of the emitting dust. Thus, Fig. 2.11 suggest that the dust grains in the inner shell should be compact and solid. The effects of porosity on the dust grains in the outer shell affect the peak of the SED and values around 40 and 60 per cent empty fractions seem to produce similar χ^2 values. As a consequence of this analysis, we decided to favour a model with 50 per cent empty grains in the inner and outer shell. Although Fig. 2.11 suggests that porosities of up to $\sim$70% cannot be ruled out, the optical line fluxes produced by these models fail to reproduce the lines reported by Montoro-Molina et al. (2023).

One of the physical parameters provided by Cloudy is the dust temperature distribution. The range of temperatures of all grain sizes in our best model is $\approx$80–600 K (see Fig. 2.13). The small grains, which are contain within the inner VLTP shell have temperatures above 290 K. There are not apparent temperature differences between different grain sizes in the small population. On the other hand, the large grains distributed in the outer VLTP shell have temperature values between 80 and 270 K. For comparison, Toalá et al. (2021) found that for A 30 the dust has smaller temperature values ranging about 40 and 160 K. We note that although the CSPN of A 30 is more than 3 times hotter than that of HuBi 1 (with a higher ionising photon flux), the dust-rich structures around it are two orders of magnitude more distant.

In Table 2.6 we list all the parameters of our best Cloudy model that includes 50 per cent porous C-rich dust. The model required the inner VLTP shell to have number density of n_1=1600 cm^{-3}, a filling factor of $\varepsilon_1 = 9 \times 10^{-3}$ with a dust-to-gas ratio of

0.562. The resultant gas and dust masses of the inner VLTP shell are 4.70×10^{-5} and 2.50×10^{-7} $M_{\odot}$. For a total mass of the inner VLTP shell of 4.72×10^{-5} $M_{\odot}$.

In addition, the outer VLTP shell resulted in number density, filling factor and dust-to-gas ratio of 160 cm^{-3}, 7×10^{-2} and 0.264, respectively. The total mass of gas resulted in 2.85×10^{-7} $M_{\odot}$ with 6.17×10^{-6} $M_{\odot}$ of dust mass. A total mass for the outer VLTP shell of 6.45×10^{-6} $M_{\odot}$. Consequently, the total masses of dust and gas are dominated by the inner VLTP shell. That is, our best Cloudy model adopting a 50 per cent of porosity predicts total masses of gas and dust for the VLTP ejecta in HuBi 1 of 4.70×10^{-5} and 8.70×10^{-6} $M_{\odot}$, respectively. We can estimate the mass of the VLTP ejecta as 5.57×10^{-5} $M_{\odot}$. If we assume that the born-again event lasted 20–100 yr (see Miller Bertolami et al., 2006), the mass-loss rate during the VLTP would be $\dot{M} = [0.56 - 2.79] \times 10^{-6}$ $M_{\odot}$.

2.5 Models implications

We obtained a satisfactory model that simultaneously fits the IR SED and makes an acceptable work by fitting the optical emission lines extracted from a similar observed slits as that used in Montoro-Molina et al. (2023) for A 78 and Montoro-Molina et al. (2022) for HuBi 1. Fig 2.5 and Fig 2.10 plots the total model and the contribution from each of the shells in comparison with the observations.

Following a similar approach to Toalá et al. (2021), the abundances of O and C can be determined, taking into account the contribution of dust. The general equations for estimating the total amount of O in the gas and the C/O mass ratio are as follows: The total mass of O in the gas can be expressed as:

$$M_{\rm gas,O} = X_{\rm O} \times M_{\rm gas,TOT}, \tag{2.9}$$

where $X_{\rm O}$ is the O mass fraction and $M_{\rm gas,TOT}$ is the total gas mass.
Similar for the mass of C :

$$M_{\rm gas,C} = X_{\rm C} \times M_{\rm gas,TOT}, \tag{2.10}$$

where $X_{\rm C}$ is the C mass fraction and $M_{\rm gas,TOT}$ is the total gas mass.
Assuming the dust is composed entirely of amorphous carbon, the C/O mass ratio can be calculated as:

$$\mathrm{C/O} = \frac{M_{\rm dust} + M_{\rm gas,C}}{M_{\rm gas,O}} \times \left(\frac{A_C}{A_O}\right), \tag{2.11}$$

where $M_{\rm dust}$ is the total mass of dust,A_C and A_O are the atomic weights of carbon and oxygen, with values of 12.011 and 15.999, respectively.
Applying this methodology to A78, and adopting the O mass fraction reported by Montoro-Molina et al. (2023), $X_{\rm O} = 0.05$, the total amount of O in the gas is estimated to be:

$$M_{\rm gas,O} = 0.05 \times M_{\rm gas,TOT}. \tag{2.12}$$

Since the C mass fraction of the gas has not been derived in previous works, the mass of C in the gas cannot be estimated.

Table 2.6: Details of our best Cloudy model for HuBi 1 adopting amorphous carbon with a porosity of 50 per cent.

Parameter	Model
Inner VLTP shell	
n_1	2,600
α	2
ε_1 ($\times 10^{-3}$)	7
$r_{\rm in}$ (arcsec)	0.05
$r_{\rm mid}$ (arcsec)	0.20
Amorphous carbon size distribution	0.0009–0.003
$M_{\rm gas}(\times 10^{-5} {\rm M}_{\odot})$	4.67
$M_{\rm dust}(\times 10^{-6} {\rm M}_{\odot})$	2.54
Dust-to-gas	0.054
Outer VLTP shell	
n_2	250
α	2
ε_2 ($\times 10^{-4}$)	8
$r_{\rm mid}$ (arcsec)	0.2
$r_{\rm out}$ (arcsec)	2.2
Amorphous carbon size distribution	0.09–0.40
$M_{\rm gas}(\times 10^{-7}$ ${\rm M}_{\odot})$	2.85
$M_{\rm dust}(\times 10^{-6}$ ${\rm M}_{\odot})$	6.17
Dust-to-gas	21.61
Total properties of the model	
$M_{\rm TOT,gas}(\times 10^{-5}$ ${\rm M}_{\odot})$	4.70
$M_{\rm TOT,dust}(\times 10^{-6}$ ${\rm M}_{\odot})$	8.70
$\log(F_{\rm H\alpha})$	-12.46
$\log(F_{\rm H\beta})$	-12.93
C/O	74.63 ± 0.4
Observed properties of HuBi 1	
$\log(F_{\rm H\alpha})$	-12.50
$\log(F_{\rm H\beta})$	-14.90

Considering that the dust in our model is exclusively amorphous carbon, we can assume that the mass of C in the dust is simply the total mass of dust $M_{\rm TOT,dust}$. Consequently, the mass ratio of C/O can be estimated to be

$$\mathrm{C/O} = \frac{M_{\rm dust}}{M_{\rm gas,O}} \times \left(\frac{A_C}{A_O}\right) \approx 17.72 \pm 0.08, \tag{2.13}$$

While for HuBi 1 we used the mass fraction abundances of O reported by Montoro-Molina et al. (2022), which is $X_{\rm O} = 0.39$, the contribution of O to the gas can be estimated as:

$$M_{\rm gas,O} = X_{\rm O} \times M_{\rm gas,TOT} = (1.83 \pm 0.2) \times 10^{-6}\mathrm{M}_{\odot}. \tag{2.14}$$

Consequently, the mass ratio of C/O can be estimated to be

$$\mathrm{C/O} = \frac{M_{\rm dust}}{M_{\rm gas,O}} \times \left(\frac{A_C}{A_O}\right) \approx 74.63 \pm 0.4 \tag{2.15}$$

This value, being greater than 1, strongly supports a VLTP event as the most probable formation scenario for HuBi 1 and A 78.

If it is assumed that most C produced during the VLTP has become dust, a lower limit close to the total C mass can be estimated. If we could estimate the contribution of C to the gas and include it in our calculations, the ratio will be even greater than this value. This strongly supports VLTP event as the most most probable formation scenario for A 78 and HuBi 1.

As mentioned in the previous section, our best model predicts that most of the mass in dust is concentrated within the outer shell of both models and that the smaller size dust particles are located in the inner structures. In A 78, this outer shell resides in the intermediate region between the inner disrupted disc and the outer old PN, which is H-rich. This is consistent with the predictions from Toalá et al. (2021) for A 30. There might be several factors that contribute to produce such configuration. First, radiation pressure on the grains will cause them to be accelerated pushing them away from the CSPN and the complex hydrodynamic processes occurring in the H-deficient clumps and filaments might drag the dust along with the gas depending on the coupling degree. On the other hand, the destruction of dust close to the CSPN might be also a considerable factor (Borkowski et al., 1994). Within 1000 yr after the born-again event in A 78 it is difficult to assess which effect has dominated over the other. However, our model requires the inner shell to host small dust grains, if we use larger dust populations in the inner shell would significantly alter the shape of the SED, making it difficult to reproduce shorter-wavelength photometry. The small population has almost no porosity, e.g., small and compact dust particles, these properties are strong indications of the intricate evolution of dust particles in the harsh environments of the CSPN of A78. This could be only explored by future radiation-hydrodynamic simulations that include dust physics and a detailed evolution of the stellar wind parameters and UV flux from stellar evolution models tailored to VLTP events.These future simulations will also help assessing the role of shocks in the ejecta of born-again PNe.

There have been other works that tried to model the IR properties of HuBi 1. In particular, Muthumariappan & Parthasarathy (2020) used multi-mission IR observations of PN hosting [WR]-type CSPN and estimated a dust colour temperature for HuB 1 of 99 K and a dust mass of $(4.3\pm1.9)\times10^{-4}$ $M_\odot$, an order of magnitude larger than the value estimated in this work. Differences in the mass estimated for HuBi 1 by Muthumariappan & Parthasarathy (2020) highlight several assumptions in our model that may lead to an underestimation of the dust mass. One significant factor is the incident spectrum: while Muthumariappan & Parthasarathy (2020) assume the star's emission to be a blackbody, we utilize a [WR] star model (PoWR), as illustrated in Figure 2.3, which shows a discrepancy between these two. The luminosity used in the photoionization model directly influences the amount of radiation that ionizes the surrounding medium. Underestimating the central star's luminosity (as would occur with a blackbody assumption) could result in reduced radiation production, consequently leading to a lower estimate of dust or gas mass. Additionally, the dust temperature they assume is lower than what we find in our Cloudy model; while they report a temperature of 99 K, we observe a dust temperature range from 65 to 600 K.

The robustness of our dust mass estimates lies in the detailed modeling approach implemented with Cloudy and the consistency between the modeled SED and observed photometric data. By integrating the dust and gas mass for each shell and comparing the results with observed optical and IR features, we validate the robustness of our approach, ensuring that the derived dust masses are physically plausible and consistent with the multi-wavelength data.

Thus far, there are few confirmed born-again PNe in the literature, and even worse, there are only two of these from which reliable masses have been estimated for their gas and dust content: A 30 and HuBi 1. A comparison between our results and those reported by Toalá et al. (2021) for A 30 is revealing. The estimated $M_{\rm VLTP}$ and $\dot{M}_{\rm VLTP}$ of HuBi 1 and A 78 are an order of magnitude smaller than those estimated for A 30. The latter suggests that although the physical properties of the material at the surface of the CSPN experiencing the VLTP must be similar, the amount of mass with such characteristics is not the same.

Chapter 3

Morpho-kinematic analyses of A 30 and A 78

In this chapter, we present a morpho-kinematic modeling approach using the SHAPE software to analyze the structural and kinematic properties of the born-again PNe A 30 and A 78. SHAPE is a powerful tool for constructing 3D models of nebulae based on observational data, allowing us to simulate and visualize the complex morphologies and velocity patterns within these nebulae. By fitting the observed emission lines and imaging data, we can assess the physical processes behind the shaping these born-again PNe. Our models provide new insights into the interactions between the stellar wind, the ejected material, and the pre-existing nebular structures in born-again PNe.

3.1 High-dispersion spectra

Long-slit high-dispersion optical spectra of A 30 and A 78 were obtained using the Manchester Echelle Spectrograph (MES) mounted on the 2.1 m telescope at the Observatorio Astronómico Nacional at San Pedro Mártir (OAN-SPM, Mexico). The data corresponding to A 30 were obtained on 2020 January 20 and 21, while those of A 78 were observed on 2023 July 25. Details of the observations are listed in Table 3.1.

We used the E2V 42-40 CCD with a pixel size of 13.5 μm pix^{-1} and a 4×4 on chip binning, which resulted in a plate scale of 0.702 arcsec pix^{-1}. A series of spectra were taken with exposures of 1200 s through the [O III] 5007 Å filter ($\Delta\lambda$=50 Å) to isolate the 114th order (0.086 Å pix^{-1} spectral scale). The slit width of 150 μm (1.9 arcsec) leads to a spectral resolution of 12 ± 1 km s^{-1}.

We observed five slits positions across the CSPN of A 30 and seven along that of A 78 with different position angles (PAs) to cover most of the H-deficient clumps and filaments surrounding their CSPN. The slit positions for A 30 an A 78 are illustrated in Fig. 3.1.

The spectra were processed using standard calibration routines in IRAF (Tody, 1993), including bias subtraction and wavelength calibration with ThAr arc lamps obtained immediately before and after the science observations. The wavelength accuracy is estimated to be $\pm$1 km s^{-1}.

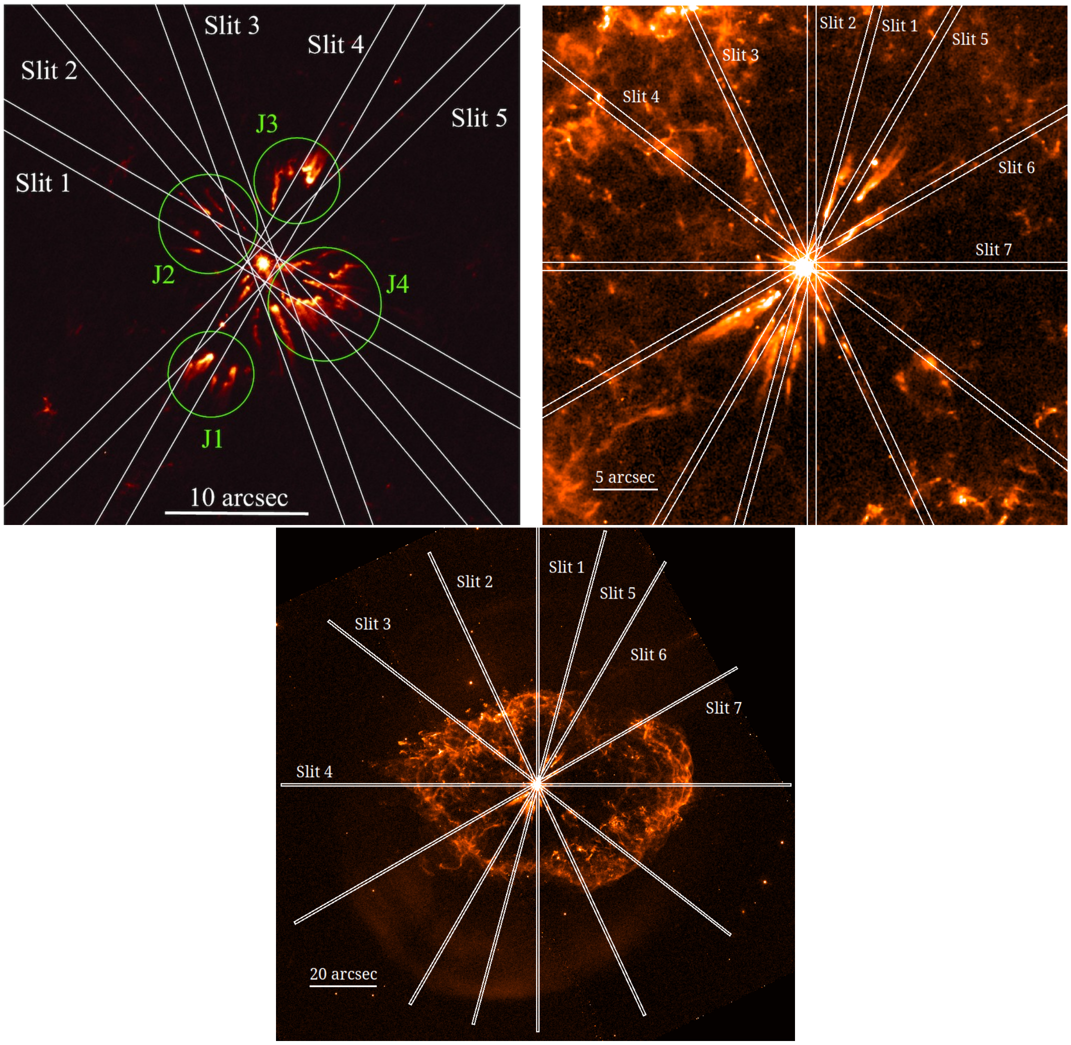

Figure 3.1: *HST* [O III] 5007 Å narrow-band images of A 30 (top left panel) and A 78 (top right and bottom panels). The position of the SPM MES slits are illustrated and labeled on each panel (see details in Table 3.1). In the three panels north is up and east is to the left. The top left panel presents green circles that delineate the previously unresolved clumps in A 30 defined as J1–J4 (see Reay et al., 1983).

Table 3.1: Details of the SPM MES observations of A 30 and A78. All spectra have exposure times of 1200 s and were taken with the [O III] λ5007 Å filter that isolates that emission line.

Object	Slit	PA ($^\circ$)	Date (yyyy mmm dd)	seeing ($''$)
A 30	1	60	2020 Jan 20	3.0
	2	40	2020 Jan 20	3.0
	3	20	2020 Jan 20	3.0
	4	−30	2020 Jan 21	2.0
	5	−45	2020 Jan 21	2.0
A 78	1	0	2023 Jul 25	2.0
	2	25	2023 Jul 25	2.0
	3	52	2023 Jul 25	2.0
	4	90	2023 Jul 25	2.0
	5	−15	2023 Jul 25	2.0
	6	−30	2023 Jul 25	2.0
	7	−60	2023 Jul 25	2.0

The complete set of position-velocity (PV) diagrams from A 30 and A 78 are presented in Fig. 3.2. We note that the selection of the slits in A 30 was designed to mainly trace the inner H-deficient clumps, whilst those of A 78 were distributed to simultaneously map as much as possible the inner H-deficient structure, the eye-like and the outer H-rich nebula. That is, for A 30 we will only construct a model of the disk-like and jet-like ejections, but we will be able to model A 78 in full. We would like to note here that the PV diagrams shown in Figure 3.2 resemble those presented in Meaburn & Lopez (1996) and Meaburn et al. (1998).**It is worth mentioning that Meaburn & Lopez (1996) and Meaburn et al. (1998) also used the SPM to obtain their spectra. However, our observations include a larger number of slits, allowing us to map a greater quantity of H-poor clumps and regions within the H-rich nebula, providing a more detailed kinematic and morphological characterization.**

3.2 Morpho-kinematic models

The software SHAPE was used to interpret the SPM MES [O III] spectra and optical images from *HST* WFC3 [O III] and NOT of A 30 and A 78, respectively. SHAPE allows the user to define different 3D geometric structures that can be edited (truncated, rotated and stretched) in order to produce forms that resemble those of the direct images of the studied objects. Moreover, expansion velocity laws can be defined for the different structures and subsequently, synthetic PV diagrams can be produced and compared to those observed. Our group has gained experienced using SHAPE in recent analysis of PNe, such as IPHASX J191104.8+060845 and NGC40 (see for example Rodríguez-González et al., 2021, 2022).

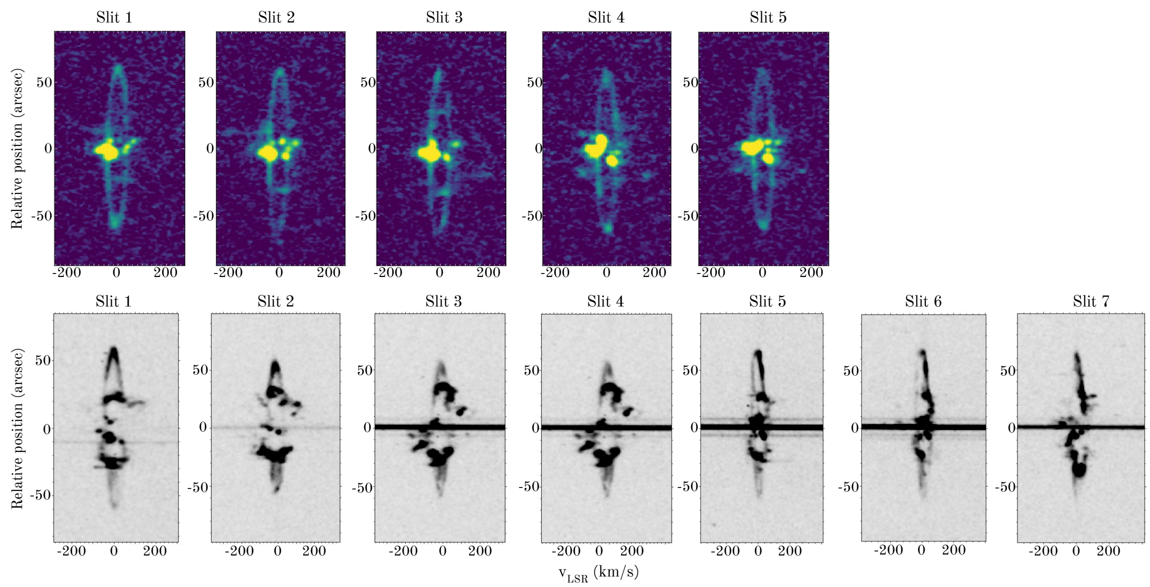

Figure 3.2: PV diagrams obtained from the SPM MES [O III] spectra of A 30 (top) and A 78 (bottom).

3.2.1 A 30

As a first attempt, we constructed a simple model of the central region of A 30. Previous observational works suggested that the inner H-deficient clumps of A 30 (and A 78) resemble a disrupted disk-like morphology with a pair of bipolar ejections (see Fang et al., 2014, and references therein). However, these suggestions have not been corroborated. Thus, we started with a simple toroidal structure and a pair of spherical clumps mimicking the jet-like features. Not surprisingly, those structures did not reproduce the images or PV diagrams obtained from observations of the H-deficient clumps and filaments in A 30. From this simple analysis we learned that the clumps and filaments in the so-called disrupted disk are not equidistant to the CSPN of A 30. In addition, the jet-like features seem to be composed by a collection of knots.

To improve the model, tailor-made structures were defined for each individual clump and filament. While images of A 30 suggest clumpy structures, the overall disrupted disk morphology can be reasonably approximated with *doughnut slice* in SHAPE. *doughnut slice* provide a generalized model for the clumps in the disrupted disk, capturing their primary shape, orientation, and density distribution while remaining compatible with the level of detail that SHAPE is optimized to handle. Due to the geometric limitations of SHAPE, which only allows us to use spheres, disks and cylinders, using truncated tori was the closest to simulating filaments. Those corresponding to the disrupted disk were assumed to be distributed mostly along the same plane, that will be referred as the equatorial plane. However, each of these structures required different widths in order to best fit the details in the observed

PV diagrams. The jet-like features were assumed to be located mostly along the orthogonal direction, i.e., the symmetry axis of the disrupted disk. The model further assumes that the symmetry axis of the disrupted disk and thus the jet-like features have a PA on the sky of $-30°$, the same used for slit 4 (see Table 3.1).

The shape of each individual structure and their velocities were then fine-tuned until the features in the synthetic [O III] image and PV diagrams were satisfactorily reproduced. Each truncated torus is defined by its distance to the star, thickness, length along the radial direction, and height over the equatorial plane. This process was iterative, requiring a comparison between the synthetic PVs and those obtained from observations each time a structure (and its properties is proposed).

The velocity at each point of these truncated tori is assumed to be radial and its modulus v is proportional to its radial distance r as

$$v(r) = v_0 \left(\frac{r}{r_0} \right), \tag{3.1}$$

where r_0 is the distance from the facing-side of the clump to the CSPN and v_0 is a characteristic velocity of each clump. This velocity law thus includes a velocity gradient within each clump that takes into account the head to tail velocity difference in a cometary knot.

The best SHAPE model of A 30 is presented in Figure 3.3 and the resultant synthetic PV diagrams are presented in the bottom panels of Figure 3.4 in comparison with those obtained from observations. As mention before, we only intend to model the inner H-deficient clumps in A 30. Edge- and pole-on projections of the best SHAPE model are also presented in the top-middle and top-right panels of Figure 3.3.

This model includes 20 more or less coplanar truncated tori around the CSPN illustrated in green in Figure 3.3, which form the disrupted disk. These structures are located on a plane with an average inclination angle i of $37° \pm 4°$ with respect to the line of sight, they have distances from the CSPN of A 30 ranging between 2.1 and 11.4 arcsec, with an averaged distance of 8.3 arcsec, and the average disk expansion velocity has a value $V_{\rm disk}$ of 105 ± 5 km s^{-1}, where the errors on i and $V_{\rm disk}$ are derived empirically solely based on the accuracy in reproducing the observed PVs and image by the model. The model requires the brightest SW optical knots to be slightly larger (see Fig. 3.3). Interestingly, the characteristic velocity of each clump v_0 decreases with their distance to the CSPN, in agreement with the results obtained by Fang et al. (2014) based on their proper motions. These structures fairly reproduce the morphology and kinematics of the disrupted disk[1] as illustrated in Figures 3.3 and 3.4.

Meanwhile, the jet-like features are reproduced using two groups of truncated tori, with the farthest ones along a direction orthogonal to that of the disrupted disk. These are located ∼24 arcsec from the CSPN and are illustrated in blue and red in Figure 3.3 for the approaching and receding structures, respectively. As the jets are assumed to be orthogonal to the disrupted disk, the best fit model implies a

[1]We note that this comparison is limited by the lower spatial resolution of the kinematic data compared to the superb *HST* image quality.

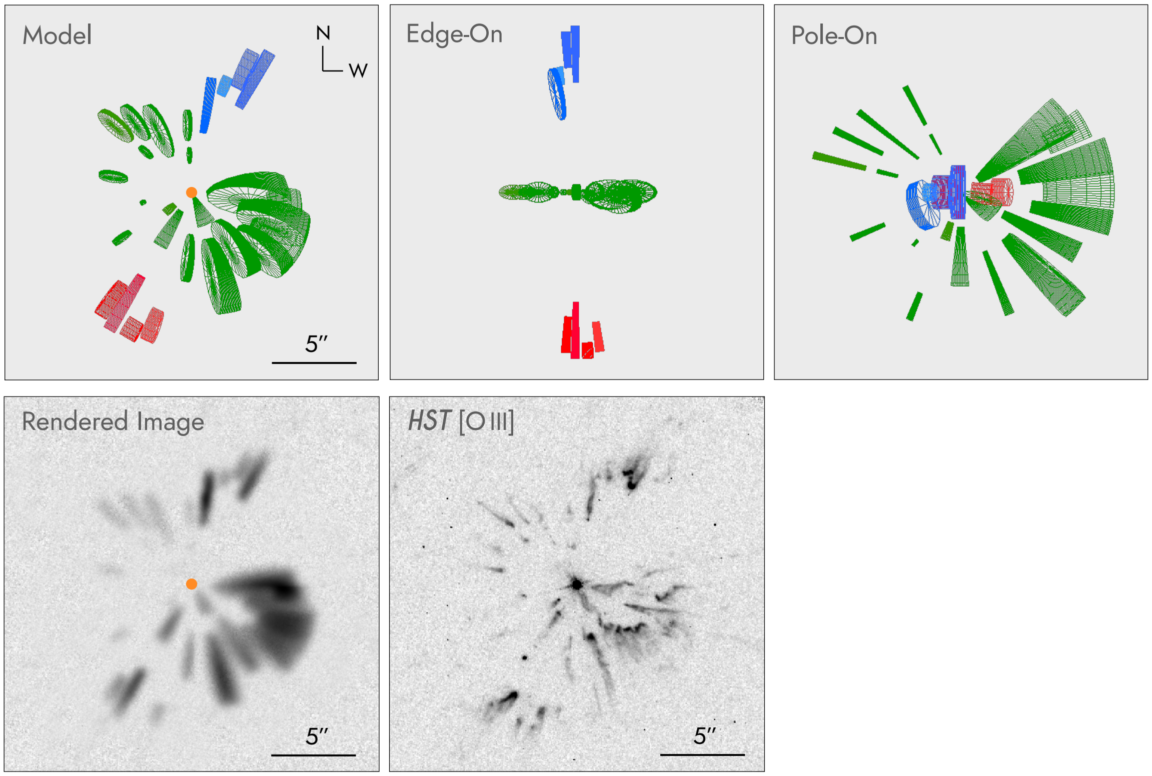

Figure 3.3: Morpho-kinematic model of A 30 obtained with the software SHAPE. Top panels show our best model through different viewing angles where features in green, blue, and red denote the disrupted disk and the approaching and receding jet-like structures in A 30, respectively (see Section 3.2 for details). The bottom left panel shows a rendered image which is compared with the *HST* [O III] image in the bottom right panel. The position of the CSPN is illustrated with an orange dot in the leftmost panels. The edge- and pole-on images do not have the same scale as the other panels, they are presented for illustrative purposes only.

deprojected expansion velocity for the jet clumps $V_{\rm jet}$ of 60 ± 5 km s^{-1} for the SE one and 45 ± 5 km s^{-1} for the NW one. The largest expansion velocity of the SE jet is also in agreement with its largest proper motion (Fang et al., 2014).

To further test our model, we also produced synthetic PV diagrams along long-slits similar to those presented by Chu et al. (1997). These were 1 arcsec wide and were oriented N-S at offsets 4 arcsec East and West of the CSPN of A 30, thus registering the SE and NW jet-like structures (knots J1 and J3), respectively, but also the eastern and western tips of the disrupted disk. The synthetic PV diagrams, shown in Figure 3.5, exhibit very similar spatio-kinematic patterns with those presented in figure 4 of Chu et al. (1997).

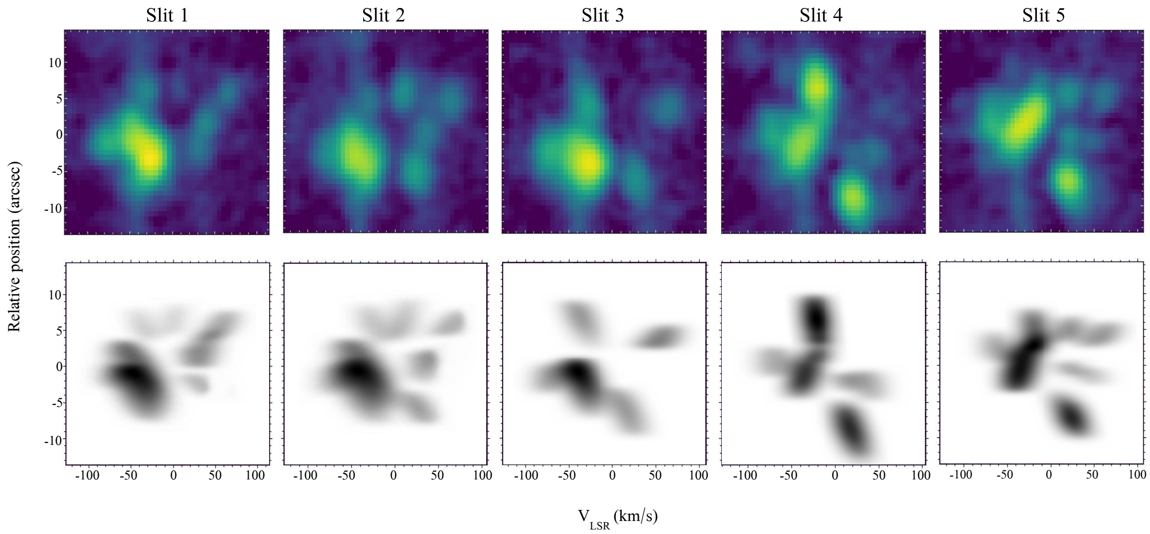

Figure 3.4: Top panels: PV diagrams obtained from the SPM MES [O III] spectra of the central region of A 30. Bottom panels: Synthetic PV diagrams obtained from our SHAPE model (see Sec. 3.2).

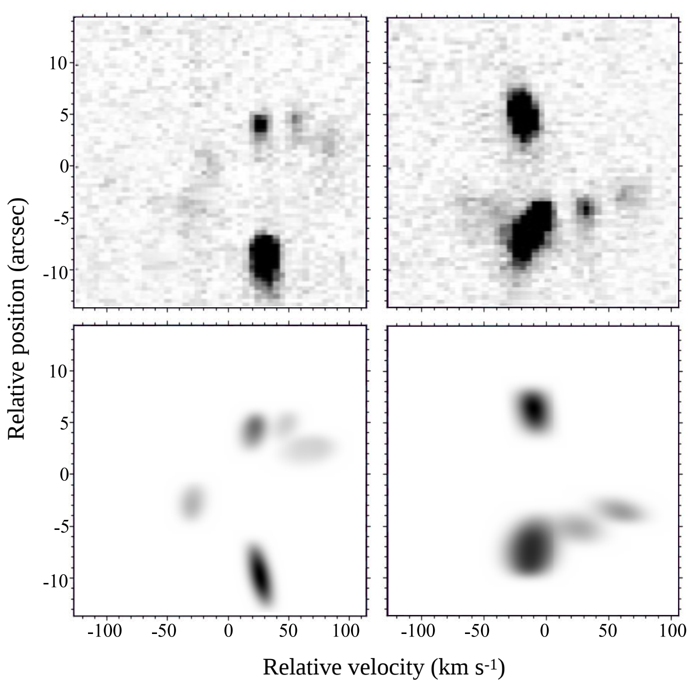

Figure 3.5: Top panels: High-dispersion [O III] spectra of A 30 presented in Chu et al. (1997) obtained at the 4 m Kitt Peak National Observatory. Bottom panels: Synthetic spectra obtained from our best SHAPE model of A 30. The spectra were obtained with a PA=0° in a N-S direction passing through the SE polar knot (left panels) and the NW polar knot (right panels).

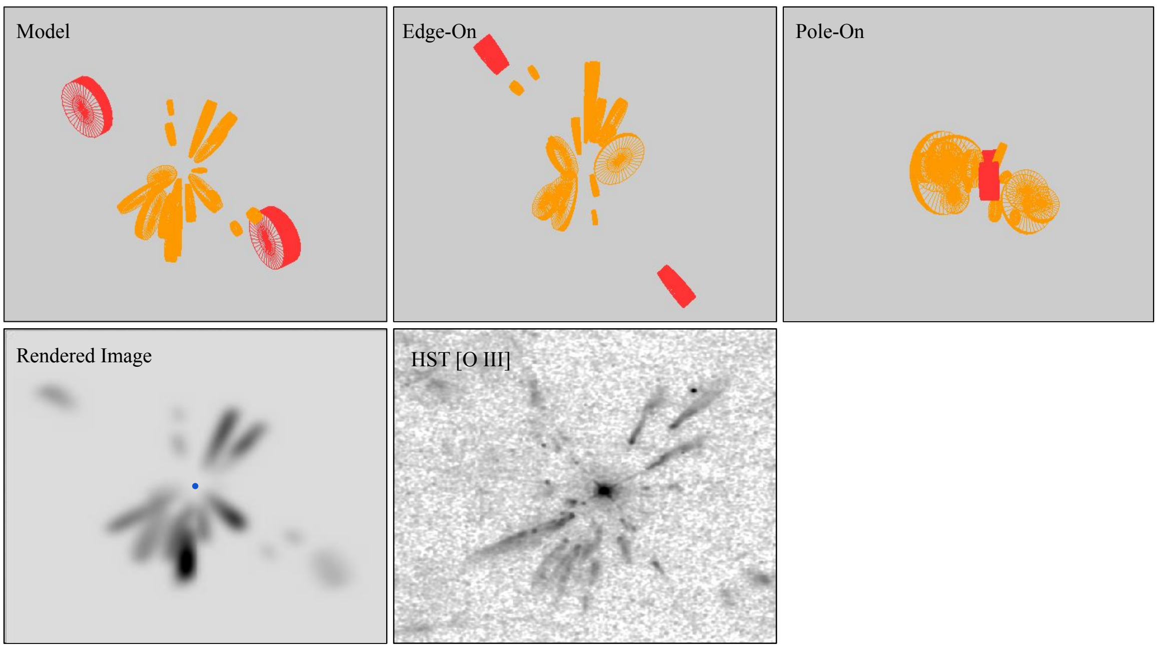

Figure 3.6: Morpho-kinematic model of A 78 obtained with the software SHAPE. Top panels show our best model through different viewing angles where features in orange and red denote the disrupted disk and the jet-like structures in A 78, respectively (see Section 3.2 for details). The bottom left panel shows a rendered image which is compared with the *HST* [O III] image in the bottom right panel. The position of the CSPN is illustrated with an blue dot in the leftmost panels.

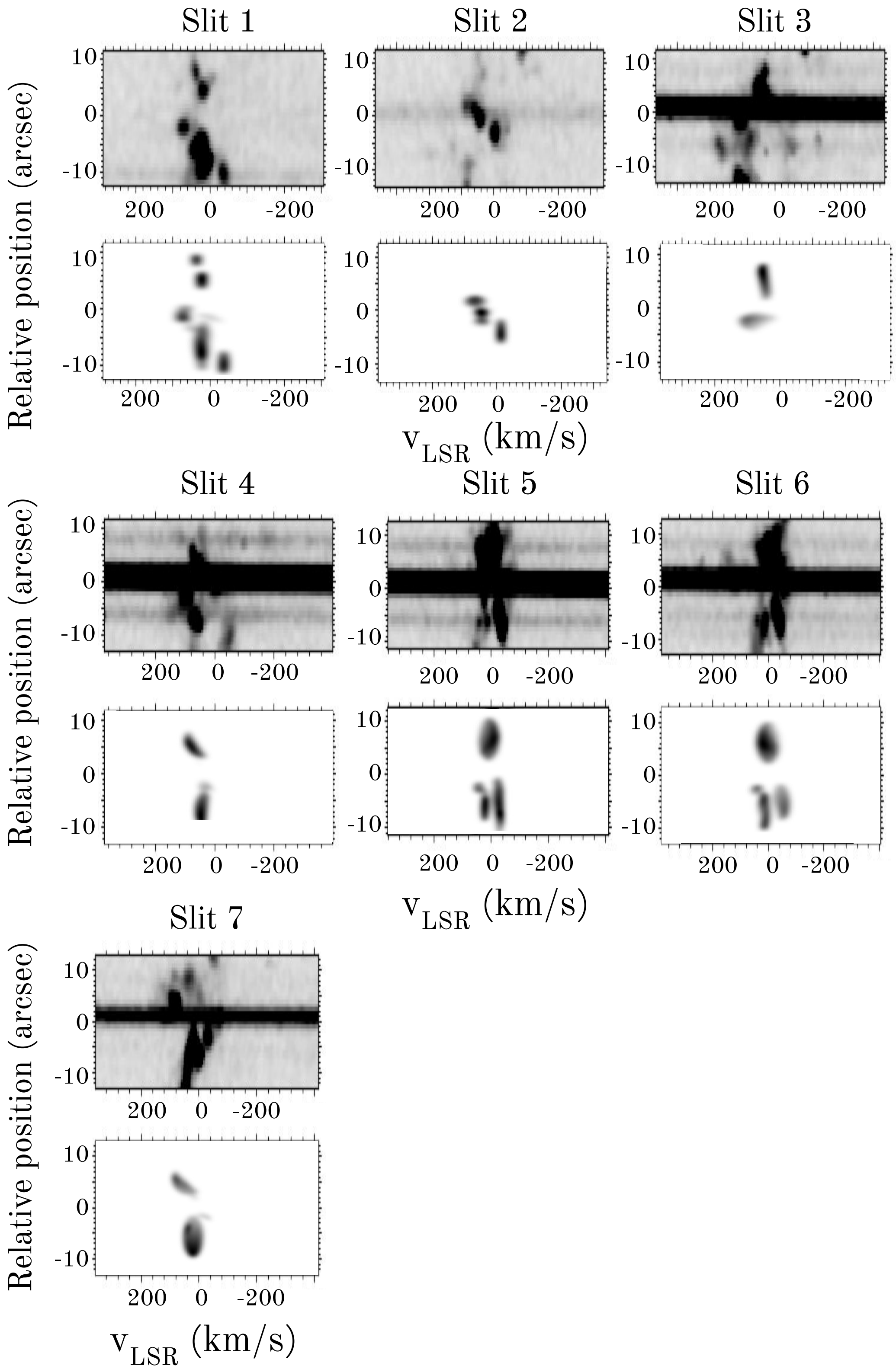

Figure 3.7: Top panels: PV diagrams obtained from the SPM MES [O III] spectra of the central region of A 78. Bottom panels: Synthetic PV diagrams obtained from our SHAPE model (see Sec. 3.2).

3.2.2 A 78

We followed the same procedure for the inner H-deficient clumps in A 78. The best SHAPE model of A 78 is presented in Figure 3.6 , with the resulting synthetic PV diagrams shown in the lower panels of Figure 3.7 in comparison with those observed. Additionally, edge-on and pole-on projections of the best SHAPE model are provided in the top-middle and top-right panels of Figure 3.6.

This model incorporates 27 truncated tori, arranged more or less coplanarly around the CSPN illustrated in orange in Figure 3.3. These structures are located more or less on a plane with an average inclination angle i of $80° \pm 4°$ with respect to the line of sight. They have distances from the CSPN of A 78 ranging between 2 and 14 arcsec, with an averaged distance of 8.6 arcsec, and the average disk expansion velocity has a value $V_{\rm disk}$ of 99 ± 3 km s^{-1}. Similarly to the case of A 30, the uncertainties associated with i and $V_{\rm disk}$ are empirically determined based solely on the model's ability to accurately reproduce observed PV diagrams and images. Again, similar to the case of A 30, the characteristic velocity v_0 of each clump decreases as its distance from the CSPN increases also consistent with the findings of Fang et al. (2014) based on their analysis of proper motions. These structures fairly reproduce the morphology and kinematics of the disrupted disk, as demonstrated in Figures 3.7 and 3.6.

The jet-like features are simulated using two truncated tori, positioned such that the farthest ones extend along a direction perpendicular to that of the disrupted disk. These components are located ∼24 arcsec from the CSPN and are illustrated in red in Figure 3.6. Given the assumption that the jets are orthogonal to the disrupted disk, the optimal model fit suggests a deprojected expansion velocity ($V_{\rm jet}$) for the jet clumps. Specifically, the SE jet exhibits a velocity of 100 ± 5 km/s, while the NW jet showcases a velocity of 160 ± 5 km/s.

The rest of the H-deficient clumps and filaments in A 78, the eye-like shape structure unveiled by the [O III] image presented in the bottom panel of Fig. 3.1, required a more complicated structural analysis. This required the ellipse shape illustrated with a blue mesh in Figure 3.8, with a semi-minor axis of 27 arcsec an a semi-major axis of 38 arcsec. With the objective to try to imitate the general elongated shapes in the eye-like structure we include some bumps or deformations. This process was iterative to try to reproduce as best as possible the PV diagrams (see Figure 3.9). To reproduce the observed spectra, the elliptical structure required an expansion velocity of 55 km s^{-1}.

Finally, the outer nebula was modeled with ellipse with a semi-minor axis of 55 arcsec and a semi-major axis of 60 arcsec. The ellipse required an inclination angle of $-30°$ with an expansion velocity of 50 km s^{-1}. It is illustrated in green in Figure 3.8.

3.3 Model implications

Within the model limitations, the morpho-kinematic SHAPE models in the previous sections do excellent jobs reproducing the observed PV diagrams and images of A 30

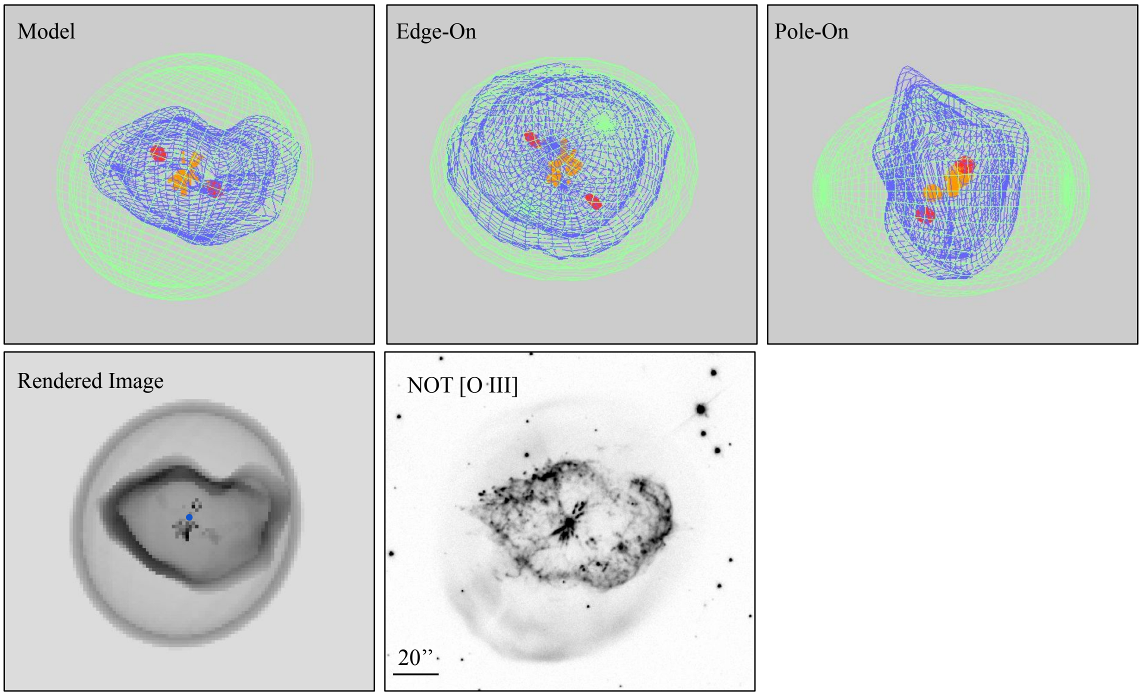

Figure 3.8: Morpho-kinematic model of A 78 obtained with the software SHAPE. Top panels show our best model through different viewing angles where features in blue and green denote the eye-like structure and the outer nebula in A 78, respectively (see Section 3.2 for details). The bottom left panel shows a rendered image which is compared with the *NOT* [O III] image in the bottom right panel. The position of the CSPN is illustrated with an blue dot in the leftmost panels.

and A 78. They confirm for the first time in these two born-again PNe that the H-deficient material close to their CSPN is distributed on disrupted disks and a pair of jet-like features.

In this section we will concentrate a discussion in the innermost structures of A 30 and A 78, the disrupted disks and jet-like structures. These structure offer us the best way to peep into the formation scenarios of these two born-again PNe. The complex morphology of the eye-like structure in A 78 likely resulted from intricate processes, such as those described by Fang et al. (2014), where multiple factors, including photoionization, momentum transfer, and interactions with the fast stellar wind, played significant roles in shaping the ejecta.

Contrary to what would be expected from the kinematics of a disk and a bipolar jet produced at the same time during a thermonuclear explosion, our SHAPE model indicates that the clumps in the disk-like structure in A 30 and A 78 expand faster than the jet features, while they are three times closer to the CSPN than those. These results are in line with those reported by Fang et al. (2014) who analyzed multi-epoch *HST* WFPC2 and WFC3 images and showed that the proper motions of the H-deficient clumps are higher for those closer to the CSPN. As mentioned before,

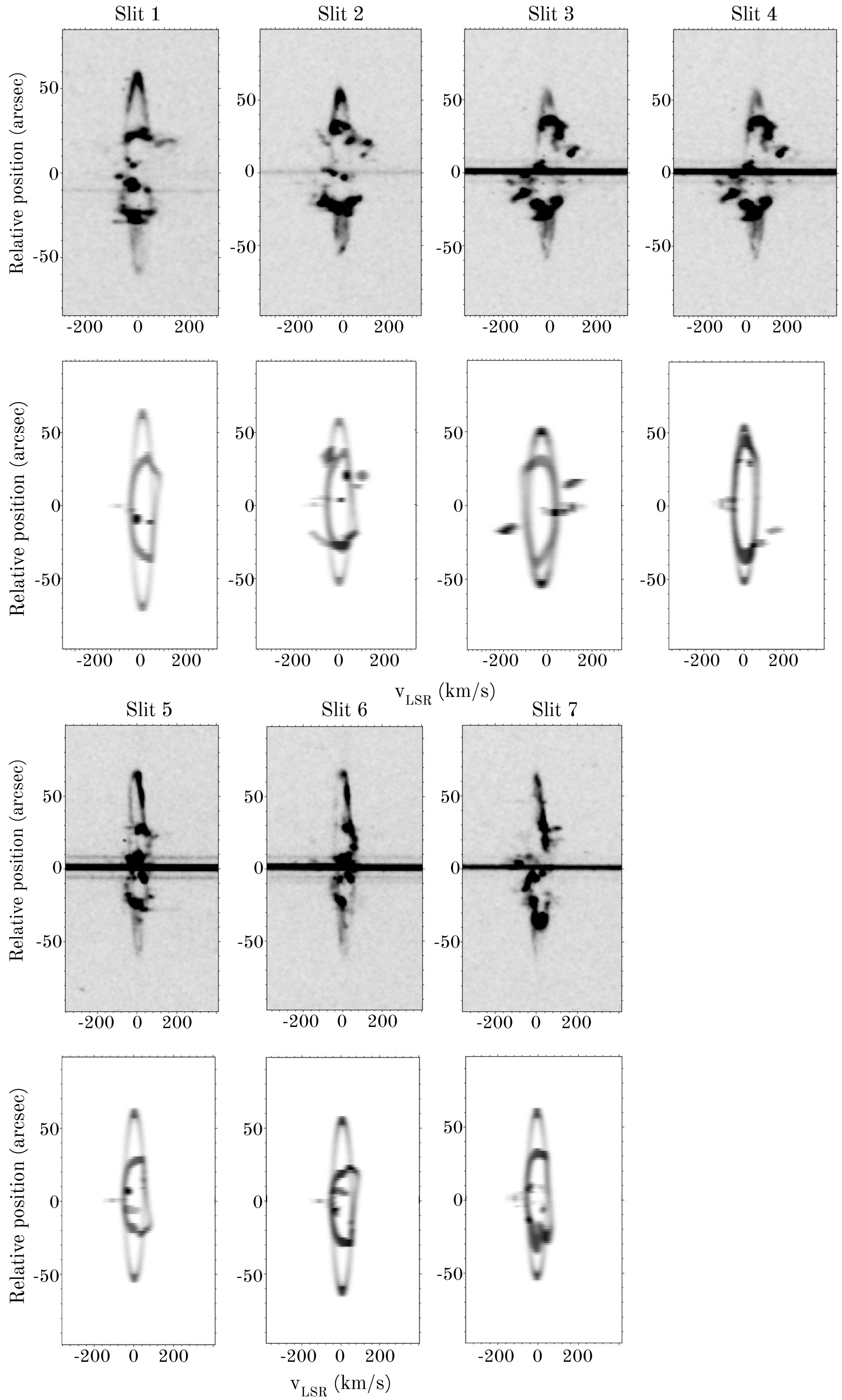

Figure 3.9: Top panels: PV diagrams obtained from the SPM MES [O III] spectra of A 78. Bottom panels: Synthetic PV diagrams obtained from our SHAPE model (see Sec. 3.2).

various physical mechanisms, such as photoionization, photoevaporation, the rocket effect and momentum transfer from the current fast wind to the dense clumps may have contributed altering the dynamics of the H-deficient ejecta and producing its complex morphology (see the discussion section in Fang et al., 2014).

The extreme bipolar morphology of the H-deficient clumps around the CSPN of A 30 and A 78 seem to concur with the possible presence of companions (Soker, 1997; Jacoby et al., 2020), which can be invoked to explain the modulation of the mass loss and the production of the disk+jet system. Nevertheless, the C/O ratio obtained after taking into account the C-rich dust in the ejecta in A 30 and A 78 suggests a single-star VLTP event (see Chapter 4 and Toalá et al., 2021). We propose that these apparently discrepant results can be simultaneously explained by invoking a VLTP followed by a common envelope (CE) evolution.

In the following, we describe our proposed formation scenario by describing the properties of A 30, but in a subsequent section we will compare with our results obtained for A 78. This scenario, illustrated in Figure 3.10, is detailed as follows:

a) The CSPN of A 30 evolved from a binary system comprising an evolved WD and a low-mass companion with masses M_1 and M_2, respectively (Fig. 3.10-*a*).

b) Following stellar evolution models, the WD experienced a VLTP causing the expansion of its outer layers and returning to the AGB locus of the HR diagram (see, e.g., Iben et al., 1983, Fig. 3.10-*b*). These predict a duration for the VLTP of decades to a few hundreds of years (see, e.g., Miller Bertolami et al., 2006, and references therein).

c) The radius increase of the primary caused the system to enter a CE phase (Fig. 3.10-*c*). The companion transferred angular momentum to the envelope, producing a reduction of its gravitational binding energy. CE numerical simulations predict that this process reduces the orbital separation within time scales of months-to-years (see, e.g., Chamandy et al., 2020). We refer to this stage as the CE-born-again (CEBA) phase.

d) Numerical simulations have shown that the companion (M_2) can help shaping the mass-loss from the primary (M_1) during the CE phase. This process might have produced a toroidal structure followed by a subsequent bipolar ejection of material (see, e.g., García-Segura et al., 2021; Zou et al., 2020; Lopez-Camara et al., 2021, and references therein). Thus, the shaping of the bipolar inner H-deficient clumps in A 30 took place during the duration of the VLTP. At this moment, the jet velocity $V_{\rm jet}$ was larger than the disk expansion velocity $V_{\rm disk}$ (Fig. 3.10-*d*). As the ejecta in the bipolar component moved faster than the disk, it was located at larger distances from the CSPN than the toroidal structure. This phase will be referred as early born-again (EBA) phase.

e) A large amount of works on born-again PNe suggests that the evolution of their CSPN is fast after experiencing a VLTP (see Evans et al., 2020; Hinkle et al., 2020, and references therein). The star shrinks and gets hotter so

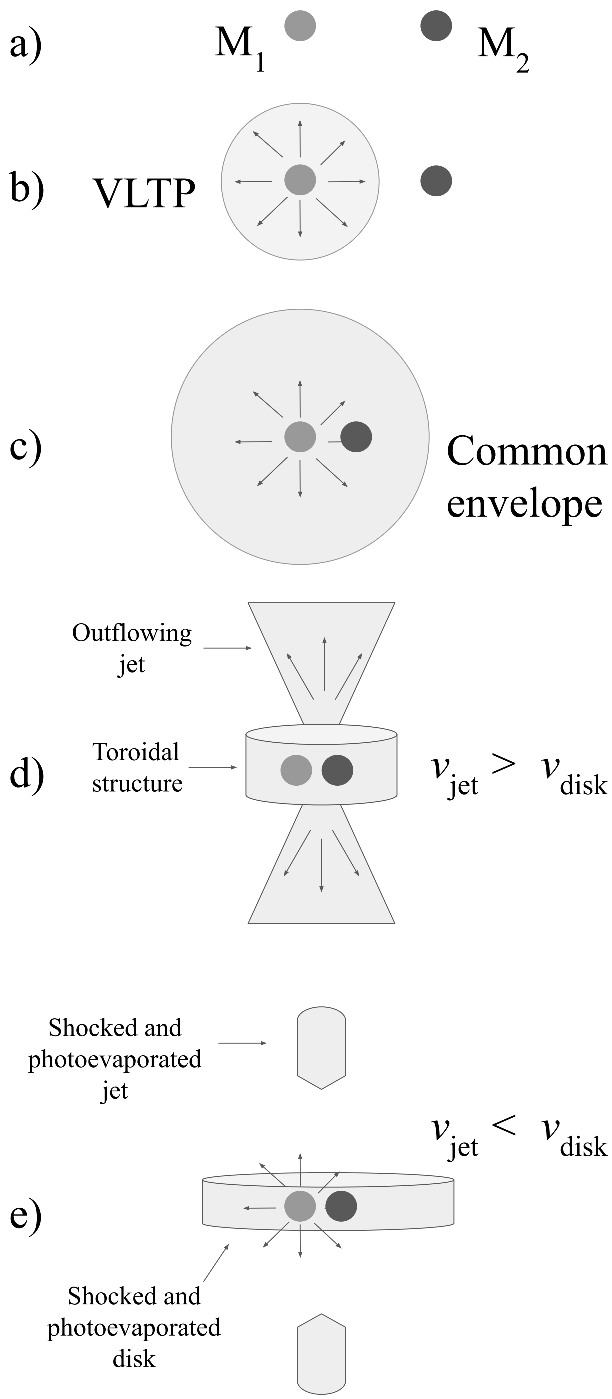

Figure 3.10: Cartoon of the evolutionary path of the H-deficient ejecta in A 30. This figure describes the CEBA scenario proposed in this work, in which a WD experiences a VLTP and the ejection of material is shaped into a bipolar morphology by a companion entering a CE phase. After the VLTP, the new WD develops a strong wind and ionizing photon flux that imprints momentum onto the H-deficient material. The closest structure is then accelerated faster than the bipolar structures. See Sec. 3.3 for details.

that a fast stellar wind and strong UV flux are developed. We propose that after the EBA phase, the increased stellar wind momentum and ionizing flux induced the toroidal structure to experience hydrodynamical instabilities that ultimately disrupted it into clumps and filaments within a few hundred years (see the radiation-hydrodynamic simulations presented in Fang et al., 2014). The momentum transfer efficiency from the wind to the H-deficient material would be larger for closer structures. In particular, the CSPN of A 30, which experienced its VLTP about $\lesssim$ 900 yr ago, has a current stellar wind with a terminal velocity of $\approx$4000 km s^{-1} and an effective temperature of $T_{\rm eff}$ $\sim$115 kK (Guerrero et al., 2012). Accordingly, the clumps in the disk that were closer to the CSPN were accelerated faster than the bipolar structures, ultimately producing the current kinematic configuration where the jet velocity $V_{\rm jet}$ is smaller than the disk expansion velocity $V_{\rm disk}$ (Fig. 3.10-e). We will refer to this stage as late born-again (LBA) phase and propose that A 30 can be actually placed into this evolutionary stage.

The proposed scenario can also help explaining the fact that the larger and brighter clumps and filaments in the disrupted disk of A 30 have a preferential distribution towards the SW of the CSPN. Simulations have shown that the toroidal structure formed as the result of a CE evolution is uneven and inhomogeneous (see, for example, Figure 1 in Ondratschek et al., 2022, and their associated videos). Density enhancements appear and get diluted towards the equator of the toroidal structure in short time-scales and are not symmetric given the orbital motion of the companion star. Thus, it is very likely that by the time the fast wind and the UV flux of the CSPN of A 30 increased, a density enhancement existed towards the SW.

In the proposed CEBA evolution scenario (see Fig. 3.10), the disk and jet abundances would be the same and thus we suggest that the differences in their ADFs reported by Simpson et al. (2022) should be rather attributed to their different physical properties. These would produce variations in the extent of the temperature (Peimbert, 1967) and density fluctuations (Viegas & Clegg, 1994), or in the clumping of the H-deficient material (Liu et al., 2000), which have long been suggested to cause the ADF (see, e.g., Wesson et al., 2018, and references therein). The IR study of A 30 presented by Toalá et al. (2021) indeed points to different physical properties between the disk and jets, with dust at temperatures of $\lesssim$200 K mainly present in the disrupted disk of A 30. Alternatively, the interaction of the companion with the expanded star envelope during the CEBA and EBA phases, which would feed the disk with processed material, may result in chemical abundances different for the jet and disk. As concluded by Simpson et al. (2022), it is critical to assess the specific mass fraction of H-poor and H-rich material of the different components of the ejecta to further peer into this discrepancy.

A detailed 2D mapping of the chemical abundances for each clump in A 30 (and other born-again PNe) would resolve this issue. Our group has recently adquired high-dispersion integral field spectroscopic data of A 30, A 58 and A 78 that are currently being analyzed (see Chapter 5). In addition, radiation-hydrodynamic numerical simulations following in detail the stellar evolution of stars experiencing a VLTP will be used in the future to test our proposed CEBA scenario and to assess the time scales on the formation of the complex structures in born-again PNe.

3.3.1 Comparison with other born-again PNe

The proposed CEBA scenario can be used to describe the characteristics of other born-again PNe. If we consider that the nebulae A78, A30, A58, HuBi 1, and Sakurai's object experienced the VLTP under similar conditions, we could establish a timeline with these nebulae in our scenario, as shown in Fig. 3.11. In particular, we note that A 78 shares many similarities with A 30. The morphology of the dense H-deficient clumps in A 78 also resemble a disrupted disk+jet system and their expansion parallaxes and radial velocity patterns are very similar to those of A 30 (e.g., Meaburn et al., 1998), as well as their kinematic ages, $\lesssim 10^3$ yr (Fang et al., 2014). In addition, their CSPNe exhibit almost the same properties (see Toalá et al., 2015). Thus, it can be envisaged that the CEBA scenario proposed for A 30 would also explain the properties of A 78.

The born-again PN A 58, which experienced its VLTP in 1919, about 100 yr ago, also displays a bipolar ejection with a dense toroidal structure almost obscuring its CSPN (Hinkle et al., 2008). The expansion velocity of the optical ejecta has been shown to be $\sim$200 km s^{-1} (Clayton et al., 2013), but recent ALMA observations of the molecular component of A 58 demonstrated that the toroidal structure expands with a velocity of 90 km s^{-1} from the CSPN whilst the bipolar emission has a faster velocity of 280 km s^{-1} (Tafoya et al., 2022). Interestingly, these authors found that the molecular material in the bipolar ejection can be traced closely to the CSPN and has a kinematic age of $\lesssim$20 yr, i.e., apparently younger than the VLTP event. The effects of the fast stellar wind and strong UV flux from the CSPN of A 58 are not yet dominant as in A 30 and A 78. Thus, under our proposed scenario, A 58 can be placed in the EBA phase of the evolution of a VLTP ejecta (Fig. 3.10-*d*).

The youngest born-again PN, the Sakurai's Object, experienced its VLTP event in February 1996, a bit less than 30 yr ago. Only two years later, in March 1998, material expanding at velocities up to -550 km s^{-1} was revealed by a blue-shifted absorption line of He I 10830 (Eyres et al., 1999). Soon afterwards, optical observations obtained on 2001 detected a bipolar outflow in the [N II] emission lines with two components at systemic velocities of -350 ± 50 and $+200 \pm 50$ km s^{-1} (Kerber et al., 2002), thus implying an average velocity close to the 290 km s^{-1} derived from the fundamental vibration–rotation CO band lines around 4.7 μm detected by Eyres et al. (2004) in 2003. This expansion velocity seems to have remained unchanged in the last decade (Hinkle & Joyce, 2014; Hinkle et al., 2020). Subsequent modelling of the IR emission led Chesneau et al. (2009) to suggest the presence of a disk-like structure seen almost edge on, obscuring the progenitor star. Interestingly, the expansion velocity of the densest molecular material probed by the sub-mm detection of the HCN molecule is $\gtrsim$100 km s^{-1} (Tafoya et al., 2017). If we assume that the densest molecular material is associated with the toroidal structure, its expansion velocity would be several times smaller than that of the bipolar outflow. This would place Sakurai's Object in the EBA phase, where the bipolar ejection is still faster than the disk-like structure. Our

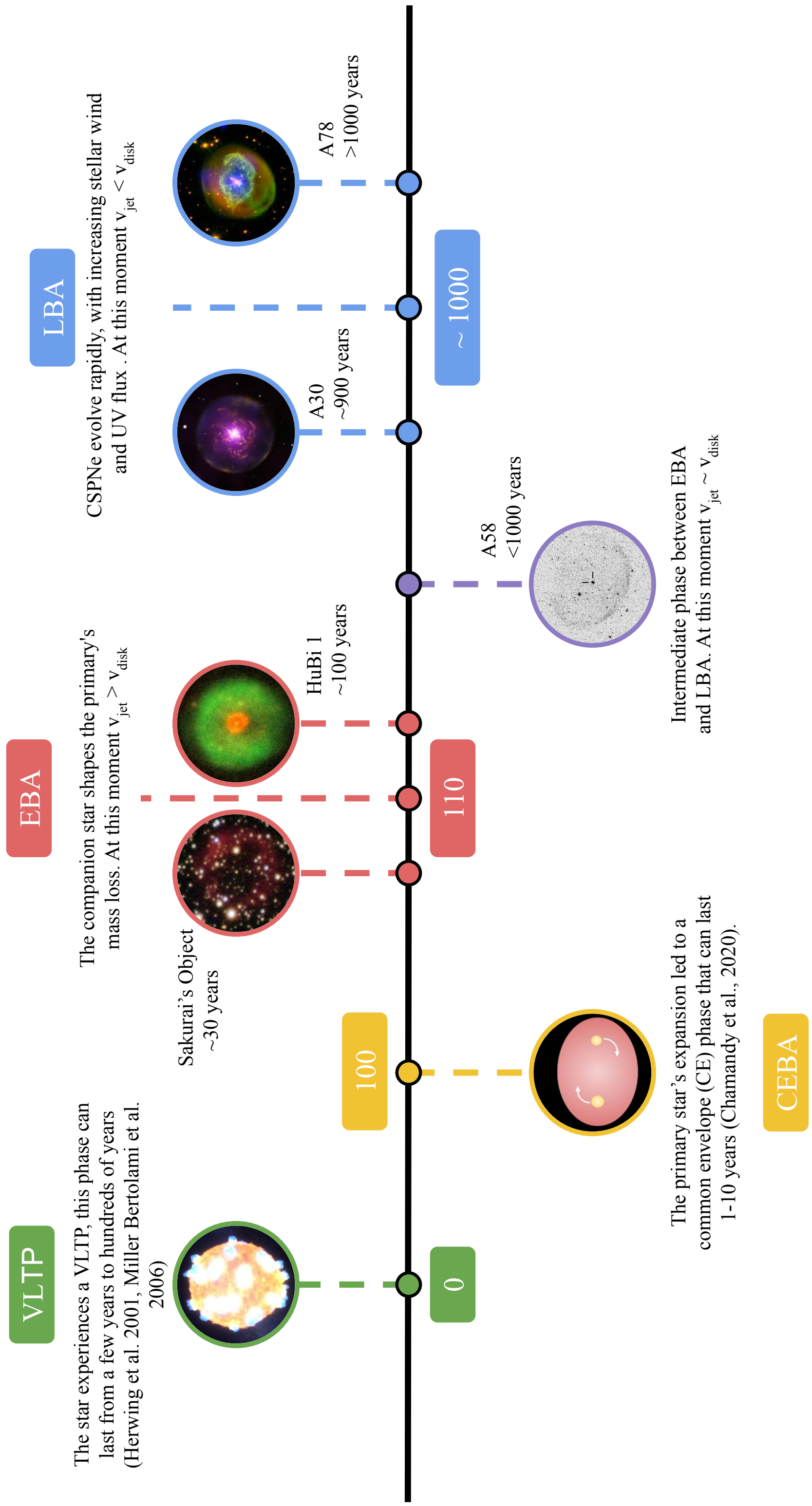

Figure 3.11: Illustration of the CEBA scenario shown in Fig. 3.10, showing key evolutionary stages and estimated timescales for BA PNe following a CE and a VLTP. The timeline includes likely positions of born-again PNe A30, A78, A58, HuBi 1 and Sakurai's Object, based on their estimated VLTP ages.

team has gathered ALMA data to map the molecular and continuum emission of Sakurai's Object to probe the extreme bipolar morphology of this born-again PN (Tafoya et al., 2022).

The last addition to the born-again PN class is HuBi 1 (Guerrero et al., 2018; Montoro-Molina et al., 2022). The 2D morpho-kinematic properties of its H-poor ejecta have been interpreted as a prolate ellipsoidal shell (Rechy-García et al., 2020b), although the extremely bright emission around the systemic velocity and weakness of the fastest components suggests an alternative physical model consistent of a bright equatorial disk mostly on the plane of the sky and a bipolar outflow tilted with the line of sight. The similarity between the expansion velocity of the disk on the plane of the sky[2] of 290 km s^{-1} and that of the bipolar outflows of 250 km s^{-1} (Rechy-García et al., 2020b) suggests that HuBi 1 would be in the transition between the EBA and LBA phases. Indeed HuBi 1 experienced its VLTP about 200 yrs ago (Rechy-García et al., 2020b) and thus it has an intermediate age between A 58 and the more evolved A 30 and A 78.

3.3.2 Model caveats

The proposed morpho-kinematic models in addition to the CEBA scenario provide a reasonable description of the morphology and spatio-kinematics of A 30 and A 78, as well as their formation and evolution. Still we would like to mention a few caveats.

The generally spherical shape of the older nebulae in most born-again PNe poses a concern in understanding their formation, particularly if binary interactions are involved. Typically, binary-induced shaping produces asymmetry, yet the halos of many born-again PNe remain round or slightly elliptical, without clear traces of binary influence.

In binary interactions, the shaping of the nebula is often influenced by the balance between angular momentum transfer and mass ejection dynamics. For a relatively spherical shape, simulations suggest that the CE phase must occur with either a slow ejection velocity or a more isotropic outflow. This can happen if the envelope ejection is partially supported by a low-mass companion or if the CE phase is incomplete, allowing part of the material to settle back symmetrically around the system (Ivanova et al., 2013; Ricker & Taam, 2012).

This setup has implications for the orbital separation, as a slow, spherically ejected envelope allows more of the companion's angular momentum to be transferred to the primary's expanding envelope, gradually shrinking the orbit. This reduced orbital distance can bring the stars close enough that, if a VLTP occurs, the system may enter a CE phase afterward.

The CEBA scenario presents significant challenges, especially with regard to a VLTP followed by a CE phase. Assuming a VLTP causes the star to contract into a hotter, more compact configuration after it leaves the AGB phase, decreasing its likelihood of entering a CE phase. During the AGB phase, the star reaches its maximum radial expansion, making it more susceptible to CE interaction. Therefore,

[2] We note that this value depends on the rather uncertain distance to HuBi 1.

if the system avoided CE during the AGB, it's challenging to explain how a much more compact post-AGB star could later trigger a CE phase. For this scenario to be plausible, the binary separation would need to decrease significantly during the post-AGB phase. However, mechanisms such as the Kozai-Lidov effect, where a tertiary companion perturbs the binary orbit, could gradually shrink the orbit over time, potentially enabling CE post-VLTP (Thompson, 2011). Alternatively, stellar winds could induce some orbital decay in specific scenarios (Moe & Di Stefano, 2017), though this requires tuning of initial conditions to effectively induce CE interaction at the post-VLTP phase.

Another critical issue is statistical. If VLTP events were limited mainly to binary systems, it would imply that a high proportion of VLTP stars are in binaries close enough to interact, despite VLTP events being driven by internal processes rather than binarity. With only about 25% of low-mass stars in binaries close enough to interact, it's statistically unlikely for all VLTP occurrences to coincide with suitable binary configurations for CE. This discrepancy suggests that VLTP events in binaries are less likely to explain all observed cases of born-again PNe.

The availability of a detailed investigation of the proper motion of the H-deficient knots in A 30 and A 78 using multi-epoch *HST* WFPC2 and WFC3 images (Fang et al., 2014) allows investigating their tangential velocity and thus their inclination in conjunction with the observed radial velocities. Unfortunately, the knots of the disrupted disk are not well resolved in our morpho-kinematic data and they cannot be assigned to the corresponding knot resolved in the *HST* images. However, this investigation is still viable for the polar knots.

For example, the proper motions of NW (J3) and SE (J1) clumps in A 30 are reported to be 7.93 and 6.99 mas yr^{-1}, respectively. At the updated distance to A 30 of 2.08±0.14 kpc (Bailer-Jones et al., 2021), this implies tangential velocities of 69 km s^{-1} for the NW jet (J3) and 78 km s^{-1} for the SE jet (J1). The observed averaged systemic radial velocities of these jets are -15 ± 5 km s^{-1} and $+21 \pm 5$ km s^{-1}, respectively, where the error is introduced to account for their velocity gradient in the PV maps. The tangential and radial velocities imply expansion velocities and inclinations with the plane of the sky of 71 ± 2 km s^{-1} and 12°±4° for the NW jet, and 81 ± 2 km s^{-1} and 15°±4° for the SE jet. These results indicate that the SE jet moves faster than the NW jet, as in the morpho-kinematic model presented Section 3, but, unlike in the model, the polar outflows are not orthogonal to the disrupted disk, which would require an inclination of 37°. This is not a major issue, as the inclination of the polar outflow in the model is an independent parameter that can be fine-tuned together with the expansion velocity of the outflow. Interestingly, the bipolar ejection in Sakurai's Object is neither orthogonal to its equatorial disk (see figure 2 in Hinkle et al., 2020). We note that the field of study of jet evolution and effects during the CE phase is very active, with simulations showing deviations from a linear motion and choking effects in jets (see, e.g., Zou et al., 2022, and references therein) that are not taken into account in the proposed CEBA scenario.

The comparison of the different born-again PNe in the previous section has evidenced that the H-poor ejecta in all of them can be interpreted as the combination of a disk and a jet. Their expansion velocities, however, are very different from one born-again PN to another. The disks and jets of A 30 and A 78 exhibit much lower expansion velocities than those of the Sakurai's Object, A 58 and HuBi 1, even though the current fast stellar wind from their CSPNe are imprinting momentum to the H-deficient clumps. It shall be noticed that, in the CEBA scenario, the bipolar ejection is produced by the presence of a companion. At early times, the velocity of the bipolar ejection is more or less the escape velocity

$$v_{\rm esc} = \sqrt{2G\frac{M}{R}}, \tag{3.2}$$

associated to the companion producing the jet, whereas the expansion velocity of the disk would depend both on the mass of the companion and its final orbital radius. There are no estimations of the mass and/or spectral types of the companions of the CSPN of born-again PNe, neither of their orbital radii, but it can be easily envisaged that a variety of those can produce very different initial values of the disk and jet velocities in born-again PNe that would explain the large difference of observed expansion velocities. On the other hand, the released energy of the VLTP is not the same for all born-again PNe (Miller Bertolami & Althaus, 2007), but we note that this idea seems more difficult to assess without modern stellar evolutionary models.

Chapter 4

Stellar evolution calculations of H-deficient stars

In this chapter, we present a review and analysis of stellar evolution models developed using the MESA (Modules for Experiments in Stellar Astrophysics Paxton et al., 2011, 2013, 2015, 2018, 2019) code. MESA is a widely used numerical simulation tool in astrophysics for studying the evolution of stars at various stages, from their formation to their most advanced phases.

The objective of this chapter is to explore how MESA can be applied to model low- and intermediate-mass stars ($1\ M_\odot < M < 8\ M_\odot$), which are the progenitors of PNe. We will closely examine how model parameters, such as initial abundances and masses, mass-loss rates, are adjusted, with a particular focus on those models that experience He flashes and evolve into H-deficient stars.

4.1 Set up of MESA models

As mentioned befores, MESA is an open-source stellar evolution package widely used and actively developed (Paxton et al., 2011, 2013, 2015, 2018, 2019). Its 1D stellar evolution module, MESAstar, has been rigorously tested against other stellar evolution codes and databases. MESAstar's modular, flexible infrastructure and robust numerical methods allow its application to diverse problems in computational stellar astrophysics, such as asteroseismology and binary star evolution.

MESAstar solves coupled Lagrangian structure and composition equations using a Newton-Raphson solver. Its modular structure, with individual thread-safe modules for numerics and input physics, facilitates experimentation with and implementation of different or new physics. User input is provided at runtime via the `inlist` file, and the `run_star_extras.f90` file allows further customization.

Key features include time step controls, adaptive mesh refinement, and parallelization. Time step controls ensure convergence and efficiency, using a scheme based on digital control theory. Mesh adjustments balance resolution and computational expense, minimizing numerical diffusion and improving convergence. MESA uses OpenMP for parallel computations, with performance improvements from a new

Table 4.1: Details of the MESA models configuration. **See text for definitions of different quantities**.

Parameter	Value
Equation of state	OPAL+SCVH+HELM+PC
Opacity	OPAL Type I for log$T \geq 4$; Ferguson for log$T \leq 4$
	Type I $\rightarrow$ Type II at the end of H burning
Convection: Ledoux + MLT	$\alpha_{\rm MLT} = 1.82$; $\nu = 1/3$; $y = 8$
Overshoot	time-dependent, diffusive, $f_{\rm ov,core} = 0.016$, $f_{\rm ov,sh} = 0.018$
	$D_0 = 0.5$
Semiconvection	$\alpha_{\rm sc} = 0.1$
Mass loss	$\eta_{\rm B} = 0.2$ for the AGB

linear algebra solver compatible with multicore processing.

In this section we review the relevant physics adopted in the models and their implementation in MESA. Table 4.1 presents a summary of the adopted physics.

The equation of state (EOS) tables in MESA are based on OPAL EOS tables (Rogers & Nayfonov, 2002), transitioning to SCVH tables (Saumon et al., 1995) at lower temperatures and densities. These extended tables cover various H (X) and metallicity (Z) values. HELM and PC tables (Potekhin & Chabrier, 2010) are used outside the covered range, assuming full ionization. MESA's EOS tables also include late stages of WD cooling phase adopting the definition from Miller Bertolami (2016).

MESA divides radiative opacity tables into high and low-temperature regimes, allowing user selection between Ferguson et al. (2005) or Freedman et al. (2008) tables for low temperatures and OPAL (Iglesias & Rogers, 1993, 1996) or OP tables (Seaton, 2005) for high temperatures. OPAL tables are further divided into Type I and II, with Type II addressing enhanced C and O abundances, crucial for He burning and beyond. Electron conduction opacity tables are based on Cassisi et al. (2007) but extended for higher temperatures and densities (Paxton et al., 2013).

MESA continues to refine diffusion implementation, especially for WD cooling phases, aiming to account for stronger coupled plasma interactions. The current diffusion implementation is limited to main-sequence stars above the fully convective limit, where it is most effective.

Mixing length theory (MLT) describes the convective transport of energy in the stellar interior. There is a vexing yet crucial free parameter of order unity, $\alpha_{\rm MLT}$, that determines how far a fluid parcel travels before it dissolves into the background. In other words, it parameterizes how efficient convection is, because a large $\alpha_{\rm MLT}$ means that the parcel travels a large distance before it deposits its energy into the ambient medium. Convective mixing of elements is treated as a time dependent diffusive process with a diffusion coefficient computed within the MLT formalism. We adopt the modified version of MLT from Henyey et al. (1965) instead of the standard MLT prescription (Cox & Stewart, 1965), as the latter assumes no radiative losses from fluid elements and is therefore applicable only at high optical depth. In addition to $\alpha_{\rm MLT}$, there are two free parameters, v and y, which are multiplicative factors to the

Table 4.2: Details of the initial parameters for our MESA models.

Parameter	Range	Δ
Initial mass	[1.0–2.5] $M_\odot$	0.1 $M_\odot$
Metalicity	[1.0–2.0] $Z_\odot$	0.5 $Z_\odot$
η_R	0.1, 0.5, 0.7	

mixing length velocity and the temperature gradient in the convective element. The latter two parameters are set to 8 and 1/3, respectively (see Henyey et al., 1965). This particular framework allows for convective efficiency to vary with the opacity of the convective element, an important effect to take into account in the layers near the stellar surface.

Mass loss is modeled using the Reimers (1975) prescription for the RGB phase and the Blöcker (1995) prescription for the AGB phase, which are:

$$\dot{M}_{\mathrm{R}} = 4 \times 10^{-13}\,\eta_{\mathrm{R}} \left(\frac{L}{\mathrm{L}_\odot}\right)\left(\frac{R}{\mathrm{R}_\odot}\right)\left(\frac{\mathrm{M}_\odot}{M}\right)\ \mathrm{M}_\odot\,\mathrm{yr}^{-1} \tag{4.1}$$

and

$$\dot{M}_{\mathrm{B}} = 4.83 \times 10^{-9}\,\eta_{\mathrm{B}} \left(\frac{L}{\mathrm{L}_\odot}\right)^{2.7}\left(\frac{\mathrm{M}_\odot}{M}\right)^{2.1}\ \mathrm{M}_\odot\,\mathrm{yr}^{-1}. \tag{4.2}$$

These approaches depend on overall stellar characteristics such as bolometric luminosity, radius, and mass, where η_{R} and η_{B} are parameters typically close to one. These parameters have been adjusted to align with various observational constraints, including the initial–final mass relation (IFMR; Kalirai et al., 2009), the AGB luminosity function (see Rosenfield et al., 2014), and asteroseismic data from open cluster members in the Kepler fields (Miglio et al., 2012). The Blöcker (1995) mass loss prescription was introduced as an alternative to the classic Reimers (1975) approach to account for the superwind phase observed in dynamical simulations of Mira-like variables' atmospheres. Nonetheless, these models remain empirically based and do not specify the exact mechanisms driving the winds (see Willson, 2000, for a discussion on, e.g., dust-driven winds).

For simplicity, Reimers mass loss is applied from the start of the evolution, though minimal mass loss occurs during the main sequence. Once the He core is depleted, the mass-loss rate is determined by the maximum of $\dot{M}_{\mathrm{R}}$ and $\dot{M}_{\mathrm{B}}$ at any given time. The commonly adopted values for these parameters are $\eta_{\mathrm{R}} = 0.5$ and $\eta_{\mathrm{B}} = 0.2$. However, we wanted to explore how the efficiency in the RGB phase could effect the occurrence of VLTP events, so we also use a η_{R}=0.1 and 0.7.

4.2 Searching for VLTP models

We created a grid of 225 models, varying the initial mass from 1 to 2.5 $\mathrm{M}_\odot$ and the metallicity between 1 to 2 $Z_\odot$,with $Z_\odot$ ≈0.0134 and a He abundance of Y ≈0.2485 (Asplund et al., 2009), as shown in Table 4.2. Our goal was to study the role played

Table 4.3: Details of our stellar evolution models that experienced a **LTP**.

Model	$M_{\rm ZAMS}$ [M$_\odot$]	Z [$Z_\odot$]	$\eta_{\rm R}$	$M_{\rm remnant}$ [M$_\odot$]	$\dot{M}_{\rm LTP}$ [M$_\odot$ yr^{-1}]	$t_{\rm LTP}$ [yrs]
1	1.0	1.0	0.5	0.5294	4.1×10^{-7}	500
2	1.2	1.0	0.5	0.5428	5.8×10^{-7}	300
3	1.2	1.5	0.5	0.5462	9.0×10^{-7}	340
4	1.4	2.0	0.5	0.5614	8.8×10^{-7}	290
5	1.1	1.0	0.7	0.5307	4.9×10^{-7}	500
6	1.2	1.5	0.7	0.5411	1.2×10^{-6}	470

by variations in our initial parameters in the production (or not) of VLTP events. In Figures 4.1, 4.2 and 4.3, we present the evolutionary tracks for all the models in our grid. We have 6 successful models with different initial parameters. The initial parameters, mass-loss rate, the remnant mass and the time this phase last, for each model, are listed in table 4.3. In the evolutionary tracks, we present more successful models than those reported in Table 4.3, as we excluded models that exhibited unusual behavior and numerical errors during the post-VLTP evolution, to ensure the reliability and accuracy of our analysis. The evolutionary track of each successful model can be seen individually in Figure 4.4, where we can observe the subtle differences in each born-again model, such as the temperature decrease, the depth at the WD cooling track when the star begins the He flash (red dots), the end of the late thermal pulse (blue square) and the presence of a small loop after the He flash in all models.

The duration of the thermal pulse in these models, that is, the time elapsed between the red circle and the blue square in Figure 4.4, ranges from 200 to 500 yr. We found that during this period, the star loses up to 1.2×10^{-6} M$_\odot$.

One of the output parameters provided by MESA is the luminosity of different elements, such as H ($L_{\rm H}$) and He ($L_{\rm He}$). The luminosities $L_{\rm H}$ and $L_{\rm He}$ are related to the burning stages of these elements within the star. They represent the amount of energy being generated through the nuclear fusion of H and He, respectively. This provides crucial information about the internal processes occurring in the star, especially during phases where the fusion rate of one element dominates over the other, such as during a He flash or subsequent quiescent burning stages. As described by Iben (1981) and others, the VLTP is characterized not simply by a sudden He shell flash, but by the occurrence of a subsequent H flash following the He shell flash. This sequence of events drastically alters the star's luminosity and composition, distinguishing the VLTP from other thermal pulse events. Figure 4.5 presents the evolution of $L_{\rm H}$ and $L_{\rm He}$ in the moments leading up to the He flash and thousands of years thereafter.

Our goal was to study VLTPs and how different parameters could affect the stellar evolution, specially the physical and chemical structures of the stars in our models. Exploring the evolutionary tracks of the models we thought 6 of them were successful (Figure 4.4), we inferred that these stars had experienced a VLTP. However, by looking at the $L_{\rm H}$ and $L_{\rm He}$ of these stars when the He flash occurred, we realized that these stars actually experienced a late thermal pulse (LTP). During an LTP, H

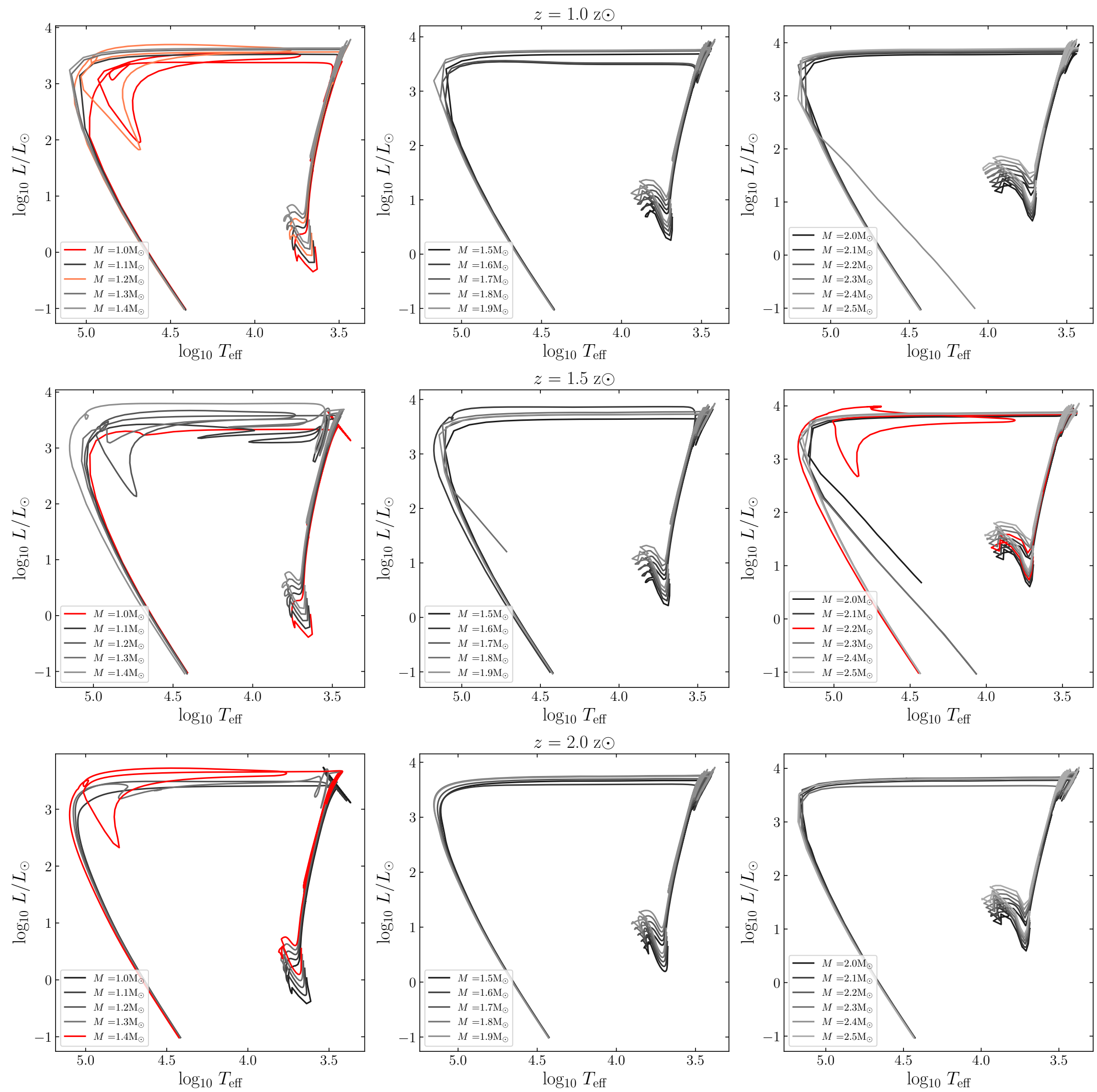

Figure 4.1: Evolutionary tracks for models with $\eta_{\rm R}$ = 0.5. The red lines represent models that produce a VLTP-like event.

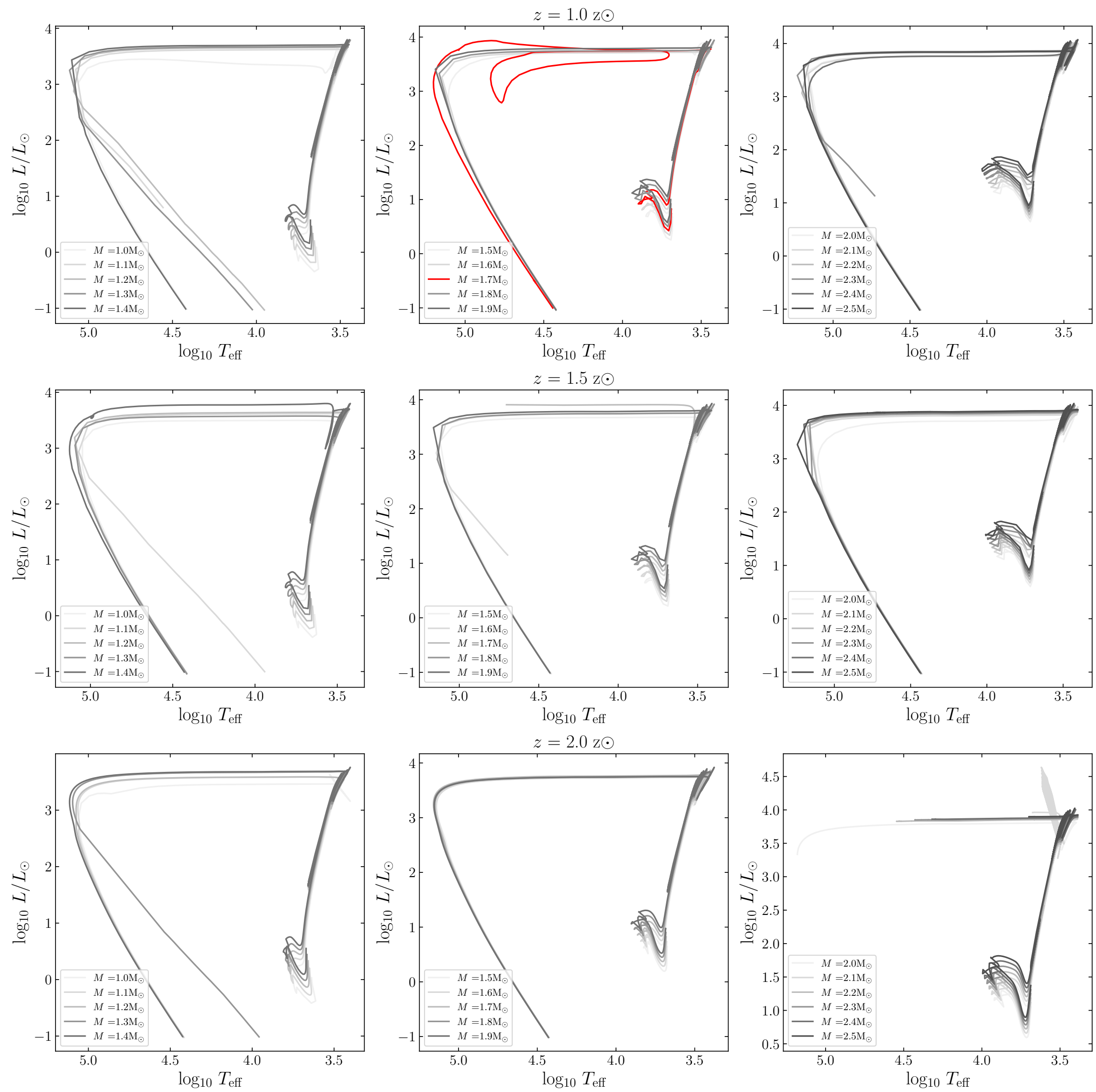

Figure 4.2: Same as Fig. 4.1 but for evolutionary tracks for models with $\eta_{\rm R} = 0.1$.

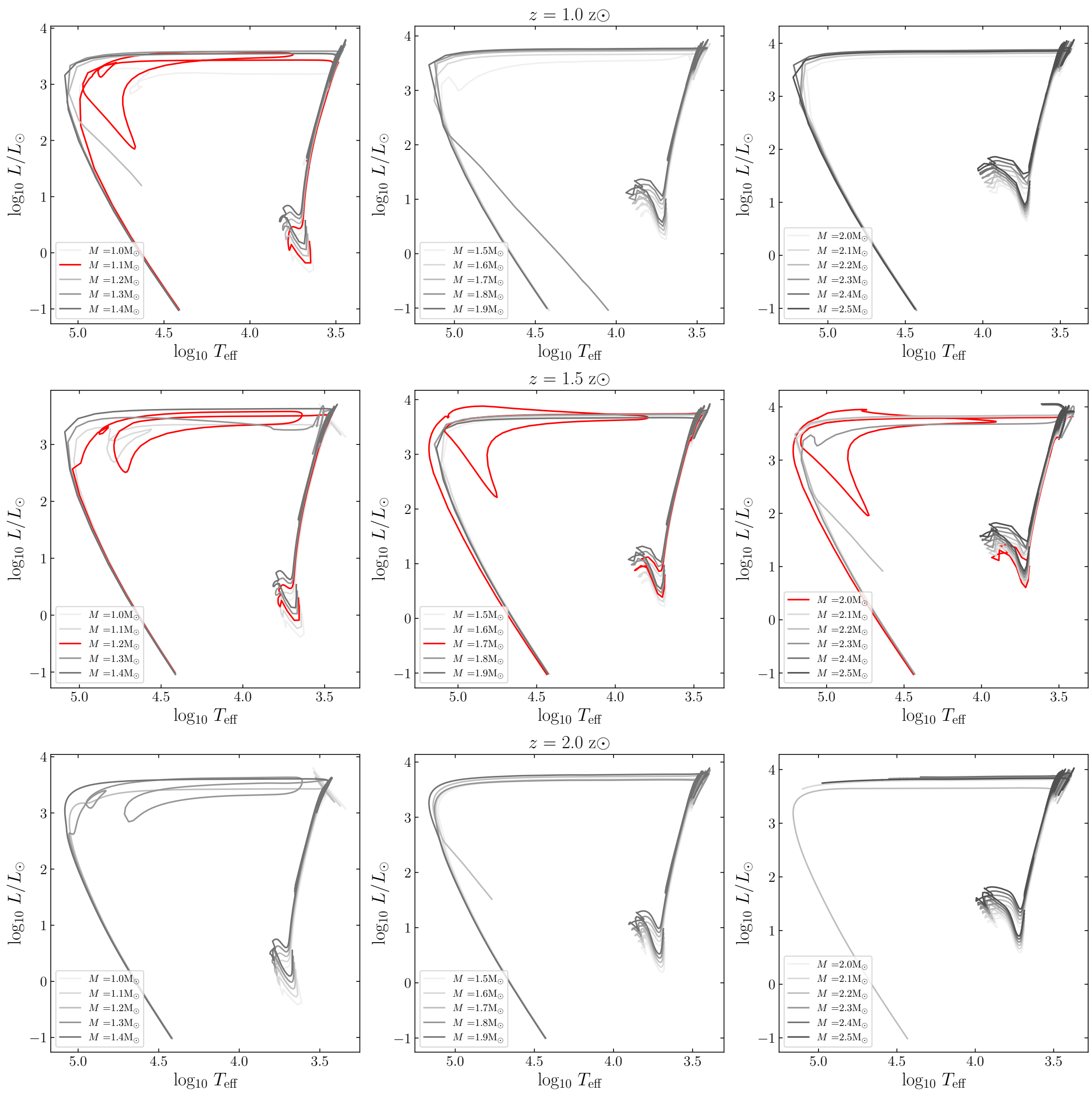

Figure 4.3: Same as Fig. 4.1 but for evolutionary tracks for models with $\eta_{\rm R} = 0.7$.

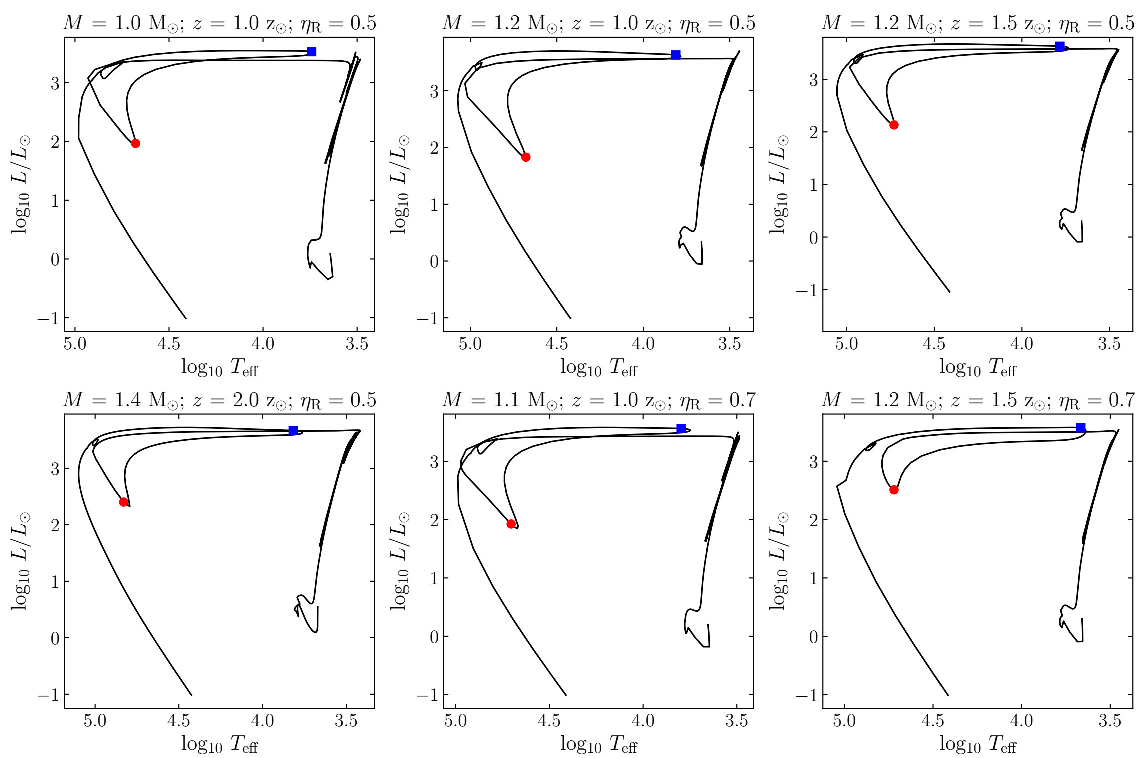

Figure 4.4: Evolutionary tracks of our stellar evolution models that exhibited a thermal pulse. Red circles shows the star of He flash, while blue squares shows when the star returns to the post-AGB phase for a second time.

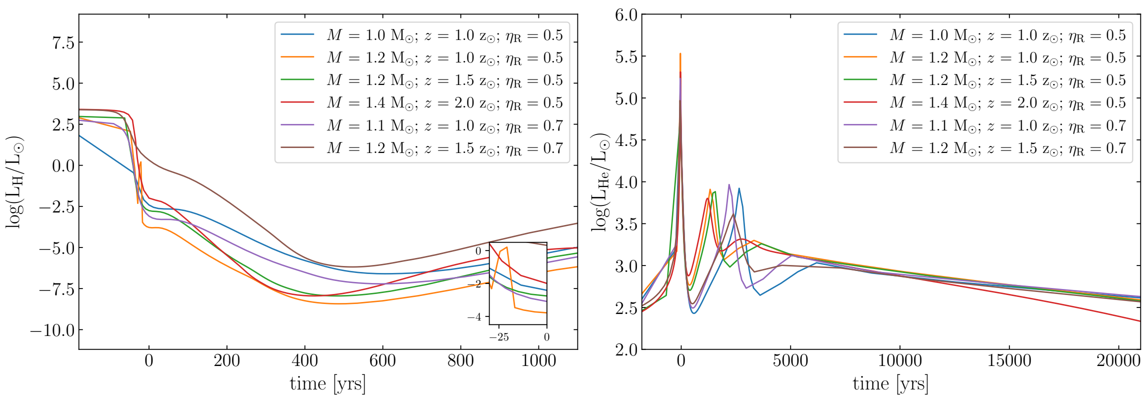

Figure 4.5: Evolution of L_H (left) and L_He (right) during the VLTP (black square) and post-LTP. The inset in the left panel shows the moment when one of the models experienced an unexpected increase in L_H.

dilution occurs as the lower edge of the convective envelope penetrates H-deficient regions following an intense He flash. This He flash pushes the star back toward the giant branch, altering surface abundances in some cases. However, in low-mass stars that did not undergo a third dredge-up on the AGB, the LTP does not significantly change surface composition. Only more massive stars, which experienced a third dredge-up prior to the LTP, display H-deficient surface compositions similar to PG 1159 stars, showing enhanced abundances of He, C, and O (Herwig, 2001). Stars that experience an LTP or a VLTP do not exhibit identical behavior in the HR diagram. In VLTP models, the star's luminosity drops drastically—by several orders of magnitude—after the event, as shown in Figure 1.6. In contrast, the luminosity drop following an LTP is far more moderate. This difference in luminosity decline highlights distinct evolutionary responses to LTP and VLTP events.

LTPs happen when the star still possesses a considerable H envelope, typically during the post-AGB phase. In this case, the thermal pulse does not completely consume the H, leaving an appreciable amount in the stellar atmosphere. As a result, the surface abundances undergo moderate changes, with an enrichment in elements such as C, N, and O. However, the H signature remains present (see Fig. 4.6.)

On the other hand, VLTPs occur at a much more advanced evolutionary stage, when the star is descending the cooling branch towards the WD. At this point, the H envelope is much thinner, and the thermal pulse is capable of burning virtually all the residual H. This leads to a drastically different surface chemical composition, characterized by an extremely low abundance of H and a significant enrichment in C and O. This distinction between LTPs and VLTPs is clearly illustrated in Figure 4.6, which shows the typical surface abundances for each type of thermal pulse.

What is particularly noteworthy in our models is that there are two additional significant increases in L_He after the LTP. The final peaks in L_He correspond to the small secondary loop seen in these models as the star returns to the WD cooling track for the second time (see Figure 4.4). This behavior indicates complex thermonuclear

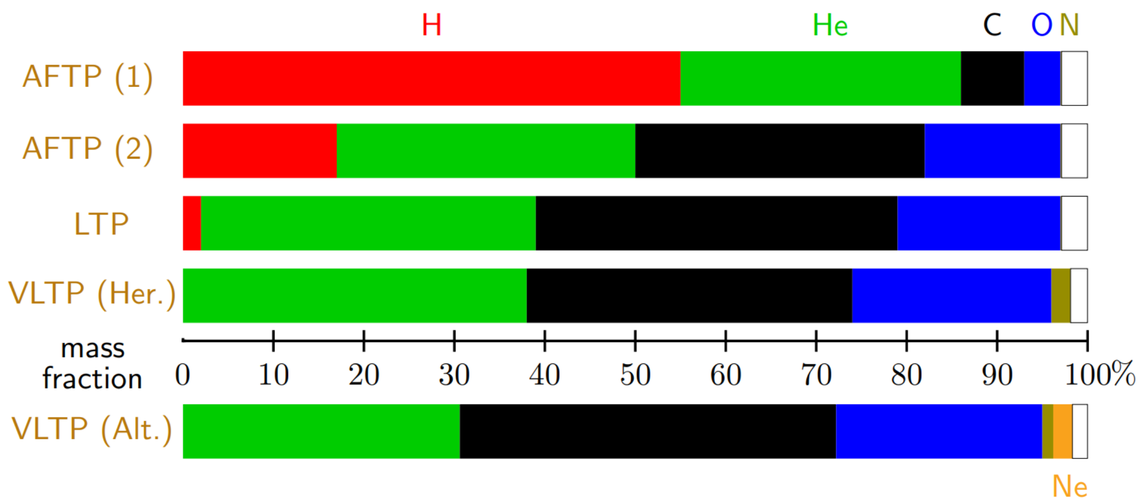

Figure 4.6: Stellar surface abundances predicted from stellar evolution models for different TP (Herwig, 2001; Werner & Herwig, 2006). This figure was taken from Todt & Hamann (2015)

processes occurring in the late stages of evolution, which can lead to the formation of H-deficient, He-rich post-AGB stars.

A critical aspect of MESA models for stars that undergo a LTP is the resulting changes in elemental abundances. Following an LTP, significant alterations are expected: specifically, a decrease in H abundance and an increase in He abundance. However, our models show a different trend. As illustrated in Fig. 4.7, the anticipated decrease in H abundance is not evident in most of our models; when it does occur, it is only slight. This discrepancy is not due to any limitation within MESA but is instead a natural consequence of using low-mass models that do not undergo a third dredge-up episode. In low-mass stars, the LTP does not lead to deep enough mixing to produce H-deficient surfaces. In contrast, more massive stars that experience third dredge-up prior to the LTP are likely to become H-deficient afterward. Earlier work by Herwig (2001) utilized a reduced diffusion coefficient to adjust mixing in VLTP models, but the VLTP models by Miller Bertolami et al. (2006) and Miller Bertolami & Althaus (2007) used standard diffusion coefficients derived from the Mixing Length Theory (MLT). Therefore, MESA's challenges in accurately simulating VLTPs are not due to an incorrect diffusion coefficient.

We note that another major limitation of current stellar evolution codes is the unknown mass loss rate for H-deficient stars. This weakness of stellar evolution codes should impact models intended for the CSPN of born-again PNe and those that evolve through a LTP event as they are known to be H-deficient, WR-type stars (e.g., Weidmann et al., 2020). In a recent study, Toalá et al. (2024) analyzed WR and [WR] stars and made predictions for their stellar winds. In our MESA models, we implemented the wind prescriptions found by Toalá et al. (2024) to more accurately represent the mass loss rates of these H-deficient stars. We edited MESA to include

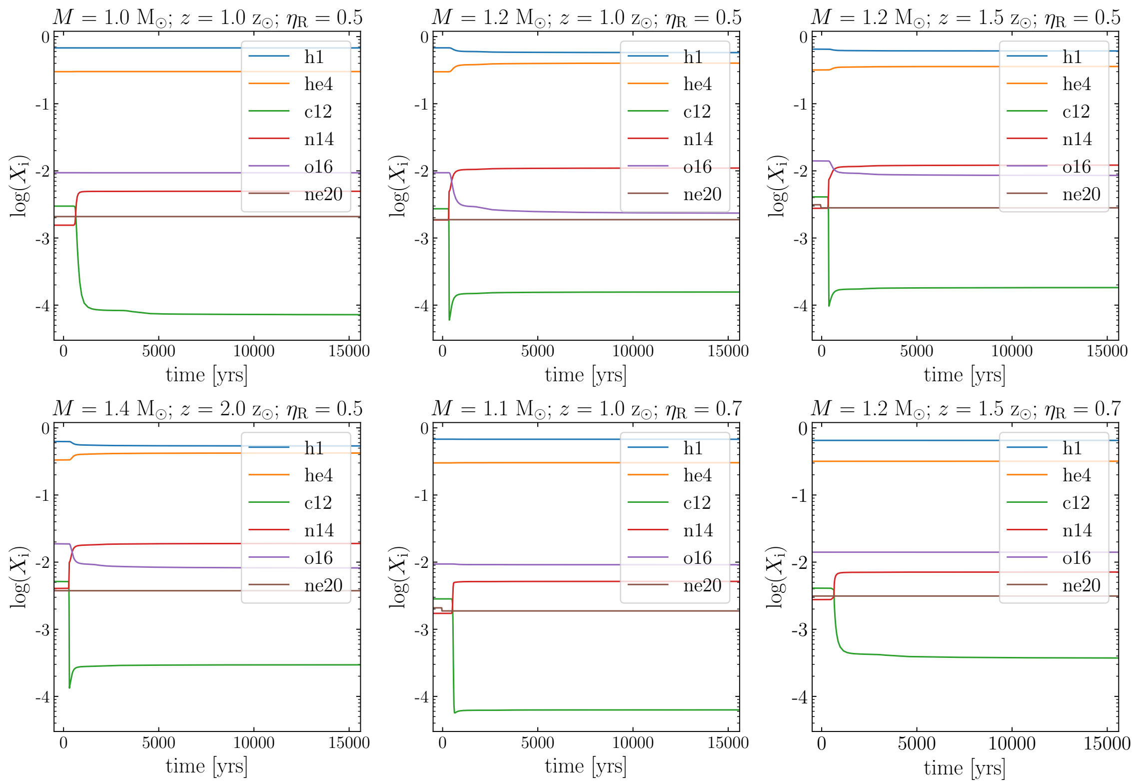

Figure 4.7: Elemental abundance evolution of our stellar evolution models that experienced a LTP. See details in Table 4.3. The time $t = 0$ denotes the moment the star experienced a LTP.

the relationship between the stellar luminosity L, the effective temperature $T_{\rm eff}$ and the mass-loss rate $\dot{M}$ as

$$\log_{10}\left(\frac{\dot{M}}{\mathrm{M_\odot\ yr^{-1}}}\right) = (1.23\pm0.42)\log_{10}\left(\frac{L}{\mathrm{L_\odot}}\right) - (0.68\pm0.57)\log_{10}\left(\frac{T_{\rm eff}}{\mathrm{K}}\right) - (8.11\pm0.46), \tag{4.3}$$

with a wind efficiency parameter η is defined as :

$$\eta = \frac{\dot{M} v_\infty}{L/c}. \tag{4.4}$$

This wind prescription is particularly important for reproducing the physical conditions of born-again CSPNe, where the loss of mass plays a critical role in the evolution of the star.

To further explore the impact on the final properties of stars that experienced a LTP event in our MESA grid, those illustrated in Figure 4.4, we included the wind relationships of Toalá et al. (2024). The results are presented in Figure 4.8. However, it is important to note that applying [WR] wind prescriptions to stars with H-rich envelopes is not physically realistic. [WR] winds are characteristic of stars that have

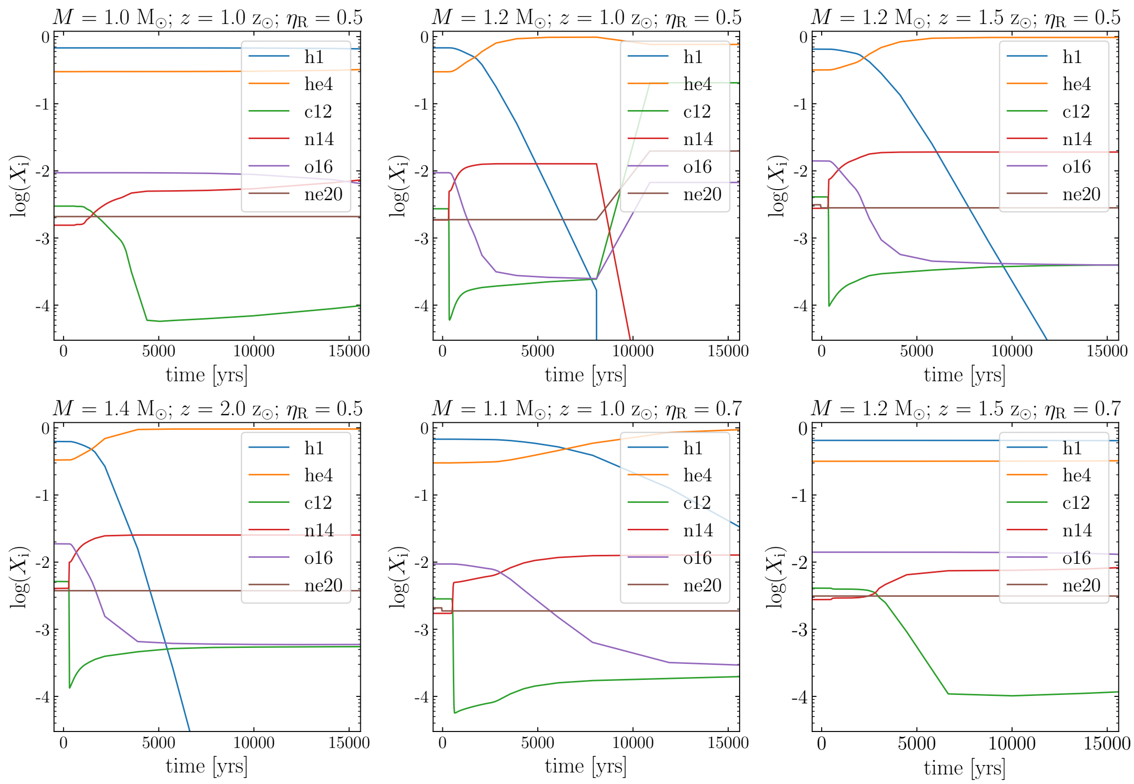

Figure 4.8: Same as Figure 4.7 but in these cases we used the wind recipes of Toalá et al. (2024) in the post-LTP evolution.

already become H-deficient after the AGB phase, where the wind is driven by the altered surface composition. Therefore, using these H-deficient wind models on H-rich stars artificially removes the H layer, as observed in Figure 4.7. This exercise demonstrates how such [WR]-type winds would impact the envelope but does not represent a realistic scenario for stars that retain H.

4.3 Final remarks

Our goal in this chapter was to use MESA to produce stellar evolution models of Solar-like stars that experience a VLTP event, that is, models that can be used to study the properties of stars that become born-again stars. However, it is evident that while MESA provides a strong foundation for modeling stellar evolution, it is not sufficient to fully explore born-again phenomena without incorporating more accurate wind prescriptions and improved diffusion treatments. MESA struggle in reproduces the L_{He} expected for a VLTP event, the He flash is a key feature in the evolution of born-again stars, and accurately modeling L_{He} is crucial for capturing the energy output during these phases. MESA tends to underestimate L_{He}, resulting in a model that does not fully account for the thermonuclear ignition of He in the stellar shell. In order to accurately reproduce the dynamics of VLTP events, larger L_{He} values are needed to match observations and theoretical predictions of these stars' behavior during their born-again transformation. Additionally, MESA do not reproduce the expected abundances for stars undergoing a VLTP , which is essential for understanding the born-again process. From our analysis, we conclude that MESA produces stellar evolution models for LTP events.

To address these shortcomings, the implementation of wind prescriptions for [WR] stars, such as those proposed by Toalá et al. (2024), is crucial, as these provide a more realistic representation of the mass-loss rates for H-deficient stars. Additionally, improvements in the treatment of mixing processes and diffusion would help to obtain a better description of our models. Accurately simulating the detailed evolution of CSPNe undergoing a VLTP primarily depends on fine-tuning and rigorously testing the code's numerical parameters. This includes adjustments to time-step control and spatial resolution settings to handle the intense H burning phase that follows the helium flash. With careful optimization of these numerical settings, MESA can achieve reliable VLTP simulations, ensuring accurate predictions of evolutionary outcomes without further code modifications. Future work will focus on refining these parameter settings to enhance MESA's capability in modeling VLTP events.Such modifications to the MESA code, will be pursued in the near future.

Chapter 5

Conclusions and future work

In this thesis, we presented a study of the properties of born-again PNe, those objects that are suggested to have experienced a VLTP. We used a combination of theoretical tools with observations to peer into the formation and evolution of the born-again PNe A 30, A78, and HuBi 1.

The main conclusions of this thesis are:

- We presented the photoionization models of the born-again PNe A 78 and HuBi 1 using the code Cloudy including gas and dust. We included the contribution from non-LTE stellar atmosphere models to account for reliable ionizing photon fluxes from these H-deficient stars.

  Our best models are able to reproduce publicly available photometric observations as well as the fluxes from optical emission lines measured from high-resolution optical spectroscopy. We have shown that the C/O ratio is greater than 1, which is consistent with the abundances expected from a VLTP ejecta. This is a result similar to that seen by Toalá et al. (2021) for A 30, showing that for these objects a more detailed characterization of the dust is necessary to unravel the origin of the H-poor material.

  The models predicts that the largest carbonaceous grains are located in the outer shell whilst the smallest dust grains are located in the inner structure. The physics of dust grain destruction and evolution is currently not included in our photionisation model and will require detailed radiation-hydrodinamical simulations to peer into the physics behind these properties.

- Based on high-dispersion spectroscopic observations obtained with the MES instrument mounted at the 2.1 m San Pedro Mártir (SPM) telescope, we produced morpho-kinematic models of A 30 and A 78 to confirm that the H-deficient material close to their CSPN consist of disrupted disks and bipolar ejections. Although these structures had been previously suggested, this study provides the first direct confirmation of their presence. Similar morphologies have been detected in other born-again planetary nebulae, such as A58 and Sakurai's object using radio observations, further supporting the idea that H-deficient material is commonly organized in this fashion in such nebulae. These findings align with those reported by Montoro-Molina et al. (2023) and Tafoya et al. (2022), who also observed disk and bipolar ejection features in other H-deficient planetary nebulae, highlighting a consistent pattern in the evolution of born-again stars.

Our SHAPE models of A78 and A30 reveal that the disk structures in these nebulae exhibit higher expansion velocities (in the case of A30) or similar velocities (in the case of A78) compared to the bipolar structures. This behavior is consistent with the proper motion observations previously reported by Fang et al. (2014), who noted similar velocity patterns in both nebulae. These findings suggest a dynamic interaction between the disk and bipolar ejections in born-again planetary nebulae, providing valuable insights into the complex kinematic behavior of H-deficient materials in these objects. The alignment between our modeling results and the observational data highlights the robustness of the SHAPE code in accurately representing the kinematic properties of such intricate structures.

We propose that the jets of A 30 and A 78 have been produced during a CE phase between its CSPN and a companion. When their CSPNe experienced the VLTP, it might have inflated its outer layers causing a CE phase. The subsequent fast evolution of this CSPNe after the born-again event produced the current high ionization photon flux and fast stellar wind, which affects more strongly to the structure close to the CSPN, i.e, the disk. We suggest that whereas the kinematic properties of the jet-like features are currently similar to those during the CE phase, the clumps in the disk have experienced a strong acceleration caused by the fast stellar wind.

We propose that other born-again PNe can also be explained by the proposed CEBA scenario presented here. In particular, we suggest that A 30 and A 78 are at the same late stage of evolution, when wind momentum is efficiently transferred to the clumps in the disk and $v_{\rm jet} < v_{\rm disk}$. The younger born-again PNe A 58 and Sakurai's Object are arguably at a previous stage, when their CSPNe have not developed a strong stellar wind nor a strong UV flux to imprint momentum into the H-deficient material so that $v_{\rm jet} > v_{\rm disk}$. HuBi 1 would be in the transition between these two phases, with $v_{\rm jet} \simeq v_{\rm disk}$.

- We used the stellar evolution code MESA to try to produce new models of the VLTP event in low-mass stars. We found out that accurately simulating the detailed evolution of CSPNe undergoing a VLTP primarily depends on fine-tuning and rigorously testing the code's numerical parameters. This includes adjustments to time-step control and spatial resolution settings to handle the intense H burning phase that follows the helium flash. With careful optimization of these numerical settings, MESA can achieve reliable VLTP simulations, ensuring accurate predictions of evolutionary outcomes without further code modifications. Future work will focus on refining these parameter settings to enhance MESA's capability in modeling VLTP events.

  To further push the predictions of the abundances of our LTP models, we incorporated recent predictions for the winds of WR-type stars from Toalá et al.

(2024). We found that with this wind prescription, the H layer is eliminated in less than 10,000 years, leading to drastic changes in the chemical abundances of the star. This suggests that an appropriate wind and mixing treatment is **interesting** for accurately modeling the evolution of stars that undergo LTPs and potentially VLTPs, providing more realistic insights into the chemical evolution of H-deficient stars.

A crucial step for advancing our understanding of born-again PNe is the improved characterization of these objects and to identify more candidates. Achieving this requires better quality observations. Our group has recently obtained observations of the PNe A 30, A 78 and WR72 using the MEGARA integral field spectrograph, which will provide unprecedented insights into their morpho-kinematic properties without relying on assumptions. These observations will enhance our ability to identify the distinct features of born-again nebulae and refine the criteria for classifying similar objects.

Finally, future radiation-hydrodynamic simulations will be essential for understanding the evolution of born-again PNe and testing our formation scenario through a common envelope. Those simulations will help clarify the physical processes involved in the late evolutionary phases of H-deficient stars and the impact on their surrounding nebulae. By combining observational data with state-of-the-art simulations, we can deepen our understanding of the mechanisms driving the born-again phenomenon and its role in the late stages of stellar evolution.

Bibliography

Althaus, L. G., Serenelli, A. M., Panei, J. A., et al. 2005, AaP, 435, 631.

Asplund, M., Grevesse, N., Sauval, A. J., et al. 2009, MNRAS, 307, L11.

Bailer-Jones, C. A. L., Rybizki, J., Fouesneau, M., et al. 2018, AJ, 156, 58

Bailer-Jones, C. A. L., Rybizki, J., Fouesneau, M., et al. 2021, AJ, 161, 147.

Balick, B., Preston, H. L., & Icke, V. 1987, AJ, 94, 1641

Blöcker, T. 2001, APSS, 275, 1.

Bloecker, T. 1995, AAP, 297, 727

Borkowski, K. J., Harrington, J. P., & Tsvetanov, Z. I. 1995, ApJl, 449, L143

Borkowski, K. J., Harrington, J. P., Blair, W. P., et al. 1994, ApJ, 435, 722.

Borkowski, K. J., Harrington, J. P., Tsvetanov, Z., et al. 1993, ApJl, 415, L47

Cassisi, S., Potekhin, A. Y., Pietrinferni, A., et al. 2007, ApJ, 661, 1094.

Chaboyer, B., Fenton, W. H., Nelan, J. E., et al. 2001, ApJ, 562, 521.

Chamandy, L., Blackman, E. G., Frank, A., et al. 2020, MNRAS, 495, 4028.

Chatzikos, M., Bianchi, S., Camilloni, F., et al. 2023, RMXAA, 59, 327

Chesneau, O., Clayton, G. C., Lykou, F., et al. 2009, AAP, 493, L17.

Chu, Y.-H., Chang, T. H., & Conway, G. M. 1997, ApJ, 482, 891. doi:10.1086/304196

Chu, Y.-H., Jacoby, G. H., & Arendt, R. 1987, ApJs, 64, 529

Ciardullo, R., Bond, H. E., Sipior, M. S., et al. 1999, AJ, 118, 488 Magnitud

Clayton, G. C. & De Marco, O. 1997, AJ, 114, 2679. doi:10.1086/118678

Clayton, G. C., Bond, H. E., Long, L. A., et al. 2013, ApJ, 771, 130.

Clayton, G. C., Kerber, F., Pirzkal, N., et al. 2006, ApJl, 646, L69.

Clegg, R. E. S., Seaton, M. J., Peimbert, M., et al. 1983, MNRAS, 205, 417

Cohen, M. & Barlow, M. J. 1974, ApJ, 193, 401

Cohen, M., Hudson, H. S., O'Dell, S. L., et al. 1977, MNRAS, 181, 233.

Collaboration, G. et al. VizieR Online Data Catalog: Gaia DR2, 2018,

Condon, J. J. & Kaplan, D. L. 1998, ApJs, 117, 361.

Corradi, R. L. M., Sánchez-Blázquez, P., Mellema, G., et al. 2004, AAP, 417, 637

Cox, A. N. & Stewart, J. N. 1965, ApJs, 11, 22

Cox, N. L. J., Kerschbaum, F., van Marle, A.-J., et al. 2012, AAP, 537, A35

Curtis, H. D. 1918, Publ. Lick Obs., 13, 57

De Marco, O., Barlow, M. J., Storey, P. J., & Liu, X. W. 1997, MNRAS, 292, 86

Dinerstein, H. L. & Lester, D. F. 1984, ApJ, 281, 702

Duerbeck, H.W. and Benetti, S., 1996, ApJ, 468, L111.

Evans, A., Gehrz, R. D., Woodward, C. E., et al. 2020, MNRAS, 493, 1277

Evans, A., Tyne, V. H., van Loon, J. T., et al. 2006, MNRAS, 373, L75.

Eyres S. P. S., Geballe T. R., Tyne V. H., Evans A., Smalley B., Worters H. L., 2004, MNRAS, 350, L9.

Eyres S. P. S., Smalley B., Geballe T. R., Evans A., Asplund M., Tyne V. H., 1999, MNRAS, 307, L11.

Eyres, S. P. S., Evans, A., Geballe, T. R., et al. 1998, MNRAS, 298, L37

Fang, X., Guerrero, M. A., Marquez-Lugo, R. A., et al. 2014, ApJ, 797, 100.

Fang, X., Zhang, Y., Kwok, S., et al. 2018, ApJ, 859, 92

Faulkner, D.J., 1970, ApJ, 162, 513

Feibelman, Walter A. 1999, ApJ, 514, 296

Ferguson, J. W., Alexander, D. R., Allard, F., et al. 2005, ApJ, 623, 585. doi:10.1086/428642

Ferland, G. J., Chatzikos, M., Guzmán, F., et al. 2017, RMxAA, 53, 385

Freedman, R. S., Marley, M. S., & Lodders, K. 2008, ApJs, 174, 504.

Frew, D. J., Parker, Q. A., & Bojičić, I. S. 2016, MNRAS, 455, 1459.

García-Hernández, D. A., Rao, N. K., & Lambert, D. L. 2013, ApJ, 773, 107.

García-Segura, G., Langer, N., Różyczka, M., et al. 1999, ApJ, 517, 767

García-Segura, G., Taam, R. E., & Ricker, P. M. 2020, ApJ, 893, 150

García-Segura, G., Taam, R. E., & Ricker, P. M. 2021, ApJ, 914, 111.

García-Segura, G., Villaver, E., Langer, N., et al. 2014, ApJ, 783, 74.

García-Segura, G., Villaver, E., Manchado, A., et al. 2016, ApJ, 823, 142.

Gehrz, R. D., Woodward, C. E., Temim, T., et al. 2005, ApJ, 623, 1105.

Gehrz, R.D. and Woolf, N., 1971, ApJ, 165, 285

Gontcharov, G.A., 2006, Astronomy Letters, 32, 759

Górny, S. K., & Tylenda, R. 2000, A&A, 362, 1008

Gräfener, G., Koesterke, L., & Hamann, W.-R. 2002, AaP, 387, 244

Greenstein, J. L. 1981, ApJ, 245, 124

Guerrero M. A., Fang X., Miller Bertolami M. M., Ramos-Larios G., Todt H., Alarie A., Sabin L., et al., 2018, NatAs, 2, 784.

Guerrero, M. A. & De Marco, O. 2013, AAP, 553, A126

Guerrero, M. A. & Manchado, A. 1996, ApJ, 472, 711.

Guerrero, M. A., Ramos-Larios, G., Toalá, J. A., et al. 2020, MNRAS, 495, 2234

Guerrero, M. A., Ruiz, N., Hamann, W.-R., et al. 2012, ApJ, 755, 129

Guerrero, M. A., Toalá, J. A., Medina, J. J., et al. 2013, AAP, 557, A121

Guerrero, M.A., Fang, X., Bertolami, M.M.M., Ramos-Larios, G., Todt, H., Alarie, A., Sabin, L., Miranda, L.F., Morisset, C., Kehrig, C. and Zavala, S.A., 2018, Nature Astronomy, 2, 784

Gvaramadze, V. V., Kniazev, A. Y., Gräfener, G., et al. 2020, MNRAS, 492, 3316

Habing, H. J., & Olofsson, H. 2003, Asymptotic Giant Branch Stars, Springer Science & Business Media

Hajduk, M., van Hoof, P. A. M., Śniadkowska, K., et al. 2018, MRAS, 479, 5657.

Hamann, W.-R. & Gräfener, G. 2004, AaP, 427, 697

Harrington, J. P. 1996, Hydrogen Deficient Stars, 96, 193

Hazard, C., Terlevich, R., Morton, D. C., et al. 1980, NATURE, 285, 463.

Henyey, L., Vardya, M. S., & Bodenheimer, P. 1965, ApJ, 142, 841.

Herwig, F., Blöcker, T., Langer, N., et al. 1999, AAP, 349, L5. doi:10.48550/arXiv.astro-ph/9908108

Herwig, F. 2001, ApJl, 554, L71. doi:10.1086/320911

Hinkle K. H., Joyce R. R., 2014, ApJ, 785, 146. doi:10.1088/0004-637X/785/2/146

Hinkle, K. H. & Joyce, R. R. 2014, ApJ, 785, 146

Hinkle, K. H., Joyce, R. R., Matheson, T., et al. 2020, ApJ, 904, 34.

Hinkle, K. H., Lebzelter, T., Joyce, R. R., et al. 2008, AAP, 479, 817.

Hog, E., Fabricius, C., Makarov, V. V. et al. 2000, A&A, 355L, 27H

Hu, J. Y. & Bibo, E. A. 1990, AAP, 234, 435

Hu, J. Y. & Bibo, E. A. 1990, AaP, 234, 435

Hunter, J. D. 2007, Computing in Science and Engineering, 9, 90.

Iben, I. 1984, ApJ, 277, 333. doi:10.1086/161700

Iben, I. & MacDonald, J. 1995, White Dwarfs, 48

Iben, I. Jr. 1981, in Astrophysics and Space Science Library, ed. I. Iben Jr., & A. Renzini (Vol. 88, Physical Processes in Red Giants), D. Reidel Publishing Co, Dordrecht, 3

Iben, I., Jr., MacDonald, J. 1995, in White Dwarfs, eds. D. Koester & K. Werner, Berlin: Springer), 48

Iben, I., Kaler, J. B., Truran, J. W., et al. 1983, ApJ, 264, 605.

Iben, I., Tutukov, A.V. and Yungelson, L.R., 1996, In Hydrogen Deficient Stars, 96, 409

Iglesias, C. A. & Rogers, F. J. 1993, ApJ, 412, 752.

Iglesias, C. A. & Rogers, F. J. 1996, ApJ, 464, 943.

Ivanova, N., Justham, S., Chen, X., De Marco, O., Fryer, C. L., Gaburov, E., ... & Taam, R. E. 2013, AARv, 21, 59

Jacoby, G. H. & Chu, Y.-H. 1989, Planetary Nebulae, 131, 183

Jacoby, G. H. & Ford, H. C. 1983, ApJ, 266, 298.

Jacoby, G. H., Hillwig, T. C., & Jones, D. 2020, MNRAS, 498, L114. doi:10.1093/mnrasl/slaa138

Jacoby, G. H. 1979, PASP, 91, 754. doi:10.1086/130582

Jeffery, C. S. & Schönberner, D. 2006, AAP, 459, 885. doi:10.1051/0004-6361:20047075

Jiménez-Hernández, P., Arthur, S. J., & Toalá, J. A. 2020, MNRAS, 497, 4128. doi:10.1093/mnras/staa2272

Kaler, J. B. 1983, ApJ, 271, 188

Kalirai, J. S., Saul Davis, D., Richer, H. B., et al. 2009, ApJ, 705, 408.

Karttunen, H., Kröger, P., Oja, H., Poutanen, M., & Donner, K. J. 2016. Fundamental astronomy. Springer.

Kerber, F., Pirzkal, N., De Marco, O., et al. 2002, ApJl, 581, L39.

Kim, H., Liu, S.-Y., & Taam, R. E. 2019, ApJs, 243, 35

Kimeswenger, S., Kerber, F., & Weinberger, R. 1998, MNRAS, 296, 614

Koesterke, L., Dreizler, S., & Rauch, T. 1998, A&A, 330, 1041

Koller, J. & Kimeswenger, S. 2001, ApJ, 559, 419

Kutter, G.S. and Sparks, W.M., 1974, ApJ, 192, 447

Kwok, S., 2007, The origin and evolution of planetary nebulae, Cambridge University Press.

Kwok, S., Purton, C. R., & Fitzgerald, P. M. 1978, ApJl, 219, L125

Lagage, P. O., Pel, J. W., Authier, M., et al. 2004, The Messenger, 117, 12

Lamers, H. J. G. L. M. & Cassinelli, J. P. 1999, Introduction to Stellar Winds, by Henny J. G. L. M. Lamers and Joseph P. Cassinelli, pp. 452. ISBN 0521593980. Cambridge, UK: Cambridge University Press, June 1999., 452

Lau, H. H. B., De Marco, O., & Liu, X.-W. 2011, MNRAS, 410, 1870.

Lawlor, T. M., & MacDonald, J. 1999, AAS, 195, 4406L

Lawlor, T. M., & MacDonald, J. 2006, MNRAS, 371, 263

Lawlor, T. M. & MacDonald, J. 2003, ApJ, 583, 913.

Lawlor, T. M. 2023, MNRAS, 519, 5373. doi:10.1093/mnras/stad042

Lawlor, T.M., MacDonald, J. 2002, Astropys. Space. Sci, 279, 123

Leal-Ferreira, M. L., Gonçalves, D. R., Monteiro, H., et al. 2011, MNRAS, 411, 1395

Liu, X.-W., Storey, P. J., Barlow, M. J., et al. 2000, MNRAS, 312, 585.

Lopez-Camara, D., De Colle, F., Moreno Mendez, E., et al. 2021, arXiv:2110.02227

Louise, R., Michel, F., & Mevolhon, J. C. 1981, AAP, 102, 303

Lundmark, K. 1921, PASP, 33, 314. doi:10.1086/123122

Luridiana V., Morisset C., Shaw R. A., 2015, AAP, 573, A42

MacDonald, J. & Mullan, D. J. 2012, MNRAS, 421, 3084.

Manchado, A., Pottasch, S. R., & Mampaso, A. 1988, AaP, 191, 128

Martin J., Xilouris K., Soker N., 2002, A&A, 391, 689

Meaburn, J. & Lopez, J. A. 1996, ApJl, 472, L45

Meaburn, J., Lopez, J. A., Bryce, M., et al. 1998, AAP, 334, 670

Meaburn, J., López, J. A., Gutiérrez, L., et al. 2003, RMXAA, 39, 185

Michaud, G., Fontaine, G., & Beaudet, G. 1984, ApJ, 282, 206. doi:10.1086/162193

Miglio, A., Brogaard, K., Stello, D., et al. 2012, MNRAS, 419, 2077.

Miller Bertolami, M. M., "A primer on the formation and evolution of hydrogen deficient central stars of planetary nebulae and related objects," *Galaxies*, 2024, submitted. Available under the Creative Commons Attribution (CC BY) license, doi:10.3390/galaxies1010000.

Miller Bertolami, M. M. 2016, AAP, 588, A25. doi:10.1051/0004-6361/201526577

Miller Bertolami, M. M. & Althaus, L. G. 2007, MNRAS, 380, 763. doi:10.1111/j.1365-2966.2007.12115.x

Miller Bertolami, M. M., Althaus, L. G., Serenelli, A. M., et al. 2006, A&A, 449, 313.

Moe, M., & Di Stefano, R. 2017, ApJS, 230, 15.

Monteiro,Hektor & Diego Falceta-Goncalves 2011, ApJ. 7348, 174

Montez, R., Kastner, J. H., De Marco, O., et al. 2005, ApJ, 635, 381

Montoro-Molina B., Guerrero M. A., Pérez-Díaz B., Toalá J. A., Cazzoli S., Miller Bertolami M. M., Morisset C., 2022, MNRAS, 512, 4003.

Montoro-Molina, B., Guerrero, M. A., & Toalá, J. A. 2023, to appear in MNRAS.

Morel, P. & Thévenin, F. 2002, AAP, 390, 611.

Morisset, C. 2013, Astrophysics Source Code Library. ascl:1304.020

Muthumariappan, C. & Parthasarathy, M. 2020, MNRAS, 493, 730

Naito, H., Mizoguchi, S., Arai, A., et al. 2012, AAP, 543, A86.

Nakano, S., Sakurai, Y., Hazen, M., et al. 1996, IAC Circ., 6322

Ondratschek, P. A., Röpke, F. K., Schneider, F. R. N., et al. 2022, AAP, 660, L8.

Osterbrock, D. E. & Ferland, G. J. 2006, Astrophysics of gaseous nebulae and active galactic nuclei, 2nd. ed. by D.E. Osterbrock and G.J. Ferland. Sausalito, CA: University Science Books, 2006

Paczyński, B., 1971, Astrophysical Letters, 9, 33

Parker, Q., et al., 2005, MNRAS, 362, 689

Passy, J. C., De Marco, O., Fryer, C. L., Herwig, F., Diehl, S., Oishi, J. S., ... & Bryan, G. L. 2012, ApJ, 744, 52

Pavlenko, Y. V. & Geballe, T. R. 2002, AaP, 390, 621.

Paxton, B., Bildsten, L., Dotter, A., et al. 2011, ApJs, 192, 3.

Paxton, B., Bildsten, L., Dotter, A., Herwig, F., Lesaffre, P., & Timmes, F. 2010, The Astrophysical Journal Supplement Series, 192, 3

Paxton, B., Cantiello, M., Arras, P., et al. 2013, ApJs, 208, 4. doi:10.1088/0067-0049/208/1/4

Paxton, B., Marchant, P., Schwab, J., et al. 2015, ApJs, 220, 15.

Paxton, B., Schwab, J., Bauer, E. B., et al. 2018, ApJS, 234, 34.

Paxton, B., Smolec, R., Schwab, J., et al. 2019, ApJS, 243, 10.

Peña, M., Hernández-Martínez, L., & Ruiz-Escobedo, F. 2021, MNRAS, 503, 972. doi:10.1093/mnras/stab517

Peña, M., Hernández-Martínez, L., & Ruiz-Escobedo, F. 2021, MNRAS, 503, 972. doi:10.1093/mnras/stab517

Peimbert, M., 1990, Reports on Progress in Physics, 53, 1559.

Peimbert, M. 1967, ApJ, 150, 825. doi:10.1086/149385

Pollacco, D. L. & Hill, P. W. 1994, MNRAS, 267, 692.

Potekhin, A. Y. & Chabrier, G. 2010, Contributions to Plasma Physics, 50, 82.

Pottasch, S.R., Bernard-Salas, J., Beintema, D.A. and Feibelman, W.A., 2003, A&A, 409, 599

Ramos-Larios, G., Phillips, J.P. and Cuesta, L.C., 2011, MNRAS, 411, 1245

Ramos-Larios, G., Santamaría, E., Guerrero, M. A., et al. 2016, MNRAS, 462, 610

Ramstedt, S., Vlemmings, W. H. T., Doan, L., et al. 2020, A&A, 640, A133. doi:10.1051/0004-6361/201936874

Reay, N. K., Atherton, P. D., & Taylor, K. 1983, MNRAS, 203, 1079

Rechy-García, J. S., Guerrero, M. A., Duarte Puertas, S., et al. 2020, MNRAS, 492, 1957

Rechy-García, J. S., Guerrero, M. A., Santamaría, E., et al. 2020, arXiv:2009.13575

Reimers, D. 1975, Memoires of the Societe Royale des Sciences de Liege, 8, 369

Ricker, P. M., & Taam, R. E. 2012, ApJ, 746, 74

Rodríguez-González, J. B., Santamaría, E., Toalá, J. A., et al. 2022, MNRAS, 514, 4794.

Rodríguez-González, J. B., Sabin, L., Toalá, J. A., et al. 2021, MNRAS, 501, 3605.

Rodríguez-González, J. B., Toalá, J. A., Sabin, L., et al. 2022, MNRAS, 515, 1557.

Rogers, F. J. & Nayfonov, A. 2002, ApJ, 576, 1064.

Rosenfield, P., Marigo, P., Girardi, L., et al. 2014, ApJ, 790, 22.

Rotundi, A., Rietmeijer, F. J. M., Colangeli, L., et al. 1998, AaP, 329, 1087

Rouleau, F. & Martin, P. G. 1991, ApJ, 377, 526.

Roxburgh, I.W., 1967, Nature, 215, 838.

Rubio, G., Toalá, J. A., Jiménez-Hernández, P., et al. 2020, MNRAS, 499, 415. doi:10.1093/mnras/staa2837

Sabbadin, F. & Hamzaoglu, E. 1982, AAP, 109, 131

Sabin L., 2008, PhDT

Sabin, L., et al., 2014, MNRAS, 443, 3388

Sahai, R., Morris, M. R., & Villar, G. G. 2011, ApJ, 739, 7

Santamaría, E., Guerrero, M. A., Toalá, J. A., et al. 2022, MNRAS, 517, 2567.

Saumon, D., Chabrier, G., & van Horn, H. M. 1995, ApJs, 99, 713.

Schoenberner, D. 1979, AaP, 79, 108

Seaton, M. J. 2005, MNRAS, 362, L1. doi:10.1111/j.1365-2966.2005.00019.x

Simpson, J., Jones, D., Wesson, R., et al. 2022, Research Notes of the American Astronomical Society, 6, 4.

Smith, J. D. T., Armus, L., Dale, D. A., et al. 2007, PASP , 119, 1133. doi:10.1086/522634

Smith, L. F., & Aller, L. H. 1969, ApJ, 157, 1245

Soker, N. 1997, ApJs, 112, 487.

Solomon, P., Jefferts, K.B., Penzias, A.A. and Wilson, R.W., 1971, ApJ, 163, L53

Stanghellini, L., Corradi, R.L. and Schwarz, H.E., 1993. A&A, 279, 521

Stanghellini, L., Shaw, R. A., Balick, B., & Blades, J. C. 2000, ApJ, 534, L167

Stanghellini, L., Shaw, R.A. and Villaver, E., 2008, ApJ, 689, 194

Starrfield, S., Truran, J. W., Wiescher, M. C., et al. 1998, MNRAS, 296, 502. doi:10.1046/j.1365-8711.1998.01312.x

Steffen, W., Koning, N., Wenger, S., et al. 2011, IEEE Transactions on Visualization and Computer Graphics, 17, 454

Sutherland, R., Dopita, M., Binette, L., et al. 2018, Astrophysics Source Code Library. ascl:1807.005

Tafoya, D., Toalá, J. A., Unnikrishnan, R., et al. 2022, APjL, 925, L4.

Tafoya, D., Toalá, J. A., Vlemmings, W. H. T., et al. 2017, AAP, 600, A23.

Thompson, T. A. 2011, ApJ, 741, 82.

Thoul, A. A., Bahcall, J. N., & Loeb, A. 1994, ApJ, 421, 828.

Timmes, F. X. & Swesty, F. D. 2000, ApJs, 126, 501.

Toalá, J. A. & Arthur, S. J. 2014, MNRAS, 443, 3486

Toalá, J. A., Guerrero, M. A., Todt, H., et al. 2015, ApJ, 799, 67.

Toalá, J. A., Jiménez-Hernández, P., Rodríguez-González, J. B., et al. 2021, MNRAS, 503, 1543.

Toalá, J. A., Lora, V., Montoro-Molina, B., et al. 2021, MNRAS, 505, 3883.

Toalá, J. A., Montez, R., & Karovska, M. 2019, ApJ, 886, 30

Toalá, J. A., Ramos-Larios, G., Guerrero, M. A., et al. 2019, MNRAS, 485, 3360

Toalá, J. A., Todt, H., & Sander, A. A. C. 2024, MNRAS, 531, 2422.

Todt, H. & Hamann, W.-R. 2015, Wolf-Rayet Stars, 253

Todt, H., Gräfener, G., & Hamann, W.-R. 2006, Planetary Nebulae in our Galaxy and Beyond, 234, 127.

Todt, H. & Hamann, W.-R. 2015, Wolf-Rayet Stars, 253

Tody, D. 1993, Astronomical Data Analysis Software and Systems II, 52, 173

Trimble, V. and Sackmann, I.J., 1978. MNRAS, 182, 97

Turcotte, S., Richer, J., & Michaud, G. 1998, ApJ, 504, 559.

Vassiliadis, E. & Wood, P. R. 1993, ApJ, 413, 641

Vauclair, S. 1983, Saas-Fee Advanced Course 13: Astrophysical Processes in Upper Main Sequence Stars, 167

Viegas, S. M. & Clegg, R. E. S. 1994, MNRAS, 271, 993.

Villaver, E., García-Segura, G., & Manchado, A. 2002, ApJ, 571, 880

Villaver, E., Manchado, A., & García-Segura, G. 2012, ApJ, 748, 94

Weidmann, W.A. et al. 2020, A&A, 640, A10

Werner, K., & Herwig, F. 2006, PASP, 118, 183

Wesson, R., Barlow, M. J., Liu, X.-W., et al. 2008, MNRAS, 383, 1639.

Wesson, R., Jones, D., García-Rojas, J., et al. 2018, MNRAS, 480, 4589.

Wesson, R., Liu, X.-W., & Barlow, M. J. 2003, MNRAS, 340, 253.

Williams, R. J. R. 1999, MNRAS, 310, 789

Willson, L. A. 2000, ARAA, 38, 573.

Wyse, A. B. 1942, ApJ, 95, 356.

Yadoumaru, Y. & Tamura, S. 1994, PASP, 106, 165. doi:10.1086/133364

Zou, Y., Chamandy, L., Carroll-Nellenback, J., et al. 2022, arXiv:2202.05715

Zou, Y., Frank, A., Chen, Z., et al. 2020, MNRAS, 497, 2855. doi:10.1093/mnras/staa2145